EXTERNAL AND INTERNAL OXIDATION PROPERTIES OF TERNARY FE-SI-AL, NI-CR-AL, AND NI-SI-AL ALLOYS

By

Shiwei Guan, B.Eng., M.Eng.

A Thesis

Submitted to the School of Graduate Studies

in Partial Fulfilments of the Requirements

for the Degree

Doctor of Philosophy

McMaster University

OXIDATION PROPERTIES OF Fe-Si-Al, Ni-Cr-Al, AND Ni-Si-Al ALLOYS

DOCTOR OF PHILOSOPHY (1993) McMASTER UNIVERSITY
(Materials Science and Engineering) Hamilton, Ontario

TITLE: External and Internal Oxidation Properties of
Ternary Fe-Si-Al, Ni-Cr-Al, and Ni-Si-Al Alloys

AUTOR: Shiwei Guan, B.Eng. (Nanchang Aeronautical Engineering University)
M.Eng. (Academia Sinica)

SUPERVISOR: Professor W.W. Smeltzer

NUMBER OF PAGES: xii, 209

ABSTRACT

The oxidation properties of binary and ternary Fe-Si-Al alloys containing 0-6 at% Si and 0-6 at% Al were investigated at 1073 K in 0.04-0.07 torr and 760 torr of oxygen. In combination with Si, the Al concentration required to form a protective Al_2O_3 scale on the ternary alloys is significantly lower than that for binary Fe-Al alloys. Theoretical and experimental results are consistent with the hypothesis that there is a synergistic effect due to the combined presence of Si and Al, resulting in improved oxidation resistance of the ternary Fe-Si-Al alloys. Si appears to limit the oxidation of Fe during the transient stage of oxidation and increase the activity and outward diffusion flux of Al to the oxide/alloy interface through ternary interactions during the subsequent stage of parabolic oxidation kinetics.

A criterion has been established for the onset of internal oxidation beneath the external scale when oxidizing conditions favor formation of the oxide of the least noble metal in a dilute ternary alloy. This criterion was applied to the oxidation of ternary Fe-Si-Al and Ni-Cr-Al alloys. Theoretical predictions of minimum Al concentrations required to form a protective Al_2O_3 scale on these two alloys are consistent with the experimental observations.

Attempts were made to give expressions describing the kinetics of internal oxidation of dilute ternary alloys during simultaneous internal oxidation of the two solutes. Good agreement was obtained between theoretically predicted and experimentally observed values of the depths of internal oxidation zones in Ni-1at%Si-4at%Al alloys at 1073 K in Ni/NiO packs or in 760 torr of oxygen.

ACKNOWLEDGEMENT

The author wishes to express his sincere gratitude to Dr. W.W. Smeltzer for his suggestion of the problems considered here and for his guidance, help and encouragement throughout the course of this study. The interest and encouragement shown by Drs. M.B. Ives, D.A. Thompson, and A. Petric, who were members of the supervisory committee, is gratefully acknowledged.

The excellent technical support of J.D. Garrett, C. Butcher, F. Pearson, A. Duft, and J. Hudak was greatly appreciated. I would like to thank Dr. H.C. Yi for his cooperation and insights in studying the internal oxidation of Ni-Si-Al alloys, and Dr. R. Macaulay-Newcombe for his kind help and encouragement during my thesis writing. Thanks are also due to Dr. R.N.S. Sodhi at the Centre for Biomaterials of the University of Toronto, and Dr. M.J. Graham and his group at the Institute for Microstructural Sciences of the National Research Council for carrying out the SIMS measurements.

The financial support of the University Centennial Scholarship and the Department of Materials Science and Engineering is acknowledged. Finances for the support of this research were obtained from a research grant to Dr. W.W. Smeltzer by the Natural Sciences and Engineering Research Council of Canada.

Finally, I would like to thank Dr. A.N. Bourns, the former President of the University, and Dr. C.X. Shi, the Vice Chairman of the National Natural Science Foundation of China, for recommending that I pursue graduate studies at McMaster. I am also indebted to my family in China for their limitless help and support.

TABLE OF CONTENTS

LIST OF FIGURES

LIST OF TABLES

CHAPTER 1

Introduction

Few metals are thermodynamically stable when exposed to ambient gases especially at high temperatures. Consequently, most metals in service today are subject to deterioration by reaction with the atmosphere, which is designated by the term "oxidation". As pure metals are rarely used as constructional materials, oxidation of alloys and, particularly, oxidation of multicomponent alloys, is the most important aspect of high temperature oxidation of metals from an applied point of view. Because of this technological importance, numerous studies of oxidation of alloys are reported in the literature. Due to the complexities of reaction mechanisms as well as thermodynamic and diffusion behavior in multicomponent systems, however, basic studies of alloy oxidation have largely been confined to binary alloys.

The current work, an approach to the fundamental study of ternary alloy oxidation, involves theoretical and experimental studies of three important aspects of alloy oxidation: (i) protective scale formation and growth, (ii) the transition from internal to external oxidation, and (iii) the kinetics of selective internal oxidation. In particular, it focuses on the external and internal oxidation properties of three ternary alloy systems:

(i) Fe-Si-Al alloys: Early studies on the oxidation of Fe-Si-Al alloys [1.1-3] indicate that in combination with Si, the Al content required to form a

protective alumina scale is significantly lower than that in the binary Fe-Al system. The synergistic beneficial effect of the Al/Si combination, however, is not well understood. Therefore, this investigation includes detailed morphological and compositional studies of the oxide scales formed, in conjunction with oxidation rate measurements. It also includes detailed evaluations of thermodynamic and diffusion properties of the system. Based on these observations and calculations, models are proposed, describing the development and growth of oxide phases on Fe-Si-Al alloys.

(ii) Ni-Cr-Al alloys: Oxidation of Ni-Cr-Al alloys has been a typical example of ternary alloy oxidation. Addition of Cr to Ni-Al alloys generally aids in establishing a protective alumina scale. For this alloy system sufficient experimental data [1.4-6] are available to permit the construction of 'oxide maps' which delineate the composition ranges for formation of different types of oxide scales. Such oxide maps, however, only represent a summary of empirical, experimental data. "A great challenge for investigators in the field", as suggested by Per Kofstad [1.7], "is to be able to derive such maps from more basic data involving the interplay of thermodynamics, diffusion data and interface reactions". Two goals for the current work are: (*a*) to obtain a theoretical criterion to predict minimum bulk solute concentrations in ternary alloys required to form a protective oxide scale, and (*b*) to test predictions of this criterion by comparing them with experimental observations available from many investigators.

(iii) Ni-Si-Al alloys: Internal oxidation is a common phenomenon in the high temperature oxidation of dilute solid solution alloys. Expressions to describe the kinetics of internal oxidation in binary alloys have been derived by several researches [1.8-11]. Unfortunately, there is no model yet available to interpret

the internal oxidation behavior of ternary alloys. The current work, the first phase of such a research effort, focuses on the case when oxidation conditions favor the simultaneous formation of oxides of both solutes in a ternary alloy. Kinetics models are proposed and the applicability of these models is tested by comparing predicted values of the depth of the internal oxidation zone with experimentally measured values for the internal oxidation of Ni-4 at% Al-1 at% Si alloys.

The thesis is arranged in eight chapters. Chapter 2 gives a brief description of applicable theories for alloy oxidation, and includes the commonly encountered equations for predictions of thermodynamic and diffusion properties of multicomponent systems. This is followed by a literature review of the systems Fe-Si-Al, Ni-Cr-Al, and Ni-Si-Al in chapter 3. In chapter 4 the theoretical considerations of this work for ternary alloy oxidation are given in detail. The various experimental techniques used in this work are described in chapter 5. Experimental results are presented in chapter 6, and discussed in chapter 7 together with the theoretical results. Finally, in chapter 8, this work is summarized and recommendations for future work are given.

CHAPTER 2

Principles of Alloy Oxidation

2.1 Introduction

When a clean surface of metal is exposed to the attack of a gas such as oxygen, the reaction commences at the metal-gas interface, and unless the reaction products are volatile, they form an intermediate layer between the metal and the gas. Thermodynamic equilibrium governs this reaction to the extent that it generally determines which compounds, if any, are formed, but the rate at which compound formation occurs is a kinetic problem. Transition metals in their pure form, when exposed to oxygen, usually form thick and non-protective oxide layers at high temperatures. It is therefore necessary to alloy the pure metal with at least one component such as aluminum, chromium, or silicon, which will oxidize selectively and produce a protective oxide scale. The protective oxide scale refers to a continuous, external, parabolically thickening solute oxide scale which grows at a significantly slower rate than the oxide of the base metal.

Although considerable knowledge has accumulated both from basic and from engineering studies, oxidation mechanisms of alloys are still often inadequately understood. This reflects a lack of knowledge of aspects such as alloy-oxide systems and their structures, phase diagrams and other thermodynamic properties, transport mechanisms and diffusion in alloy phases and in oxide scales, adherence

of scale to the metal, etc. It is certainly the case for oxidation of alloys containing three or more components.

The aim of this chapter is to present a summary of alloy oxidation principles. A more extensive description is to be found in many of the standard works in this field [2.1-8].

2.2 Thermodynamics and Diffusion of Multicomponent Systems

2.2.1 Prediction of Thermodynamic Properties

There is a considerable need to predict the thermodynamic properties of a ternary or multicomponent solution phase from the properties of its binary components. The prediction is particularly important for systems at elevated temperatures, due to the difficulty of experiments. During the past two decades, a large number of models have been proposed for practical calculations of ternary thermodynamic properties and phase diagrams from binary selected data, among which the models of Kohler [2.9], Colinet [2.10], Muggianu [2.11], Toop [2.12], Hillert [2.13], and Chou [2.14] have been utilized and discussed extensively. A good review of many such models may be found in an article by Ansara [2.15]. Fig. 2.1 gives a geometric illustration of the above models. In most cases it shows that these models may lead to reasonably satisfactory results.

For ternary systems, it is useful to consider properties such as the excess Gibbs free energies of the solution as the sum of binary contributions and specifically ternary ones. One may write

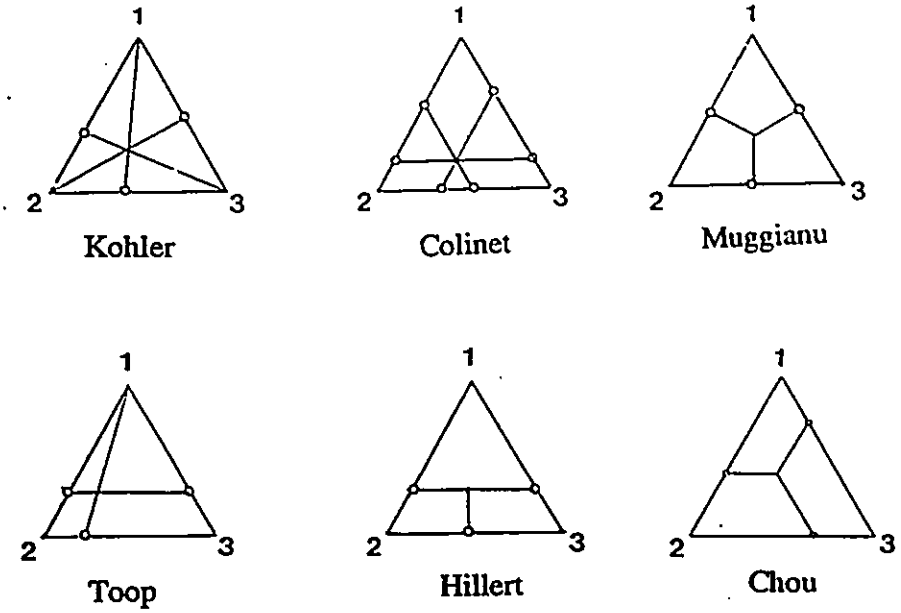

Figure 2.1 Composition paths relating the ternary excess quantity to the binary ones according to various models

Table 2.1 Ternary interaction coefficients of several models

Models	f_k
Colinet	0
Muggianu	0
Hillert	$-(B_{12} + B_{13})$
Toop	$-B_{12} - B_{13} + B_{23}(N_2-N_3)/(N_2+N_3)$
Kohler	$\Sigma\, B_{ij}(N_i-N_j)/(N_i+N_j)$
Chou	$-(B_{12} + B_{31} + B_{23})$

$$G^E = G^E(N_1,N_2) + G^E(N_1,N_3) + G^E(N_2,N_3) + f_k N_1 N_2 N_3 \qquad (2.1)$$

where: $G^E(N_i,N_j)$ represents an analytical expression of G^E for the binary system i-j; N_i represents the mole fraction of component "i" in the ternary system; f_k is referred to as "ternary interaction coefficient" which indicates the magnitude of the interaction among three components. For a binary quasi-regular model, $G^E(N_i,N_j)$ can be expressed as

$$G^E(N_i,N_j) = N_i^{\dagger} N_j^{\dagger} [A_{ij} + B_{ij}(N_i^{\dagger} - N_j^{\dagger})] \qquad (2.2)$$

where A_{ij}, B_{ij} represent the coefficients of the binary quasi-regular model and $N_i^{\dagger}$, $N_j^{\dagger}$ represent the mole fractions for "ij" binary systems respectively. Thus, the difference among the above ternary models will be only in the ternary interaction term [2.14], as shown in Table 2.1.

From Table 1, it can be seen that Colinet's and Muggianu's models do not contain a ternary interaction term. f_k of Hillert's model only depends on 1-2 and 1-3 binary systems but has no relation to the 2-3 binary system. f_k of Toop's model is near that of Hillert's, which is mainly related to 1-2 and 1-3 and has little relation with 2-3 system due to small values of $(N_2-N_3)/(N_2+N_3)$. Kohler's model can describe the contributions from three binary systems to the ternary interaction term simultaneously; f_k, however, tends to zero when $N_1 = N_2 = N_3$, which does not reflect the situation for some real systems. In general, most real solutions should involve a ternary interaction term in their expressions of ternary molar properties, and Chou's model probably is useful for some systems where the ternary interaction effect is not negligible.

The case of a quaternary system is similar. The properties of the system are considered as the sum of related binary and ternary contributions and specifically quaternary ones. Different formulae take into account the limiting binary and/or ternary systems in different ways [2.16]. These analytic techniques are very arbitrary, and their selection is entirely at the discretion of the investigator.

Once an expression of the excess Gibbs free energy has been selected, the expressions of the activity coefficients for an n-component system can easily be derived through the following equations:

$$G_i^E = RT\ln \gamma_i = G^E + \sum_{j=2}^{n} (\delta_{ij} - N_j)\frac{\partial G^E}{\partial N_j} \qquad (2.3)$$

where δ_{ij} is Kronecker's symbol ($\delta_{ij} = 0$ for $i \neq j$ and $\delta_{ij} = 1$ for $i = j$).

In the case of a dilute solution (*i.e.*, $N_i \leq 0.1$), the activity coefficient for component i in the form of ($\ln \gamma_i$) can be expanded as a Taylor series about a state of infinite dilution and to the first order has the form

$$\ln \gamma_i = \ln \gamma_i^{\infty} + \varepsilon_{i1} N_1 + \varepsilon_{i2} N_2 + \ldots \qquad (2.4)$$

where the γ_i^{∞} is the value of the activity coefficient γ_i at infinite dilution, and the coefficients of the ensuing terms, ($\partial \ln \gamma_i / \partial N_j = \varepsilon_{ij}$) defined as the Wagner interaction coefficients, are constant. The Maxwell relation for exact differentials yields the symmetry relations, $\varepsilon_{ij} = \varepsilon_{ji}$. For a ternary A-B-C metallic system, the values of ε_{BC} may be estimated [2.16] from the properties of the binary limiting systems by the equation

$$\varepsilon_{BC} = (\ln \gamma_C^{\infty})_{B\text{-}C} - (\ln \gamma_B^{\infty})_{A\text{-}B} - (\ln \gamma_C^{\infty})_{A\text{-}C} \tag{2.5}$$

and, if A is selected to be solvent,

$$\varepsilon_{BB} = -2(\ln \gamma_B^{\infty})_{A\text{-}B} \tag{2.6}$$

The values of $\ln \gamma_i^{\infty}$ in the binary limiting systems can be obtained from experimental measurements or be calculated by invoking proper models of statistical thermodynamics [2.16]. Related to alloy oxidation, there is a model derived by Wagner [2.17], and further extended by Chiang and Chang [2.18] to describe the effect of alloying elements on the activity coefficients of oxygen. The interaction parameter of ε_{OB} in binary A-B alloy can be expressed as [2.19]

$$\varepsilon_{OB} = Z\left[1 - \left[\frac{\gamma_{O(A)}^{\infty}}{\gamma_{O(B)}^{\infty}}\right]^{1/Z} \exp\left[\frac{(Z-1)}{2RT}\, h\right]\right] \tag{2.7}$$

where Z is the coordination number, $\gamma_{O(A)}^{\infty}$, $\gamma_{O(B)}^{\infty}$ are the activity coefficients of O in pure A and in pure B at infinite dilute solution respectively. Wagner's h parameter can be estimated by the following equation

$$h = 2\Omega Z^{-2} + 0.09[\Omega(V_B/V_A)^2] + 0.04RT[\ln \gamma_{O(A)}^{\infty} - \ln \gamma_{O(B)}^{\infty}] \tag{2.8}$$

where Ω is $\Delta H/N(1\text{-}N)$ with ΔH being the enthalpy of formation of $A_{1-N}B_N$ alloy and V_B, V_A are the valences of pure A and B.

2.2.2 Diffusion Equations

The phenomenological description of multicomponent diffusion originally proposed by Onsager [2.20] has served as the basis for both theoretical and experimental diffusion studies in alloys with three or more components. The major contributions and advances made in this area over the decades have been reviewed by Kirkaldy and Young [2.8]. According to the phenomenological diffusion theory of Onsager [2.20], a linear flux-force relation exists for a system near equilibrium. The flux J_i of component "i" in an n-component isotropic solid subjected to chemical potential gradients is

$$J_i = - \sum_{k=1}^{n} L_{ik} \frac{\partial \mu_k}{\partial x} = - \sum_{k=1}^{n-1} D_{ij} \frac{\partial C_j}{\partial x} \qquad (2.9)$$

where L_{ik} and D_{ij} are phenomenological coefficients and diffusivities, respectively, and $\partial \mu_k / \partial x$ and $\partial C_j / \partial x$ are the chemical potential and molar concentration gradients. Assuming that $L_{ii} \gg L_{ik}$ and that the main-term phenomenological coefficient is related to the binary self-diffusion coefficient $D_i(n)$ of "i" in the solvent "n" by the Nernst-Einstein relation,

$$L_{ii} = D_i(n) C_i / RT \qquad (2.10)$$

For a ternary system, this implies that [2.7]

$$D_{ii} = \frac{D_i(3) C_i}{RT} \left. \frac{\partial \mu_i}{\partial C_i} \right|_{C_j}, \ (i, j = 1, 2), \text{ and} \qquad (2.11)$$

$$D_{ij} = \frac{D_i(3)\ C_i}{RT} \left.\frac{\partial\ \mu_i}{\partial\ C_j}\right|_{C_i}, \quad (i, j = 1, 2). \tag{2.12}$$

Since we have that

$$\mu_i = \mu_i^{\circ} + RT \ln \gamma_i N_i \tag{2.13}$$

and the mole fraction

$$N_i = C_i \tilde{M} / \rho \tag{2.14}$$

where $\tilde{M}$, ρ are the average molar weight and density of the solid respectively, Eqs. (2.11) and (2.12) become

$$D_{ii} = D_i(3) \left[1 + N_i \left.\frac{\partial \ln\ \gamma_i}{\partial\ N_i}\right|_{N_j}\right], \quad (i, j = 1, 2), \text{ and} \tag{2.15}$$

$$D_{ij} = D_i(3)\ N_i \left.\frac{\partial \ln\ \gamma_i}{\partial\ N_j}\right|_{N_i}, \quad (i, j = 1, 2). \tag{2.16}$$

Practically it may be convenient to write the flux equations (Eq. (2.9)) in terms of the mole fractions N_i rather than the molar concentrations C_i. If the N_i are written as the elements of a column vector (N); the J_i as the elements of a column vector (J); and the D_{ij} as the elements of a diffusion coefficient matrix, [D]; then the general diffusion equation in matrix notation, based on Eq. (2.9), can be written as

$$\frac{\partial (N)}{\partial t} = [D] \frac{\partial^2 (N)}{\partial x^2} \tag{2.17}$$

The general method for solving Eq.(2.17) is given by Toor [2.21] for the case of constant diffusion coefficients. Assuming that [D] may be diagonalized by a nonsingular matrix [θ] and letting

$$(\psi) = [\theta]^{-1}(N) \tag{2.18}$$

then operating on Eq.(2.17) by $[\theta]^{-1}$ one obtains

$$\frac{\partial (\psi)}{\partial t} = [\theta]^{-1}[D][\theta] \frac{\partial(\psi)}{\partial x^2}, \tag{2.19}$$

which represents the set of scalar diffusion equations

$$\frac{\partial \psi_k}{\partial t} = D_k \frac{\partial^2 \psi_k}{\partial x^2}, \quad (k = 1, 2, ..., n-1) \tag{2.20}$$

where D_k are the eigenvalues of [D] obtained by solving the characteristic equation of [D]. Solution of Eq. (2.20) is then

$$\psi_k = U_k + W_k \operatorname{erf} \left(\frac{x}{2\sqrt{D_k t}}\right), \quad (k = 1, 2, ..., n-1) \tag{2.21}$$

where U_k and W_k are constants defined by initial and boundary conditions. Since $[\psi] = [\theta]^{-1}[N]$, the result is that

$$N_j = \sum_{k=1}^{n-1} \theta_{jk} U_k + \sum_{k=1}^{n-1} \theta_{jk} W_k \operatorname{erf}\left(\frac{x}{2\sqrt{D_k t}}\right). \qquad (2.22)$$

2.3 Oxidation of Alloys

2.3.1 Internal Oxidation

Internal oxidation is the process by which oxygen diffuses into a dilute alloy and causes sub-surface precipitation of oxides of one or more alloying elements. The criteria for internal oxidation are: (a) the free energy of formation of the solute oxide must be more negative than that of the solvent oxide; (b) the solvent metal must exhibit a significant solubility and diffusivity of oxygen; (c) the solute concentration must be lower than that required to cause a transition from internal to external oxidation; and (d) surface-oxide layers must not prevent oxygen diffusion into the substrate.

The simplest system for analysis is internal oxidation in the absence of external scale. This is achieved if the oxygen partial pressure is at, or below, the dissociation pressure of the oxide of the relatively noble metal solvent. Such a system may be obtained by means of a 'Rhines pack', in which specimens of the alloy are located in a powder mixture of a large amount of the metal solvent and its lowest oxide, so the oxygen pressure is held at the dissociation pressure of the solvent oxide [2.22]. In the case of exclusive internal oxidation of a binary A-B alloy, the depth of the internal zone, ξ, is a parabolic function of time t expressed by Wagner [2.23]

$$\xi = 2\gamma(D_O t)^{1/2} \tag{2.23}$$

where D_O is the diffusion coefficient of oxygen in the solvent A. γ is a dimensionless parameter. At the precipitation front of the zone of internal oxidation, the flux of oxygen atoms arriving from the external surface must be equivalent to the flux of B atoms arriving from the bulk alloy if an insoluble and stoichiometric BO_ν oxide particle is precipitated. Thus an expression for γ can be obtained by solving the diffusion equations for oxygen and for the solute B

$$\frac{N_O^s}{\nu N_B^o} = \frac{G(\gamma)}{F(\gamma\phi^{1/2})} \tag{2.24}$$

where $\phi = D_O/D_B$, D_B is the diffusion coefficient of B in the alloy, N_O^s is the mole fraction of oxygen at the outer surface, N_B^o is the mole fraction of B in the bulk alloy, and ν is a number expressing the stoichiometry of the precipitated oxide BO_ν, the auxiliary functions G and F are defined by

$$G(u) = \pi^{1/2}\, u\, \exp(u^2)\, \mathrm{erf}(u), \text{ and} \tag{2.25}$$

$$F(u) = \pi^{1/2}\, u\, \exp(u^2)\, \mathrm{erfc}(u). \tag{2.26}$$

Therefore the parameter γ may be obtained from a graphical or numerical solution of Eq. (2.24). Two limiting cases exist. If $\gamma \ll 1$ and $\gamma\phi^{1/2} \gg 1$

$$\gamma = \left[\frac{N_O^s}{2\nu N_B^o}\right]^{1/2} \tag{2.27}$$

Eq. (2.27) is expected to hold under conditions where the movement of the precipitation front is predominantly determined by the diffusion of oxygen in the solvent metal. There is a second limiting case —— if $\gamma \ll 1$, but $\gamma\phi^{1/2} \ll 1$

$$\gamma = \frac{N_O^s \ (\pi\phi)^{1/2}}{2\nu N_B^o} \tag{2.28}$$

In this case, the rate of outward diffusion of the alloying element as well as the rate of inward diffusion of oxygen are both important in determining the kinetics of oxidation.

In most practical applications of alloys at high temperatures the internal oxidation zone is formed below an external oxide scale of the solvent metal. Analytic solutions for the kinetics of internal oxidation in combination with a parabolically thickening external scale have been given by Rhines *et al* [2.24], Maak [2.25] and Gesmundo and Viani [2.26]. Retaining the same symbols as above, except that N_O^s now equals the oxygen mole fraction at the metal/scale interface and k_C the parabolic rate constant for the external scale, Maak solved the diffusion equations for oxygen and B in the alloy and obtained a complicated expression for γ

$$\frac{N_O^s}{\nu N_B^o} = \frac{\{\mathrm{erf}(\gamma) - \mathrm{erf}[(k_C/2D_O)^{1/2}]\}}{\mathrm{erf}(\gamma)} \frac{G(\gamma)}{F(\gamma\phi^{1/2})} \tag{2.29}$$

The above analysis of internal oxidation is essentially for the situation where the amount of precipitate is constant across the internal oxidation zone and precipitation occurs at the subscale-matrix interface. In the other situation

precipitation occurs continuously through the subscale as it forms. Both of these limiting situations can be treated as approximations to a general equation derived by Kirkaldy [2.27] for simultaneous diffusion and precipitation in ternary systems as exemplified by Morral and coworkers [2.28-29] and by Kirkaldy and Young [2.8] in their textbook on diffusion in the condensed state. Internal oxidation of several noble-based binary alloys leads to penetration of subscales of almost constant oxide volume fraction by parabolic kinetics. Alloy systems following the second limiting situation have not been examined in any detail in literature.

2.3.2 Transition from Internal to External Oxidation

Wagner [2.23] has proposed that the transition from internal to exclusive external oxidation should occur when the solute content in a binary alloy is sufficient to form a critical volume fraction of internal oxide precipitate at the reaction front. Basically, as the solute content increases, the oxide-particle density increases. If f is the mole fraction of the solute oxide BO_V in the internal oxidation zone, then the ratio of f to the molar volume of the alloy V_a is the molar concentration of the oxide per unit volume. Consider the advance by a distance $d\xi$ of the precipitation front of area A in a time dt; in the volume element $Ad\xi$, the number of moles of oxide BO_V precipitated, which by definition equals $(f/V_a)Ad\xi$, must also equal to the number of moles of B arriving at the front through diffusion from $x > \xi$

$$\left[\frac{f}{V_a}\right]Ad\xi = \lim_{\varepsilon \to 0}\left[\frac{D_{AB}\,A}{V_a}\left[\frac{\partial N_B}{\partial x}\right]_{x=\xi+\varepsilon}\right]dt \qquad (2.30)$$

Substituting $d\xi/dt$ from Eq. (2.23) and considering the general expression Eq. (2.24) will yield expressions for an enrichment factor α

$$\alpha = \frac{f}{N_B^o} = \frac{1}{F(\gamma\phi^{1/2})} \tag{2.31}$$

where the auxiliary function F and ϕ are as defined previously. When the volume fraction of the oxide, $f_v = f\varphi$, reaches the critical value f_v^*, the critical bulk solute content N_B^* for the transition from internal to external oxidation is then defined from Eq. (2.31) as [2.26]

$$N_B^* = \frac{1}{\varphi} f_v^* F(\gamma\phi^{1/2}) \tag{2.32}$$

where φ is the ratio of the molar volume of BO_v, V_{ox}, to that of the alloy, V_a. For the case of $\gamma \ll 1$ and $\gamma\phi^{1/2} \ll 1$, Eq. (2.32) can be simplified as [2.23]

$$N_B^* = \left[\frac{\pi f_v^* N_O^s \phi}{2 v \varphi}\right]^{1/2} \tag{2.33}$$

The application of Eq. (2.33) requires an empirical knowledge of the critical volume fraction of oxide f_v^*. Rapp [2.30] has found experimentally that initial oxide volume in the range of $0.3 \le f_v^* \le 0.5$ could lead to the transition from internal to external oxidation of several noble-base alloy.

If an external oxide scale of BO_v is already formed on the binary alloy, the criterion for the onset of internal oxidation is when conditions exist at the alloy side of the scale/alloy interface for the product of the solute and oxygen

concentrations to exceed the solubility product of BO_V. Wagner [2.31] has utilized the solutions of diffusion equations to obtain an expression for the product $N_B N_O^V$. The gradient of this product, $g = \frac{\partial}{\partial x} \ln(N_B N_O^V)_{x=\xi}$ is related to the diffusion parameter in the alloy, the bulk alloy composition, composition of the alloy at the scale/alloy interface, and the rate of thickening of the external scale. There are several possibilities: *i*) If g is negative, the alloy next to the scale is undersaturated with respect to the oxide BO_V and no internal oxidation can occur. *ii*) If g is zero, the alloy is saturated and at the limit for internal oxidation. *iii*) If g is positive, the alloy is supersaturated and internal oxidation is possible. These conditions thus establish a minimum bulk concentration (N_B^*) above which internal oxidation will not occur and the external scale forms alone as:

$$N_B^* = \frac{\nu F(u) + u(\phi\pi)^{1/2}}{\nu + u(\phi\pi)^{1/2}} \tag{2.34}$$

where u replaces $(k_C/2D_{AB})^{1/2}$, k_C is the parabolic rate constant for the growth of BO_V, and D_{AB} is the interdiffusion coefficient of the alloy. The auxiliary function F(u) and all other parameters are as defined previously. Wagner's analysis has been extended by Smeltzer and Whittle [2.32] using the diffusion path concept. In semi-infinite ternary diffusion couples, an extra degree of freedom is introduced which makes possible the appearance of nonplanar interfaces. As a first approximation, all interfaces are assumed flat, and the diffusion equations previously discussed are solved for an assumed order of phases between the termini of the diffusion couple. Referring to Eq. (2.22), it can be seen that the two independent concentrations can be expressed as a function of the same parameter λ

$= x/\sqrt{t}$. By solving one concentration in terms of the other and plotting the solution on a ternary isotherm, the result is a time invariant mapping of the concentration profile. If a solution is found which duplicates the assumed order of phases and satisfies local equilibrium at all interfaces (crosses all two-phase fields coincident with tie lines) then the solution is a possible one. If the path enters a two-phase region and cuts tie lines, the calculated path is unstable and is called a virtual path [2.8]. Because of this instability, the actual path will have either nonplanar interface or internal precipitates, or even both. Equations have been derived for the onset of internal oxidation based on the two assertions relating the locus of the virtual diffusion path on the ternary alloy-oxygen isotherm: *i*) External scale formation alone occurs when the virtual diffusion path in the alloy phase contacts and is tangent to the oxygen solubility curve for the alloy. *ii*) External scale formation with internal oxidation occurs when the virtual path for the alloy cuts into and across the two phase alloy-oxide region. Thus a minimum solute concentration for external scale formation alone can be defined as [2.32]

$$\varepsilon_{OB}(N_B^*)^2 + \left[\frac{1-F(u)}{F(u)}\left[1 + \frac{u(\phi\pi)^{1/2}}{\nu}\right] - \varepsilon_{OB}[1 + F(u)]\right](N_B^*) + \left[\varepsilon_{OB}F(u) - [1 - F(u)] - \frac{1-F(u)}{F(u)}\,\frac{u(\phi\pi)^{1/2}}{\nu}\right] = 0 \qquad (2.35)$$

where ε_{OB} is the Wagner thermodynamic interaction parameter between oxygen and the solute B.

2.3.3 Formation and Growth of Protective Scales and the Third-Element Effect

At sufficiently high concentrations, the preferential or selective oxidation of alloying components such as aluminum, chromium, and silicon to yield continuous external scales of Al_2O_3, Cr_2O_3 and SiO_2, respectively, is an important means of achieving oxidation protection in practical alloys. The growth of these protective scales usually follows a parabolic rate law

$$\frac{dx}{dt} = \frac{k}{x}; \qquad x^2 = 2kt \tag{2.36}$$

where k is parabolic rate scaling constant and x is scale thickness.

Wagner [2.33] formulated a quantitative theory for parabolic growth of oxide scales on pure metals. He postulated that the species of ambipolar diffusion (charge migration under local electroneutrality) in the oxide scales are ions and electrons which migrate independently. Reactions at the oxide/gas and oxide/metal interfaces are considered to be sufficiently rapid for local equilibrium to be established at these interfaces. The expressions for the rate constant k is given by

$$k = \frac{1}{2}\int_{p_{O2}^{i}}^{p_{O2}^{o}} \left[\frac{z_c}{|z_a|} D_M + D_O\right] d\ln p_{O2} \tag{2.37}$$

where p_{O2}^{o} is the oxygen pressure in the ambient gas phase and p_{O2}^{i} the oxygen partial pressure at the metal/oxide interface, D_M and D_O are the self diffusion coefficients of the metal and oxygen, respectively. Z_M and Z_O are their valences.

It is frequently observed that the rate of growth of oxide scales on metals is greater than that predicted using the parabolic rate constant defined by Eq. (2.37). This apparent failure of Wagner's theory can be rectified if normal diffusion is "short circuited" by paths of higher diffusivity such as pores, grain boundaries or dislocations. Following the method of Smeltzer and coworkers [2.34], an effective volumetric diffusion coefficient, D_{eff}, may be defined to describe reaction transport across the oxide scale as

$$D_{eff} = D_L(1 - f) + D_B f \tag{2.38}$$

where D_L and D_B are diffusivities for the lattice and internal boundaries respectively, and f is the area fraction of low resistance diffusion paths. Using Eq. (2.38), a modified parabolic law may be written. The modified parabolic rate constant is

$$k_{eff} = k \int_0^t \left[1 + \frac{D_B}{D_L} f\right] dt \tag{2.39}$$

The growth of single phase ternary oxides on binary alloys may be described by Wagner's [2.35] ternary diffusion model. From the model it may be possible to calculate the parabolic rate constant and alloy composition and oxygen activity profiles as a function of the scale thickness if the cation diffusivities in the oxide are known as functions of composition and oxygen activity.

The establishment of protective scales on binary alloys is facilitated by the presence of a third element (such as Cr for Ni-Al alloys, Zn for Cu-Al alloys, or Si for Fe-Al alloys), where the added component is one forming an oxide of

intermediate stability compared to the base metal and protective oxides. The minimum bulk concentrations of the least noble metal in the ternary alloys, being required to form the protective oxide scales, are much lower than those in the binary alloys. To explain this *Third Element Effect*, Wagner [2.36] has proposed the following mechanisms: 1. Additions getter oxygen by reacting with oxygen before it can diffuse into the alloy. 2. The oxides formed by the gettering action block oxygen and reduce its flux into the alloy. 3. The additions alter the oxides that form and makes them more protective. A fourth mechanism proposed by Morral and coworkers [2.37-38] is: 4. The additions increase the flux of the least noble metal from the bulk of the alloy to the alloy/oxide interface. Predicting this fourth effect requires knowledge of the "square root" diffusivity matrix. The square root diffusivity matrix [r] is related to the diffusivity matrix [D] by

$$[D] = [r][r] \tag{2.40}$$

The elements of [r] are related to the flux J_i of component i in an n-component system from the bulk of the alloy to the oxide scale/alloy interface in time t and these relations are [2.39]:

$$J_i = \frac{1}{(\pi t)^{1/2}} \sum_{j=1}^{n-1} (r_{ij}\, \Delta C_j) \qquad (i=1,2,...n-1) \tag{2.41}$$

where ΔC_j corresponds to the difference between alloy bulk and interfacial concentrations of component j ($C_j^o - C_j^i$). Morral and coworkers [2.40] have further assumed that in ternary alloys both solutes are oxidized and their concentrations at the oxide scale/alloy interface are reduced by oxidation. Thus from Eq. (2.41)

it is apparent that whether a solute enhances or inhibits diffusion is reflected in the sign of each corresponding r_{ij}. For example, if r_{ij} is positive, then increasing the concentration of component j in the bulk of alloy will increase the flux of component i to the interface. Recent work [2.40] has indicated that all above mechanisms should be considered in analyzing the third element effects and developing oxidation resistant alloys. However, quantification of the four mechanisms requires a knowledge of the thermodynamic and diffusion properties of the ternary alloy plus oxygen system and the solution of appropriate diffusion equations. The necessary thermodynamic and diffusion data for such treatment is usually as yet unavailable, and a sufficiently detailed oxidation model under appropriate boundary conditions has not been devised.

CHAPTER 3

Literature Review

3.1 Introduction

High temperature materials have been defined [3.1] as those with a melting point (T_M) above 1300°C and possessing a working temperature (T) at a high proportion of the melting point. Characteristically, the ratio T/T_M is greater than 0.5, *i.e.*, useful working temperature is above 650°C [3.1]. Of the metallic materials for use at high temperatures two classes are commercially available. The first, known as the superalloys and stainless steels are based exclusively on alloys of nickel, cobalt or iron and have an upper temperature limit of 1000-1200°C . The second, referred to as the refractory metals and alloys, *i.e.* the group IV-VI elements such as chromium, tungsten, and molybdenum, are frequently used above 1000°C but have limited acceptance because of their high cost or poor surface stability in oxidizing atmosphere.

Clearly, for an alloy to possess any degree of oxidation resistance it must form a dense compact oxide layer completely covering the alloy surface, so that rate of further oxidation is governed by solid state diffusion in the scale. The oxide formed must have a more negative free energy of formation than other oxidation products of the alloy and not allow rapid diffusion of cations or anions. The oxide must not be volatile, or react with water or carbon dioxide, or

have a low melting point. These criteria make all possible oxides except Al_2O_3, Cr_2O_3, and SiO_2 unsuitable for high-temperature oxidation protection.

Only a limited amount of work has been carried out with SiO_2 scales, but it appears that at elevated temperatures, reduction to volatile SiO may occur, or SiO_2 may react with other metal ions to form complex molten oxides, e.g. Fe_2SiO_4 , fayalite, which has a melting point of only 1177°C. The most satisfactory oxides are Al_2O_3 and Cr_2O_3 and accordingly most heat-resistant alloys may be classified either as chromina-formers or alumina-formers. The detrimental effect of large Al contents on the mechanical properties of alloys has limited the development of the alumina-formers although their superior oxidation resistance has long been recognized [3.2]. Cr_2O_3 provides the oxidation resistance in most uncoated superalloys and heat-resisting steels. However, due to limitations in world Cr production and an upper practical limit for use of 1000°C for chromina forming alloys, there is renewed interest in the development of alumina forming alloys [3.3]. Synergistic effects of additions of Al and Si or Al and Cr in combination on the oxidation properties of Fe or Ni have been observed by many investigators [3.4-6], and it is on these alloy additions that this research will focus.

The aim of this chapter is to review the available oxidation results on the Fe-Si-Al, Ni-Cr-Al, and Ni-Si-Al systems.

3.2 Properties of the Fe-Si-Al-O Systems

3.2.1 Thermodynamics of the Fe-Al and Fe-Al-O Systems

Rivlin and Raynor [3.7] have reviewed the Fe-Al system and compiled the

available phase equilibrium data. The Fe-Al phase diagram is shown in Fig. 3.1. Al is a ferrite stabilizer and exhibits a large solubility in bcc iron. The activities of Al and Fe in liquid and solid Fe-Al alloys have been determined by several investigators [3.8-12], and the activity of Al in Fe-Al alloys at 1173 K shows a large negative deviation from Raoult's law at low Al concentrations [3.12].

Kaufman and Nesor [3.13] have calculated excess free energy functions for the Fe-Al system. For instance, the excess free energies, in units of J/mol, for the system in the bcc iron region can be expressed as:

$$G^{\Xi}(N^{\dagger}_{Fe}, N^{\dagger}_{Al}) = N^{\dagger}_{Fe}\, N^{\dagger}_{Al}\, [-\, 58576 - 14.23T + N^{\dagger}_{Al}(117152 - 85.36T)]. \qquad (3.1)$$

Their functions are in good agreement with observed thermochemical values.

Atlas and Sumida [3.14] studied isothermal sections of the Fe-Al-O system in 1958. Several of their important results can be summarized as follows: (1) Fe-Al alloys exist in equilibrium with Al_2O_3 containing only a small amount of iron; (2) Only five compounds are stable in the Fe-Al-O system below 1523 K. These are wustite, hercynite, magnetite, hematite, and alumina; (3) A complete spinel solid solution exists between Fe_3O_4 and $FeAl_2O_4$; (4) FeO dissolves up to 1 wt% Al and is never found in equilibrium with Al_2O_3 because of the intermediate spinel compound; (5). Al_2O_3 and Fe_2O_3 form limited solid solutions, with Fe_2O_3 dissolving a maximum of 24 wt% Al_2O_3 and Al_2O_3 dissolving a maximum of 12 wt% Fe_2O_3. More results as well as equilibrium oxygen pressure diagrams for the Fe-Al-O system at 1073, 1173, and 1273 K have been obtained by Elrefaie and Smeltzer [3.15]. The equilibrium oxygen pressure diagram at 1073 K is given in Fig. 3.2.

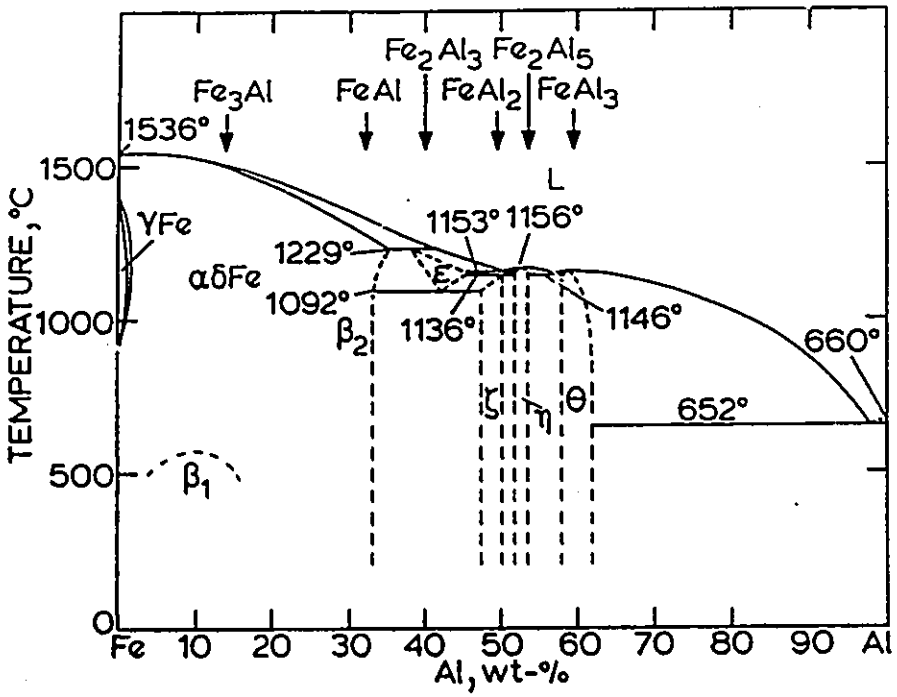

Fig. 3.1 Fe-Al system [3.7]

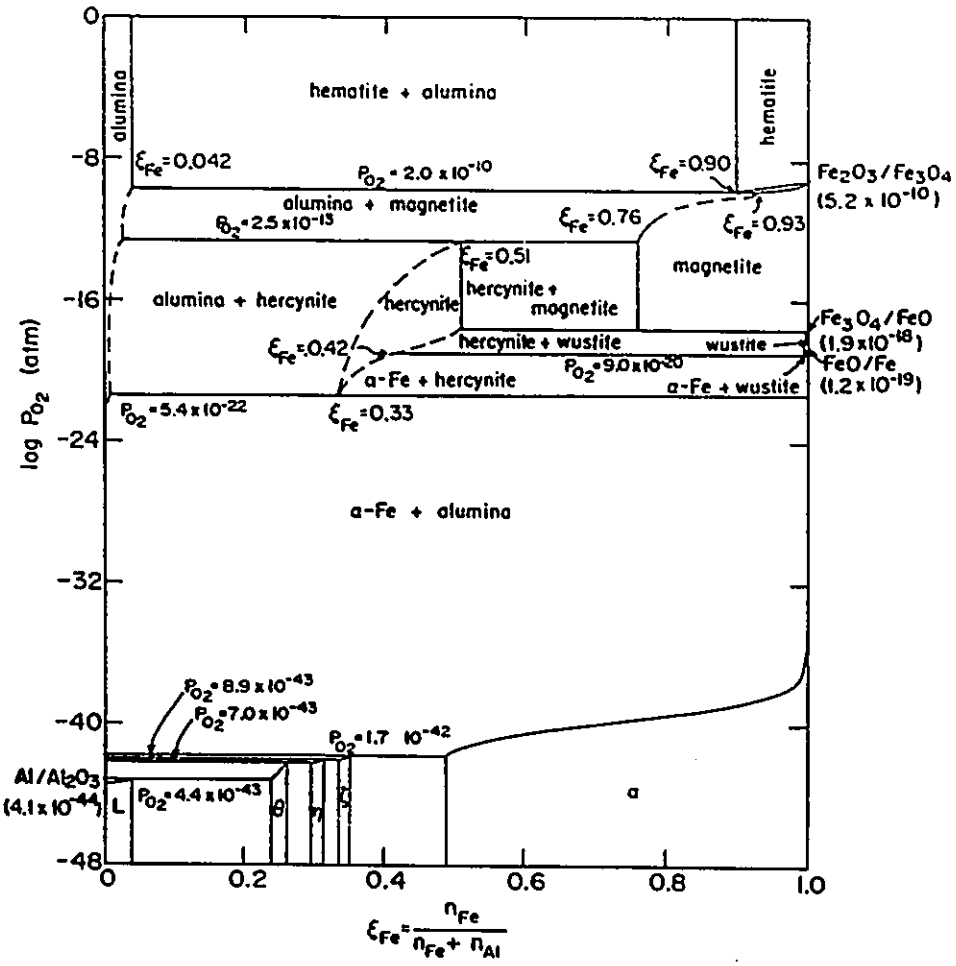

Fig. 3.2 Equilibrium oxygen pressure diagram of the system Fe-Al-O at 1073 K [3.15]

3.2.2 Thermodynamics of the Fe-Si, Al-Si and Fe-Si-Al Systems

The solidus and liquidus are reliably established in the Fe-Si system. Solid solubility of Si in γ-Fe is restricted. Conversely, referring to Fig. 3.3 the solubility of Si in bcc-Fe is extensive — up to 20 at% Si [3.7]. Several investigators have determined the activities of Fe and Si in liquid alloys [3.16-18], but only limited information is available for the solid phases. Schenk *et al.* [3.19] have determined Si activity in dilute Fe-Si alloys at 1329 K and found Si to exhibit a strong deviation from Raoult's law. Vecher *et al.* [3.20] have measured the activity of Fe in dilute Fe-Si alloys over the temperature range of 873-1073 K. Kaufman [3.21] has calculated excess free energy functions for the Fe-Si alloys. In the temperature range of 300-1800 K, the excess free energy of in J/mole α-Fe can be expressed as

$$G^{E}(N^{\dagger}_{Fe}, N^{\dagger}_{Si}) = N^{\dagger}_{Fe}\, N^{\dagger}_{Si}\, [-\, 297064 + 136.82T + N^{\dagger}_{Fe}(167360 - 128.87T)] \quad (3.2)$$

Kaufman did not consider the ordering reactions in the α-Fe region. However his analytical expressions for the Fe-Si system compares well with the observed phase diagram. The Gibbs free energy data for all phases of the Fe-Si system have been evaluated and used to calculate the Fe-Si phase diagram by Lee *et al.* [3.22].

The Al-Si system is a simple eutectic with very limited solid solubilities — 1.59 at% Si in Al and about 0.1 at% Al in Si at 850 K [3.7]. The excess free energy of the system with respect to liquid state can be expressed by [3.23]

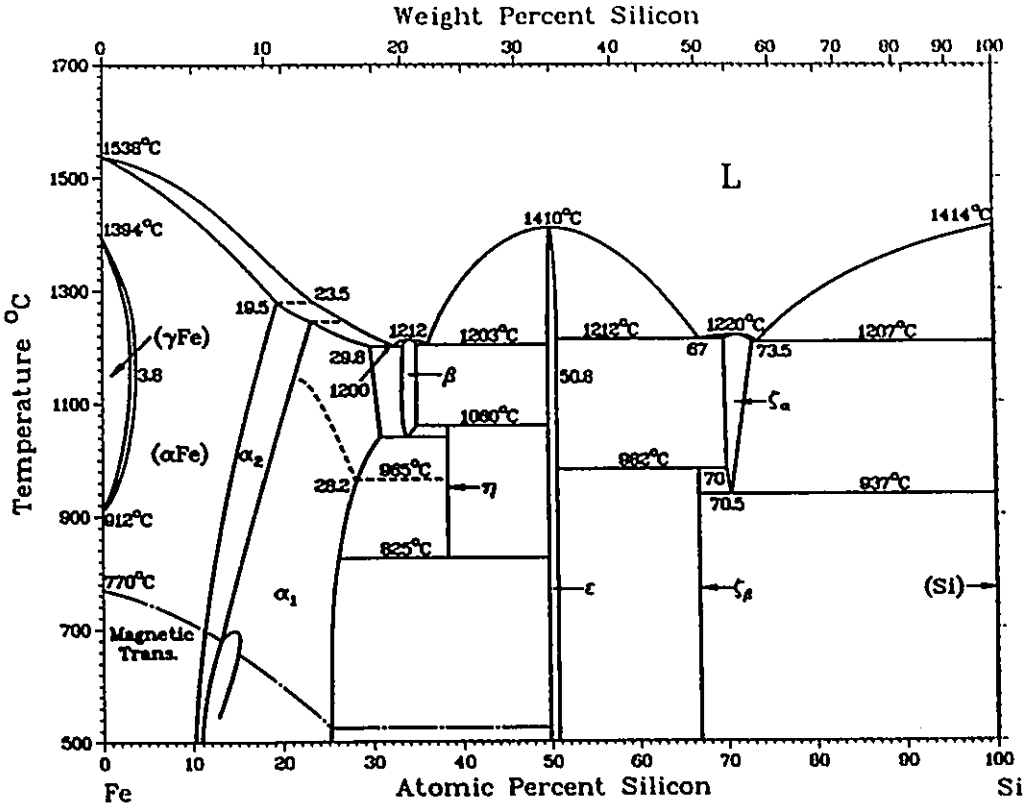

Fig. 3.3 Fe-Si system [3.7]

$$G^{E}(N^{\dagger}_{Si}, N^{\dagger}_{Al}) = N^{\dagger}_{Al}\, N^{\dagger}_{Si}\, [-\, 11179 - 1.29T + (N^{\dagger}_{Al} - N^{\dagger}_{Si})(-\, 4179 + 2.04T) + (N^{\dagger}_{Al} - N^{\dagger}_{Si})^{2}(-\, 3148 + 4.95T) + (N^{\dagger}_{Al} - N^{\dagger}_{Si})^{3}(8698 - 8.58T)]. \quad (3.3)$$

Lattice stabilities of Al and Si in the system are [3.20]

$$^{o}G^{liq}_{Al} - {}^{o}G^{bcc}_{Al} = -\, 627.6 - 6.69T, \text{ and} \quad (3.4)$$

$$^{o}G^{liq}_{Si} - {}^{o}G^{bcc}_{Si} = -\, 6276 - 10.46T. \quad (3.5)$$

Revlin and Raynor [3.7] have reviewed the Fe-Si-Al system and compiled the available phase equilibrium data. Most studies of this system have been confined to Al-rich alloys, although enough data exist to discuss Fe rich ternary alloys. As shown in Fig. 3.4, the αδ Fe primary surface exists over a very wide range of composition. Miyazaki *et al.*[3.24] have found that at 973 K, the range of solid solubility of α-Fe in the Fe-Si-Al system can reach up to 12 at% Si and 25 at% Al. Mitani *et al.* [3.25] have obtained activities in Al rich ternary alloys. The only other study was made by Batalin and coworkers [3.26]. They measured the activity of Al in Fe-(2-10 at% Al) alloys and in Fe-2 at% Al alloys containing Mn, Si, Mo, or Ni at 1861-1923 K. They found that the presence of 1 at% Si would increase the activity of Al in the Fe-2 at% Al alloy up to six times at 1823 K. Activities of Al and Si in the solid Fe-Si-Al system have not yet been experimentally measured or theoretically estimated.

3.2.3 Thermodynamics of the Fe-Si-O and Fe-Si-Al-O Systems

Phase relations for the Fe-Si-O system in the temperature range of

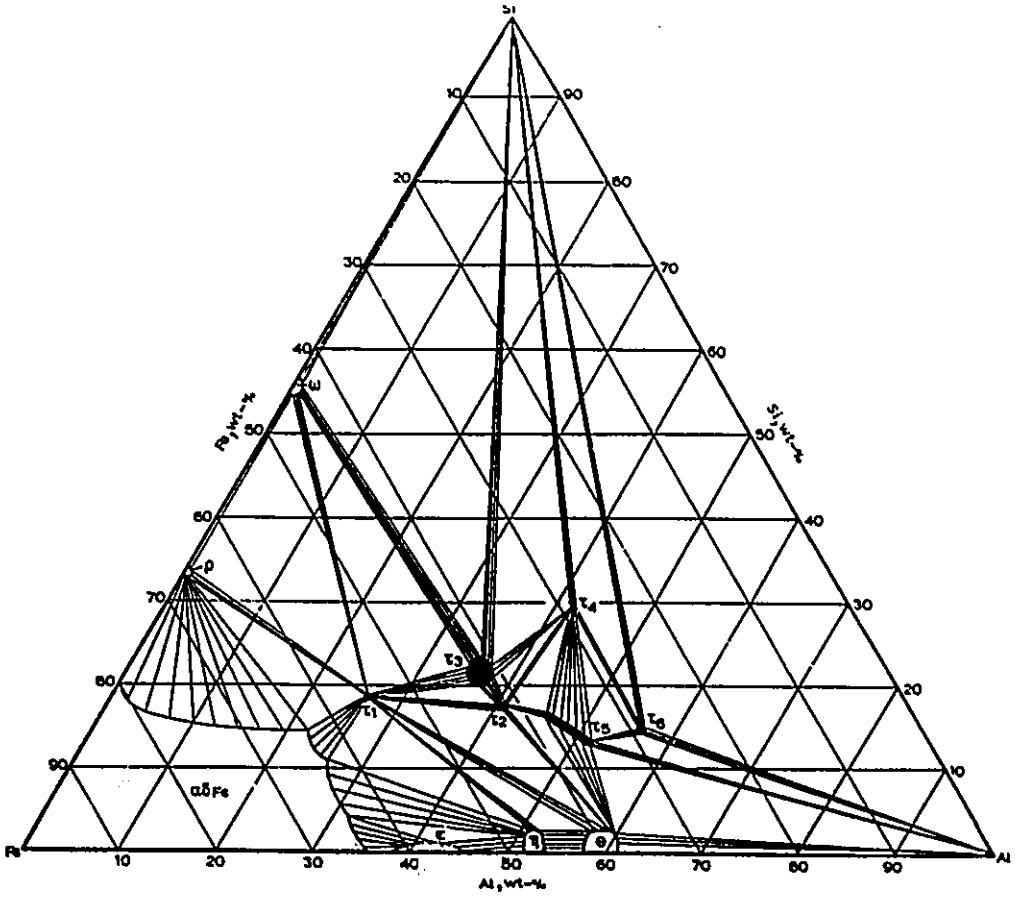

Fig. 3.4 Schematic diagram of phase relations in the system Fe-Al-Si at 1273 K [3.7]

1473-2003 K have been constructed by Iyengar and Philbrook [3.27] with more attention paid to temperatures above 1783 K. However, this temperature range is only localized in the liquid region. Fig. 3.5 shows the phase relations for the solid Fe-Si-O system at 1173 K which was given by Kanz [3.28] to explain his observations on the microstructure of a series of iron-oxide/silica melts. It was derived primarily from a consideration of Schenck's reduction curves for a series of Fe_2O_3-SiO_2 mixtures at 1173 K [3.29]. Joins are shown running from $2FeO{\cdot}SiO_2$ to both Fe_3O_4 and Fe_2O_3. There are some doubts concerning the accuracy of the latter join, however, for Fe_3O_4 has been experimentally found in iron-oxide/silica melts lying in the field Fe_2O_3-$2FeO{\cdot}SiO_2$-SiO_2 of Fig. 3.5 [3.30]. In this study, an isotherm shown in Fig. 3.6 is proposed for the Fe-Si-O system at 1173 K, which covers the work of about 25 investigators in the literature [3.28-47]. The compositions within each phase field must be regarded as being of only schematic significance since no detailed information on the phase fields of iron-silicon oxides is available in the literature.

Information on phase equilibria in the Fe-Si-Al-O system is limited to the work of Muan [3.48-49]. While his data are of considerable importance in the study of slag chemistry in steel-making, it provides limited information in regard to oxide/alloy equilibria.

3.2.4 Diffusion of the Fe-Si-Al-O System

Data on metal diffusion in the αδ-Fe phase of the Fe-Al system have been obtained in several studies [3.50-54], and have been compiled in reference [3.55]. A detailed study by Nishida *et al.* [3.53] on interdiffusion in the α solid

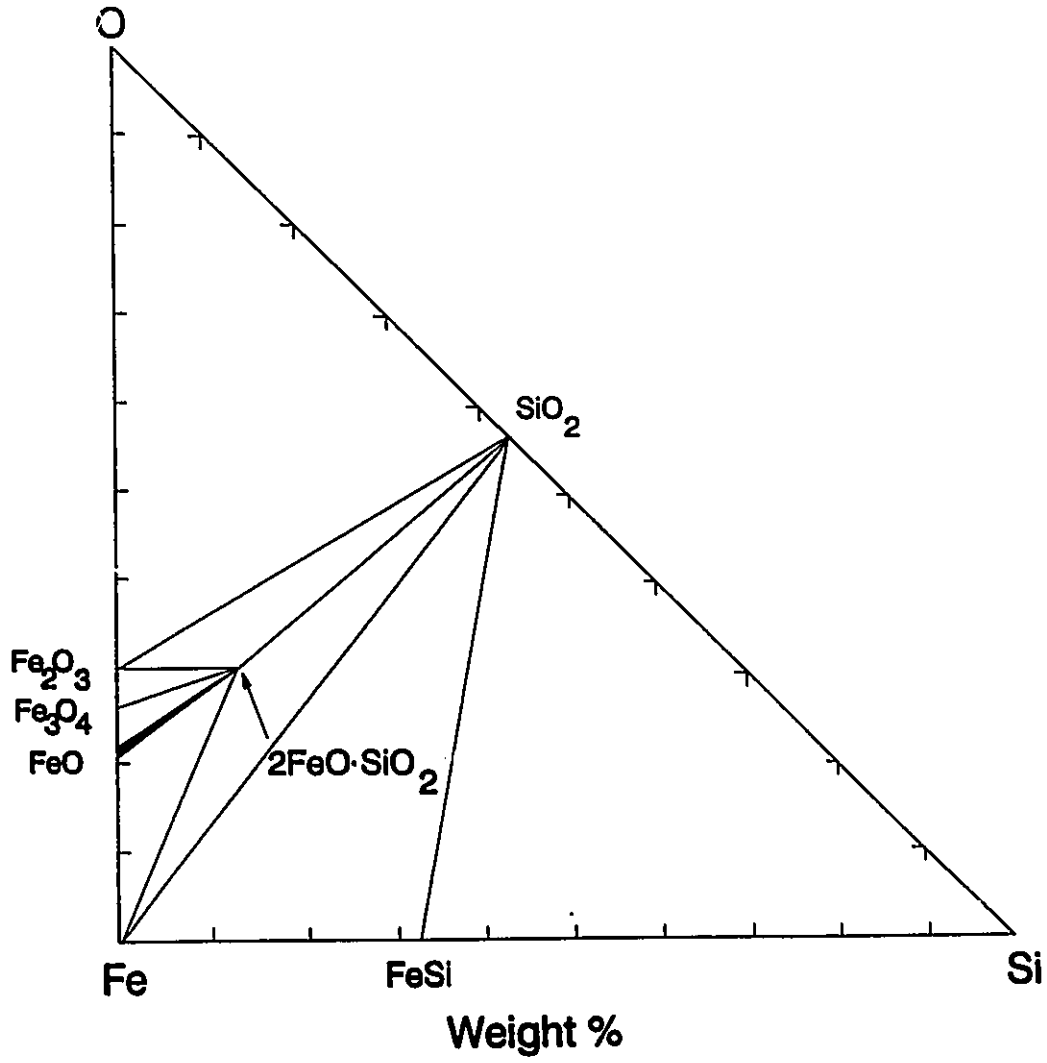

Fig. 3.5 Phase relations in the system Fe-Si-O at 1173 K [3.28]

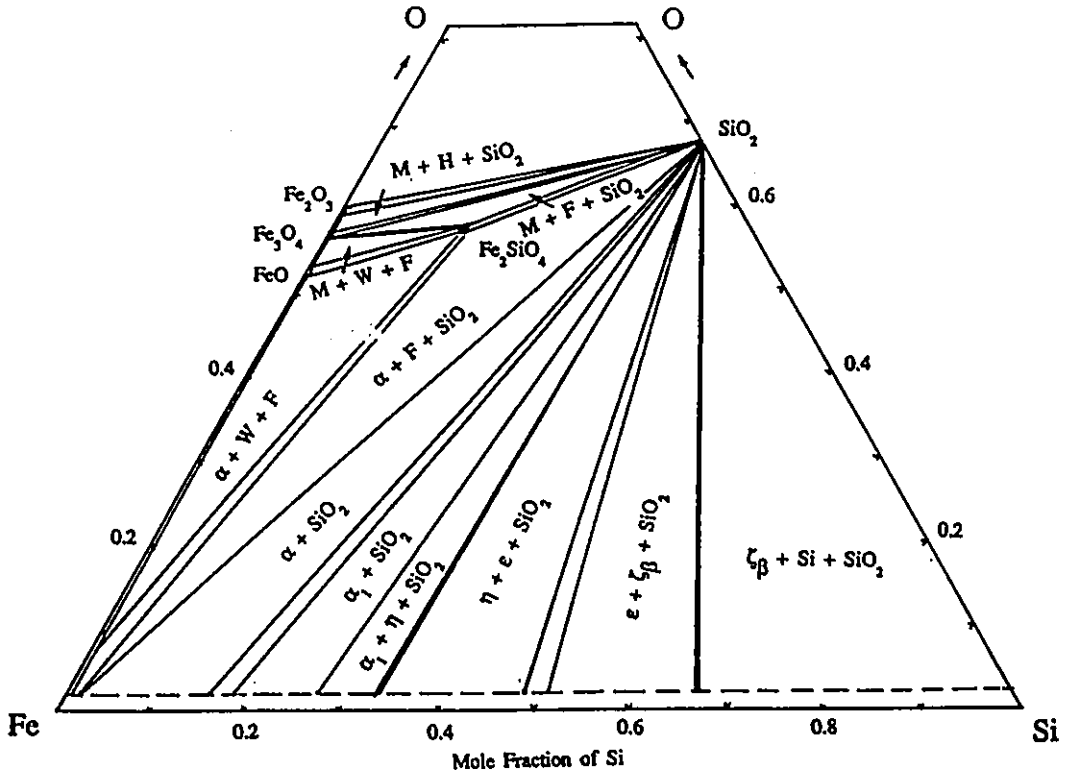

Fig. 3.6 Fe-Si-O isotherm at 1173 K

solution phase at 1073-1373 K found the chemical diffusivity to be strongly dependant on the Al concentration, with maximum values occurring at the order disorder phase boundary. Their data are presented in Fig. 3.7.

Several studies have been carried out to determine the self diffusion coefficients for Si in α-Fe [3.56-59]. Borg and Lai [3.56] found a concentration dependence for D_{Si} over the temperature range 1173-1723 K to be given by

$$D_{Si} = 0.735(1 + 12.4N_{Si})\exp(-219.7\pm1 \text{ kJ}\cdot\text{mol}^{-1}/RT) \text{ cm}^2/\text{sec} \qquad (3.6)$$

for Si mole fraction N_{Si} from 0 to 0.047. Mirani and Maaskant [3.58] studied Si diffusion in Fe-Si alloys containing N_{Si} from 0.0835 to 0.1041 over a temperature range of 1173-1373 K. Their results were consistent with those of Borg and Lai [3.56].

There are no diffusion data available on the Fe-Si-Al alloys. Kositsyn *et al.* [3.60] have measured the chemical diffusion coefficient in β-$Ni_{50\text{-}66}Al_{44\text{-}28}Si_6$ alloys at 1373 K. They found that the addition of 6 at% Si increased the chemical diffusivity 4 to 6 times. The β-Ni phase has an ordered CsCl type super lattice, and hence the results of Kositsyn and coworkers may give some indications of the effect of Si addition in Fe-Al alloys.

Takada and coworkers [3.61-62] have calculated the diffusion coefficient of oxygen in α-Fe, based on measurements of the internal oxidation of Al and Si. For the dilute Fe-Al alloy, over the temperature range 1023-1123 K, D_O is given by

$$D_O = 1.79 \times 10^{-3} \exp(-85.7\pm6.1 \text{ kJ}\cdot\text{mol}^{-1}/RT) \text{ cm}^2/\text{sec} \qquad (3.7)$$

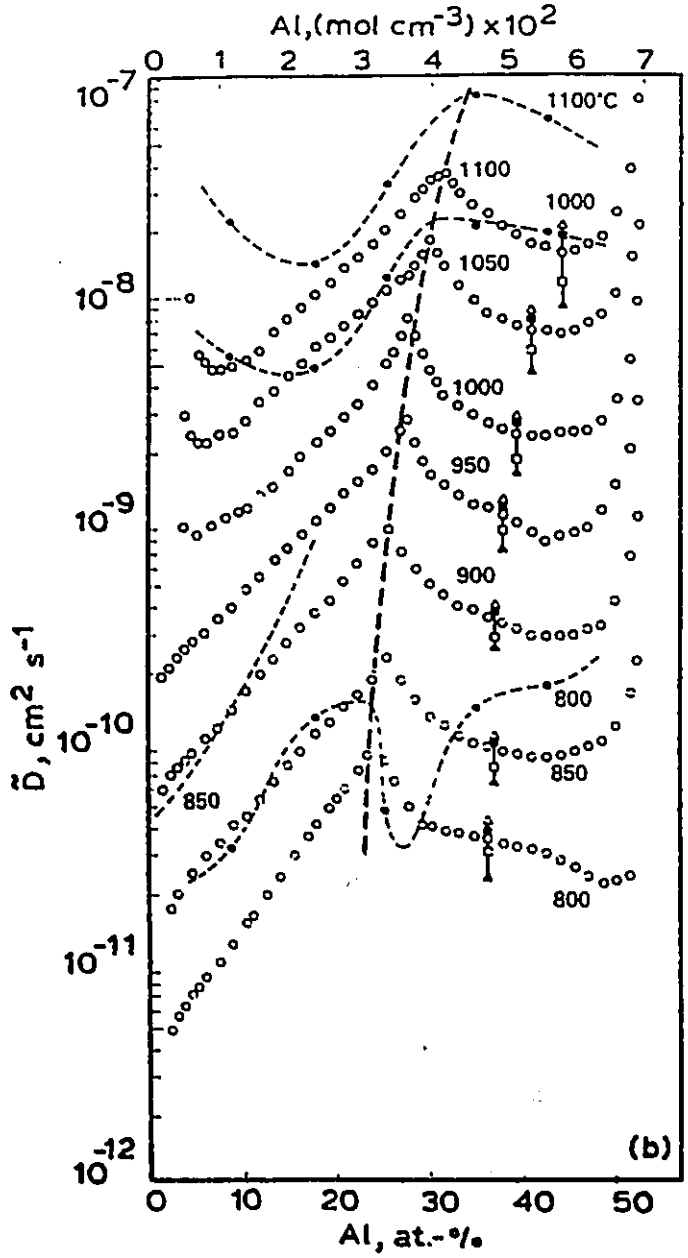

Fig. 3.7 Fe-Al interdiffusion coefficient as function of temperature [3.53]

For the dilute Fe-Si alloy, over the temperature 1023-1173 K, D_O is given by

$$D_O = 2.91 \times 10^{-3} \exp(-89.5 \pm 7.2 \text{ kJ·mol}^{-1}/RT) \text{ cm}^2/\text{sec} \quad (3.8)$$

These two values are in good agreement.

The diffusion properties of the oxides of iron have been discussed in several reviews [3.55, 3.63]. Fe is the mobile species in FeO and Fe_3O_4 [3.64] while in Fe_2O_3, the diffusion coefficients of Fe and O are of the same order of magnitude. The diffusion coefficients determined for ionic species in Fe_3O_4 and Fe_2O_3 show a broad scatter as diffusion in these oxides is strongly influenced by the impurities present and the defect structure of the oxide examined [3.55].

It is generally agreed that the growth of SiO_2 films formed during the thermal oxidation of Si in oxygen is controlled by the inward diffusion of oxygen [3.65-70]. Parabolic growth of the vitreous SiO_2 film and oxygen permeation through this film exhibit a direct dependence on O_2 pressure at temperatures near 1273 K. This behavior has been interpreted as arising from the transport of electrically neutral O_2 molecules through the interstitial spaces of the open SiO_2 network structure. Cawley and coworkers [3.70] have investigated the sequential oxidation of Si using O^{16} and O^{18} isotopes near 1273 K which confirms that oxidation occurs by the transport of electrically neutral interstitial oxygen with a small degree of simultaneous atomic self diffusion in the SiO_2 network. Atkinson and Gardner [3.71] have also determined the chemical diffusion coefficient of Fe^{3+} in amorphous SiO_2 over the temperature range 773-1273 K.

The structure and transport properties of α-Al_2O_3 have been reviewed by Kroger [3.72] and Prescott and Graham [3.73]. Most considerations of diffusion

properties of Al_2O_3 pertain to the α phase — the thermodynamically stable modification. α-Al_2O_3 is ionic in character with a high lattice energy and a large band gap, consequently the concentration of electronic and ionic defects is very low. Ionic defects are reported to be the major defect species, electrons and holes being minorities [3.73]. Fig. 3.8 summarizes self diffusion coefficients for oxygen and aluminum, obtained from measurements of diffusion, ionic conductivity, and creep on single and polycrystalline materials. In general, for oxygen, grain boundary diffusion is greater than lattice diffusion, while for aluminum both processes are approximately equal and of the same magnitude as oxygen grain boundary diffusion. The lattice diffusion of oxygen is likely to occur by a vacancy mechanism, whereas aluminum diffusion may be by movement of charged interstitials [3.74]. Iron tracer diffusion coefficients in a polycrystalline α-Al_2O_3 sample containing 0.1% SiO_2 and 0.05% Fe have been determined over a temperature range of 1073-1273 K by Izvekov and Gorbunova [3.75]. They obtained values of lattice and grain boundary diffusion coefficients of

$$D_L = 9.18 \times 10^{-8} \exp(-112.97\ kJ \cdot mol^{-1}/RT)\ cm^2/sec \qquad (3.9)$$

$$D_B = 1.37 \times 10^{-8} \exp(-46.01\ kJ \cdot mol^{-1}/RT)\ cm^2/sec \qquad (3.10)$$

3.2.5 Oxidation of Fe-Al Alloys

The oxidation of Fe-Al alloys has been the subject of a number of investigations [3.55, 3.76-85] and several reviews [3.86-87]. Prescott and Graham [3.87] have summarized the more recent studies in this field.

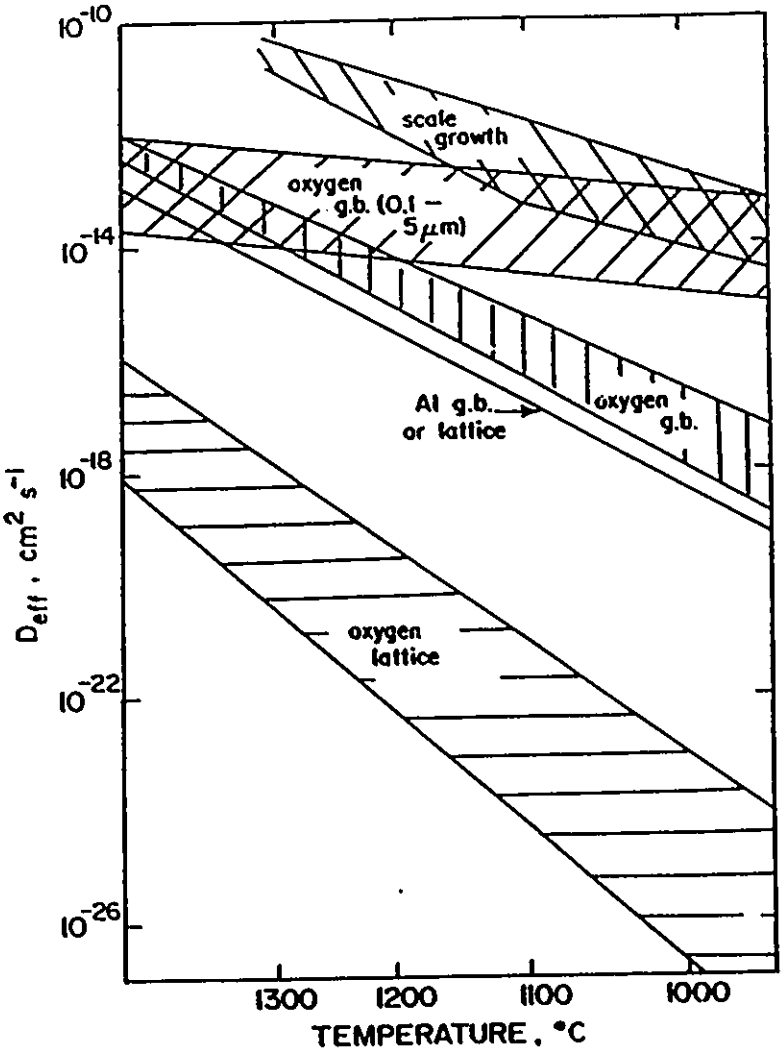

Fig. 3.8 A comparison of lattice and grain boundary diffusivies for Al and O diffusion in single-crystal and polycrystalline Al_2O_3 as a function of temperature [3.132]

The influence of very small Al additions (*i*.e. 0.006 to 0.18 at%) has been shown to increase the overall growth rate of scales when compared with pure iron [3.76-77]. Bateman and Rolls [3.77] reported that at 1173 K scales were morphologically similar to those formed on pure Fe and consisted of FeO, Fe_3O_4 and Fe_2O_3 The increased rate was interpreted as being due to the Wagner-Hauffe effect whereby some Fe^{2+} ions are replaced by Al^{3+} ions in the Fe_3O_4 or FeO lattice. This causes an increase in cation vacancy concentration and raises the rate of diffusion of Fe ions.

At higher Al concentrations the rate of oxidation decreases progressively below that of pure Fe and scale morphology is modified by the presence of Al_2O_3 or $FeAl_2O_4$ precipitates near the scale/metal interface [3.76-78]. Cations migrate slower through Al-containing oxides than FeO, and therefore the formation of Al_2O_3 or $FeAl_2O_4$ is generally considered responsible for decreasing the scaling rate and providing a barrier to the outward diffusion of ferrous cations. Ahmed and Smeltzer [3.55] have observed that at 1173 K the scale formed on 1.5-3 at% Al alloys is duplex in nature, with an $Fe_2O_3/(Fe,Al)_3O_4$ scale and an internal oxidation zone containing $FeAl_2O_4$-Al_2O_3 precipitates. At a higher Al concentration (5 at%) the scale was initially similar to that formed on the lower Al content alloys, but the ultimate composition was $Fe_2O_3/FeAl_2O_4/Al_2O_3$.

At about 1073 K, alloys with about 6 at% Al may be classified as Al_2O_3 formers as a transition occurs from internal to external oxidation [3.87]. The scales formed at such Al contents, however, are not fully protective and may permit the development of nodular growths of bulky Fe oxide. Such nodules are associated with an increased oxidation rate. The composition of the nodules is complex, with an outer layer of Fe_2O_3 covering the Fe_3O_4, FeO, and Al_2O_3 inside

[3.79]. Tomaszewicz and Wallwork [3.79] have proposed a mechanism to explain the formation of nodules. FeO and Al_2O_3 develop as products of the transient stage of oxidation, but Al_2O_3 soon forms a complete layer, isolating the FeO from the alloy which soon becomes depleted in Al. Any crack or flaw in the Al_2O_3 layer allows oxygen to react with the Fe-enriched alloy and nucleate a nodule around the FeO. Eventually, the whole nodule oxidizes to Fe_2O_3. If the Al content of the alloy is low, for example 6 at%, the nodules may coalesce to form a continuous layer. Otherwise, an Al oxide healing layer may develop at the base of the nodule, thus ending its growth. The nodules tend to be formed at highly stressed areas such as specimen edges and corners, or at regions of crystal misfit such as grain boundaries or triple points.

The minimum Al concentration required to eliminate nodule formation has not been widely investigated. Wallwork and McGirr [3.80] have suggested that this concentration at 1073 K is 16 at%. At 1273 K, 10 at% Al is reported to be enough to form an external protective scale, although other findings are conflicting [3.87].

The oxidation of Fe-Al alloys containing more than 10 at% Al has been investigated by Graham and coworkers [3.85] at 1273 K and 1373 K in 5×10^{-3} torr of oxygen. Protective α-Al_2O_3 scales have been formed. ^{18}O/SIMS profile analysis indicates that the scales grow primarily by oxygen transport, but the growth may be more complex than the SIMS profiles would suggest.

3.2.6 Oxidation of Fe-Si Alloys

The oxidation behavior of Fe-Si alloys has been studied by numerous

investigators [3.88-96]. In general, binary Fe-Si alloys oxidize in a manner similar to Fe-Al alloys with progressive additions reducing the rate of oxidation, until selective oxidation leads to the formation of a protective SiO_2 scale.

Scales on Fe-Si alloys containing less than 1.5 at% Si when formed in air and oxygen above 973 K appear bulky and are similar to those formed on pure iron [3.88-89]. The major part of the scale is composed of an inner FeO layer which contains precipitates of Fe_3O_4 and Fe_2SiO_4. This is adjacent to a dense layer of Fe_3O_4 and finally a thin and compact Fe_2O_3 layer exists at the scale/gas interface.

Logani and Smeltzer [3.90-92] have studied the oxidation of Fe-3 at% Si in CO/CO_2 atmosphere at 1163 and 1273 K. The oxidation kinetics indicated that initially there were regions of variable reaction rate, followed by regions of linear reaction behavior. In the initial stage of oxidation, the alloy was covered with an amorphous SiO_2 film and the film was then consumed by growth of $FeO\text{-}Fe_2SiO_4$ nodules. In conjunction with growth of the nodules externally, oxygen diffusion into the underlying alloy led to precipitation of SiO_2 as α-tridymite. These precipitates were converted to fayalite by reaction with FeO, Fe, and oxygen. The onset of linear kinetics corresponded to complete coverage of the surface by the nodules. Eventually the scale became composed of an external FeO layer and an inner $FeO\text{-}Fe_2SiO_4$ conglomerate layer interspersed with discontinuous Fe_2SiO_4 bands.

Atkinson [3.97] has analyzed the selective oxidation behavior of Fe-Si alloys and predicted the Si concentrations required to develop and maintain a protective SiO_2 film as a function of temperature. This analysis predicts that 5.5 at% Si is required at 873 K, which is in good agreement with experimental

observations [3.93-95]. At Si concentrations greater than 4-5.8 at% at temperatures above 873 K, scales formed on Fe-Si alloys have been identified as exclusively SiO_2 [3.93-95]. When initially formed and only a few angstroms thick, these scales were difficult to analyze and probably existed as an amorphous oxide or very small crystallites. With continued oxidation this converted to high temperature crystobalite and eventually in part or wholly to tridymite.

At higher temperatures, Si concentrations higher than those predicted by Atkinson [3.97] are required to form protective SiO_2 films, apparently due to the enhanced permeability of the SiO_2 film to Fe. Adachi and Meier [3.96] have studied the oxidation behavior of Fe-Si alloys containing 9-33 at% Si in air at temperatures of 1173-1373 K. At 1173 K parabolic kinetics were observed, with all alloys forming a SiO_2 protective oxide. At 1373 K the oxidation kinetics, although slow, were essentially linear due to the outward permeation of Fe through the slowly growing SiO_2 film to form Fe_2O_3 at the scale/gas interface. The oxide formed at this temperature was duplex in nature, made up of an outer Fe_2O_3 layer and an inner layer of crystalline SiO_2, or in the case of 9 at% Si alloy, Fe_2O_3/Fe_2SiO_4. The Fe_2O_3 formation was not related to cracking of the SiO_2 layer.

3.2.7 Oxidation of Fe-Si-Al Alloys

Only limited results are available for the oxidation of Fe-Al-Si alloys [3.4, 3.98-106]. The earliest systematic study into the oxidation of this system appears to be that by Brandes [3.98], who oxidized alloys containing additions of less than 8 at% Al and Si, over a temperature range of 873-1273 K. Tests were carried out in dry and wet air, steam, and various synthetic gases containing SO_2

or H_2O. However scale identification was not carried out. It was shown that the silicon-aluminum steels were markedly superior to calorized mild steels and only slightly inferior to an 18Cr-8Ni stainless steel under oxidizing conditions. The alloy containing 4.8 at% Si and 2 at% Al was found to be the most resistant at temperatures between 873 K and 1373 K, scaling at a rate approximately five orders of magnitude slower than pure iron. Random, isolated oxide nodules were observed only on low aluminium (<1-2 at%) alloys. The growth of nodules was attributed to the presence of sulphur segregation, as the addition of sufficient Mn prevented their formation.

Tuck [3.99] examined the oxidation of a commercial Fe-3.4 at% Si-0.6 at% Al alloy. Protective duplex scales were formed at temperatures of 1073-1273 K on alloys oxidized in oxygen. The outer layer was composed of Fe_2O_3, while the inner layer was found to be Si rich, and too thin for identification by X-rays. No internal oxidation of Si or Al was apparent. The oxidation rate reduction achieved by the Al addition was greater than if the Si content of the alloy had been increased by a similar amount.

The oxidation of alloys containing less than 10 at% of Si and Al was studied by Von Fraunhofer and Pickup [3.100-102] over a temperature range of 773-973 K. An alloy with good oxidation resistance, Fe-3.2 at% Al-3.6 at% Si formed a thin adherent scale (2-3 μm thick) interspersed with iron oxide nodules 40-50 μm in diameter after 40 hours oxidation in air at 973 K [3.102]. Electron microprobe analysis (EPMA) indicated that the scale was aluminum rich, probably Al_2O_3 with no detectable silicon. Nodules were iron-rich and aluminum could be detected in their lower hemisphere. An alloy which was considered to have excellent oxidation resistance, i.e. Fe-1.67 at% Al-2.03 at% Si, also formed a

thin scale (2-3 μm) interspersed with iron-rich nodules. However, EPMA revealed not an aluminum rich scale, but rather a scale with duplex morphology. This was composed of an Fe rich outer layer and a Si rich (14% enrichment) inner layer where about 4% Al enrichment was also detected. X-ray diffraction of the oxide was attempted, but its structure could not be determined. Ternary alloys with a much higher Al content were studied by Boggs [3.103]. Samples containing up to 15 at% Al and 5 at% Si were oxidized in wet or dry oxygen at 700 torr, over a temperature range of 1073-1366 K. At 1073 K, even the alloy having the lowest concentration of Al and Si (3.7 at% Al and 3.8 at% Si) was much more oxidation resistant than the Fe-9.8 at% Al binary alloys. At 1366 K, ternary alloys containing 9.6-11.5 at% Al and 1.9-3.3 at% Si oxidized at a similar rate, which is about 2 orders of magnitude less than that of an Fe-9.8 at% Al alloy and 5 times less than that for an Fe-16 at% Al alloy. The ternary alloys resisted nodular oxide growth, while the Fe-9.8 at% Al binary alloy was almost completely covered by nodules. However, only limited compositional identification of the oxides formed was carried out. The adherent protective oxides were identified by X-ray diffraction as α-Al_2O_3, and spectrographic analysis did not show a significant amount of Si in the oxide films. The mechanism of the oxidation resistance of these ternary alloys was speculated to be the oxygen getter effect of Si.

The oxidation behavior of Fe-Al-Si alloys containing up to 10 at% Al and 10 at% Si prepared by ingot metallurgy (IM) and powder metallurgy (PM) in air and oxygen was investigated in the temperature range of 1173-1373 K [3.104]. Exceptional scale adherence and extremely low oxidation rates, in both the isothermal and the cyclic tests, were observed for the Al_2O_3-scale-forming Fe-Al-Si PM alloys below 1273 K; the IM alloys, in comparison, showed poor scale

adherence. The mechanism was explained to be that the extremely fine grain size of the PM alloys enhanced outward aluminum diffusion with a corresponding reduction in the critical concentration of Al, hastening the establishment of a protective layer. This would shorten the transient stage of oxidation, and accelerate healing of the Al_2O_3 scale in case of scale breakdown. Rapid diffusion of Al to the scale/alloy interface was confirmed by the observation that no depletion of Al could be detected at a distance of 2 μm from the interface by EDAX.

Corkum [3.4] has studied the oxidation behavior of several binary and ternary Fe-Al-Si alloys at 1173 K in an oxidizing atmosphere of 100 torr of dry oxygen. At oxidation times of up to 20 hours, the order of increasing oxidation resistance was: Fe-6 at% Al < Fe-5 at% Si < Fe-5.6 at% Al-0.9 at% Si < Fe-4.3 at% Al-4.2 at% Si < Fe-5.2 at% Si -0.8 at% Al. The parabolic oxidation rates of the ternary Fe-Al-Si alloys are of approximately the same magnitude as those for binary Fe-Al alloys containing Al in excess of 16 at%. The ternary alloys formed to varying degrees an Al_2O_3 scale of convoluted morphology. This scale was interspersed by iron oxide nodules on the low Si content alloy. Si was only detected in the oxide formed on these alloys during the initial stages of oxidation. In light of the greatly enhanced oxidation properties of certain alloy compositions, the gettering effect was not considered to be the sole mechanism leading to oxidation resistance for the ternary alloys and the synergistic effect of Al and Si additions was thought to be possibly due to strong ternary interactions increasing the Al diffusion flux to the oxide/alloy interface. However, this hypothesis warrants more detailed analysis and future investigation.

3. 3. Properties of the Ni-Cr-Al-O System

3.3.1 Thermodynamics of the Ni-Cr-Al-O System

Ni and Al are both face-centered cubic metals. The phase diagram for the Ni-Al system has been accurately determined [3.108]. In the temperature range 600-1200 °C, up to 12-17 at% Al can be dissolved in Ni to give a disordered *f.c.c.* solid solution (γ). Three intermetallic phases are formed with non-stoichiometric ranges: Ni_3Al (γ'), NiAl (β) and Ni_2Al_3 (δ).

Al activities in Ni-Al alloys containing 15-60 at% Al have been determined by Steiner and Komarek [3.108] in the temperature range 1200-1300 K. Ni activities were calculated from these data by integrating expressions of the Gibbs-Duhem equation [3.109]. Kaufman and Nesor [3.13] have calculated excess free energy functions for the Ni-Al alloys.

Nash [3.110] has reviewed the Ni-Cr system and compiled the available phase equilibrium data. The Ni-Cr phase diagram has often been investigated but its shape above 1473 K is still controversial. Cr and Ni activities in the system have been measured by Davies and Smeltzer [3.111], and Mazandarany and Pehlke [3.112] over the temperature range 900-1100 °C and 1000-1300 °C, respectively. There appears to be reasonable agreement among various investigators below 25 at% Cr, indicating a slight negative deviation of the activity of Cr from ideality.

The activity of Al in solid Al-Cr alloys has been measured by Johnson *et. al.* [3.113] between 890 and 1126 °C and concentrations from 13 to 80 at% Al. The maximum solid solubility of Al in Cr was confirmed to be 43 at% Al at 1000 °C. Kaufman and Nesor [3.114] have calculated excess free energy functions for the

Al-Cr system.

Very little work has been done on the thermodynamics of ternary Ni-Cr-Al alloys. Malkin and Pokidyshev [3.115] measured the activity of Al in solid alloys using an e.m.f. technique and observed strong negative deviations from ideality which decreased on passing from the Ni-Al binary system to the ternary system. Odorka and Argent [3.116] determined the activities of Ni, Cr and Al in the isothermal ternary section and its constituent binary systems at 1150 °C. The deviation of Al activity from ideality decreases on passing from the Ni-Al binary system to the Ni-Cr-Al system. The effect of the addition of Cr on the activity of Al is small.

Elrefaie [3.117] has used solid electrolyte galvanic cells to measure various thermodynamic properties of the Ni-Al-O system. The dissolution pressures of both Al_2O_3 and NiO were measured. Dissociation pressure values of Al_2O_3 equilibrated with the alloy from the relation

$$P_{O_2} = a_{Al}^{-4/3} \exp\left[\frac{2\Delta G_f^{\circ}(Al_2O_3)}{3RT}\right] \qquad (3.11)$$

were also calculated using the Ni-Al activity data [3.109]. All of these values were used to determine the Ni-Al-O equilibrium oxygen pressure diagrams at 1213 and 1273 K.

The equilibrium oxygen pressures for Cr-Ni alloys coexisting with Cr_2O_3, NiO, and $NiCr_2O_4$ have also been determined at 1173, 1273, and 1373 K [3.111]. These pressures were related to compositional determinations of the solid phases and the Cr-Ni-O isotherms.

The mole fractions of oxygen solubilities in nickel at the dissociation

pressures of NiO at 1373 and 1473 K have been measured by Smithells and Ransley [3.118] and by Seybolt [3.107] as 0.00048 and 0.00044, respectively.

3.3.2 Diffusion of the Ni-Cr-Al-O System

The temperature dependence of interdiffusion coefficients in the Ni-Al alloys with up to 11 at% Al has been given by Green and Swindells [3.135] as

$$\tilde{D}_{NiAl} = 1.3 \exp(-257\ kJ \cdot mol^{-1}/RT) \qquad cm^2/sec \qquad (3.12)$$

Values of the tracer diffusion coefficients of Al in Ni have been measured as 1.0×10^{-10} and 5.1×10^{-10} cm^2/sec [3.120], and of Cr in Ni as 1.3×10^{-10} and 3.9×10^{-10} cm^2/sec [3.121], at 1373 and 1473 K, respectively.

Ternary interdiffusion coefficients have been measured by Nesbitt and Heckel [3.122] in the Ni solid solution γ (*f.c.c.*) phase of the Ni-Cr-Al system at 1373 and 1474 K. The results have showed that for all concentrations, $\tilde{D}_{AlAl}$ is two to three times greater than $\tilde{D}_{CrCr}$. $\tilde{D}_{AlAl}$ and $\tilde{D}_{AlCr}$ increase with increasing Al concentration but show little dependence on Cr. $\tilde{D}_{CrAl}$ is strongly dependent on Cr concentration alone whereas $\tilde{D}_{CrCr}$ is more strongly dependent on Al. The concentration dependence of the four interdiffusion coefficients as functions of both the Al and Cr concentrations in at% is given in Table 3.1.

Values of the oxygen diffusion coefficients in Ni and dilute Ni-Al alloys have been found to range from 2.27×10^{-7} to 2.45×10^{-7} cm^2/sec at 1373 K [3.123-124], and from 3.7×10^{-7} to 10.0×10^{-7} cm^2/sec at 1473 K [3.125].

Table 3.1 Concentration Dependence of Interdiffusion Coefficients [3.122]

$$\tilde{D}_{ij} \times 10^{10}\ cm^2/sec = a_0 + a_1 N_{Al} + a_2 N_{Cr} + a_3 N_{Al}^2 + a_4 N_{Cr}^2$$

	a_0	a_1	a_2	a_3	a_4
1373 K					
D_{AlAl}	1.229	0.073	-0.0083	0.01008	0.00016
D_{AlCr}	0.0116	0.0923	-0.0010	0.00016	0.00002
D_{CrAl}	0.0766	-0.0153	0.0837	0.00062	-0.00146
D_{CrCr}	0.7833	-0.0123	0.0247	0.00096	-0.00057
1473 K					
D_{AlAl}	1.9708	1.3837	0.1845	0.0061	-0.0032
D_{AlCr}	0.1350	0.2804	-0.0164	0.0352	0.0004
D_{CrAl}	-1.4108	0.3285	0.4724	-0.0133	-0.0080
D_{CrCr}	3.2061	-0.5584	0.1836	0.0704	-0.0037

3.3.3 Oxidation of Ni-Al Alloys

The most extensive investigation of Ni-Al oxidation prior to 1970 was done by Pettit [3.126]. The major portion of his paper presented a description of oxidation mechanisms in the temperature range 1200 to 1600 K, which were formulated from experimental findings on oxidation behavior and thermodynamic and diffusional factors. The mechanism controlling oxidation depended on Al content of the alloy and temperature as shown in Fig. 3.9. In mechanism I, the critical mole fraction, $N^*_{Al_2O_3}$, for exclusive external oxidation is considered. If the critical mole fraction of oxide is not exceeded, internal oxidation occurs. In mechanisms II and III, the critical mole fraction of oxide is always exceeded but the Al flux in the alloy and oxide is variable. With high Al flux in the alloy, a stable

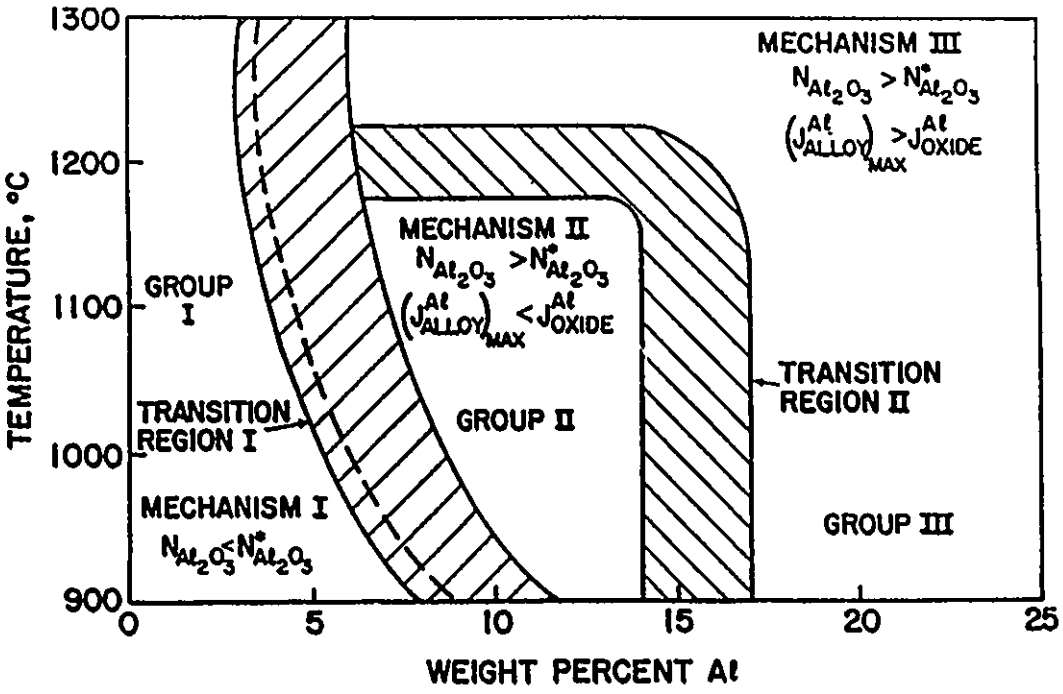

Fig. 3.9 Dependence of the groups of data and the mechanism of oxidation for Ni-Al alloys on temperature and alloy composition. [3.126]

protective alumina layer is formed on the alloy surface.

The oxidation rates of Ni-Al alloys with Al concentration less than 8 at% are greater than those of unalloyed Ni in the temperature range 1073-1473 K [3.126-132]. These alloys form an external duplex scale consisting of outer and inner layers of Al-doped NiO and NiO-$NiAl_2O_4$ aggregates, respectively, and an Al-depleted alloy zone containing $NiAl_2O_4/Al_2O_3$ precipitates. The increased oxidation rate of the alloy over the pure metal has been attributed to the doping effect of Al on NiO which results in an increase in the concentration of Ni vacancies and thereby an increase in the diffusion of Ni [3.127]. The presence of $NiAl_2O_4$ in the inner layer increases the oxygen activity gradient across the scale which also increases the oxidation rate, although the spinel phase also acts as a diffusion barrier, reducing the first effect. In studies of the growth of the $NiAl_2O_4/Al_2O_3$ subscales, deviations from the classical Wagner models of internal oxidation have been observed by analyses of the data for the rates of penetration of the subscales [3.128-129]. It has been suggested that the results can be accounted for if it is assumed that the precipitates in the internal oxidation zone do influence the diffusivity of oxygen. The precipitates themselves block the transport of oxygen, while the incoherent boundaries between the precipitates and the metal matrix provide enhanced diffusion paths for this species [3.130-131]. The relative contribution of the boundary transport, however, diminished rapidly with temperature in the range of 1073 to 1373 K [3.131]. Hindam and Whittle [3.132] have suggested that the boundaries between the precipitates and the metal matrix are ineffective in accelerating oxygen transport at 1473 K.

Alloys with higher Al concentrations form a continuous Al_2O_3 layer with or without NiO nodules scattered in it depending on the Al composition of the alloy.

It has been suggested that the transition from internal precipitation to the growth of a continuous layer occurs by preferential precipitation of Al_2O_3 particles at alloy grain boundaries [3.128-129]. The minimum Al concentration for the transition from internal to external oxidation in Ni-Al alloys was investigated by Pettit [3.126] in oxidizing conditions such that only Al_2O_3 was stable (CO/CO_2 = 0.2). He found that Al concentrations equal to or greater than approximately 10 and 8 at% were required to cause the transition at 1373 and 1473 K, respectively. In an oxidizing environment where Al_2O_3 and NiO are both stable, Pettit [3.126], Hindam and Whittle [3.132], and Smeltzer *et al.* [3.133] found that Al concentrations of 14 and 12 at% were required for the transition at 1373 and 1473 K, respectively. The critical volume fraction of Al_2O_3 for the transition has been found by Hindam and Whittle [3.132] to be 0.33 at 1473 K in air.

3.3.4 Oxidation of Ni-Cr-Al Alloys

Giggens and Pettit [3.5] have experimentally studied the oxidation characteristics of Ni-Cr-Al alloys and determined the minimum bulk Al concentrations necessary to form and grow a protective Al_2O_3 scale on the alloys isothermally oxidized at 1273, 1373 and 1473 K. They have found that Cr enables the formation of a continuous, external layer of Al_2O_3 on Ni-Cr-Al alloys at lower Al concentrations than would be necessary if the Cr were not present in the alloy. Similar results on this ternary alloy system have been obtained by many other investigators [3.134-137]. The experimental data are sufficient to permit the construction of 'oxide maps' which delineate the composition ranges for formation of different types of oxide scales at a particular isotherm. An example of such a

map is given in Fig. 3.10, which illustrates that the oxidation behavior of Ni-Cr-Al alloys which can be divided into three broad groups [3.138]. Dilute alloys form an external scale of NiO and a subscale of Cr_2O_3 and/or Al_2O_3. Alloys with sufficiently high concentration of Cr and relatively low concentrations of Al form a continuous external scale of Cr_2O_3 with Al being internally oxidized to form a Al_2O_3 subscale. Alloys with sufficiently high concentrations of Al form a thin continuous external layer of Al_2O_3 only.

Many investigators [3.5, 3.134-138] have attempted to explain the beneficial effect of Cr addition on the formation of the exclusive external scale of Al_2O_3 on Ni-Cr-Al alloys. One possibility is that the presence of Cr enhances the diffusion rate of Al in the alloys. However, measurements of the interdiffusion coefficients in the Ni-Cr-Al alloys by Nesbitt and Heckel [3.122] appear to negate this idea. The ternary diffusion coefficients affecting the diffusion of Al in the system ($\tilde{D}_{AlAl}$ and $\tilde{D}_{AlCr}$) show only slight increases with increasing Cr concentration. Therefore, the diffusion flux of Al in the alloy to the oxide/alloy interface will not be significantly affected by the Cr additions. Another possibility which has been suggested [3.5, 3.134-138] is that Cr acts as a getter and is oxidized during the transient stage of oxidation, reducing the inward oxygen flux to the alloy or oxygen solubility in the alloy, so α-Al_2O_3 tends to develop as a complete surface layer instead of just as an internal oxide. At 1173-1273 K, Cr also tends to stabilize α-Al_2O_3 rather than the less protective γ-Al_2O_3 modification. However, the amount of Cr required to act as a secondary getter would not be sufficient to form a continuous Cr_2O_3 external scale in the absence of Al, and this appears to be a requirement of the Wagner hypothesis for the secondary gettering effect [3.139]. The other possibility suggested by

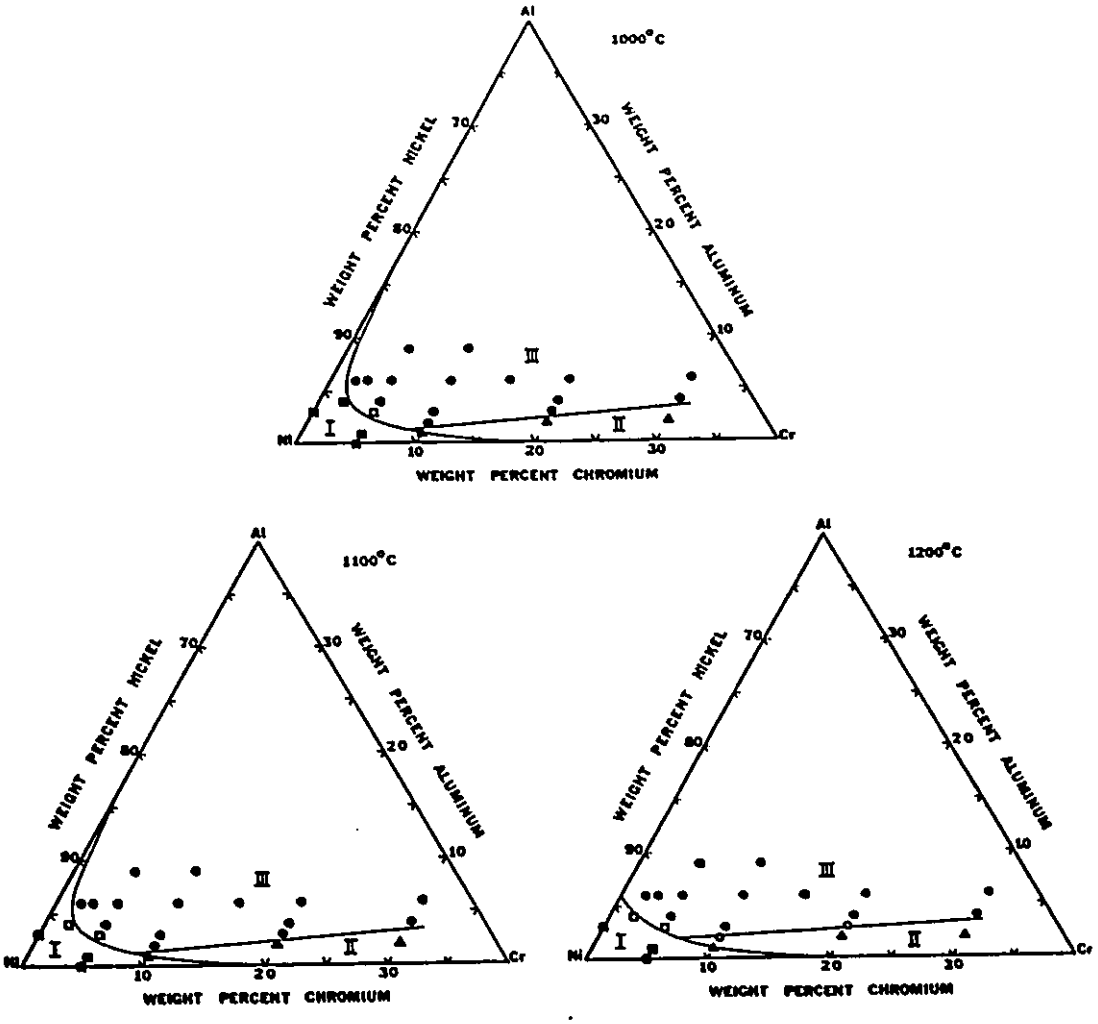

Fig. 3.10 Oxide maps showing the compositional limits for formation of different types of oxide scales on Ni-Cr-Al alloys. (I) NiO scale + Cr_2O_3 or Al_2O_3 ppts. (II) Cr_2O_3 scale + Al_2O_3 ppts. (III) Al_2O_3 scale only. [3.5]

Whittle [3.139] is that the Al oxidizes internally initially to form a dispersion of Al_2O_3 particles and then these particles act as nucleation sites promoting the formation of a Cr_2O_3 scale. The continuous Cr_2O_3 layer lowers oxygen potential at the surface to a point where Al can diffuse outwards to develop a continuous Al_2O_3 scale, beneath the Cr_2O_3 layer. These are all qualitative rather than quantitative explanations.

3.4 Oxidation Properties of the Ni-Si-Al System

The analytical descriptions of thermodynamic properties of the solution and compound phases in the Ni-Si system have been given by Kaufman [3.20]. In the temperature range 300-1800 K, the excess free energy of the *f.c.c.* solution of Si in Ni can be expressed as

$$G^E(N_{Ni}^{\dagger}, N_{Si}^{\dagger}) = N_{Ni}^{\dagger} N_{Si}^{\dagger} [26434564 - 62.01T + N_{Si}^{\dagger}(40.0T - 126106)] \quad (3.13)$$

in units of J/mol.

The phase relationships and terminal solid solubility in Ni at 1373 K have been determined for the Ni-rich portion of the ternary system Ni-Al-Si [3.140]. Fig. 3.11 illustrates an isothermal section of the Ni-Al-Si system at 1373 K, showing also the solvus line for the γ solid solution region at 1173 K.

Diffusion coefficients of Si in Ni have been measured as a function of temperature [3.141]

$$D_{Si} = 1.5 \exp(-258.15 \pm 8 \text{ kJ·mole}^{-1}/RT) \quad \text{cm}^2/\text{sec} \quad (3.14)$$

Experimental data are not yet available for the interdiffusion coefficients in the solid solution region of the Ni-Si-Al system.

Several studies have been reported [3.142-145] on the oxidation of Ni-Si alloys. The addition of up to 1 at% Si increases the oxidation rate of Ni at 1173 K, and further addition in the Si concentration of up to 5 at% will reduce it [3.142]. Douglass and coworkers [3.144] found that the oxidation kinetics of Ni-4 at% Si and Ni-9 at% Si alloys did not follow a parabolic rate law over the range of 873-1273 K, and that 6.6 at% Si was required for the transition from internal oxidation to continuous silica film formation.

Little information is available on to the oxidation of Ni-Si-Al alloys. Pettit and Meier [3.145] found that for certain ranges of Al concentration, Si retarded the development of external Al_2O_3 scales.

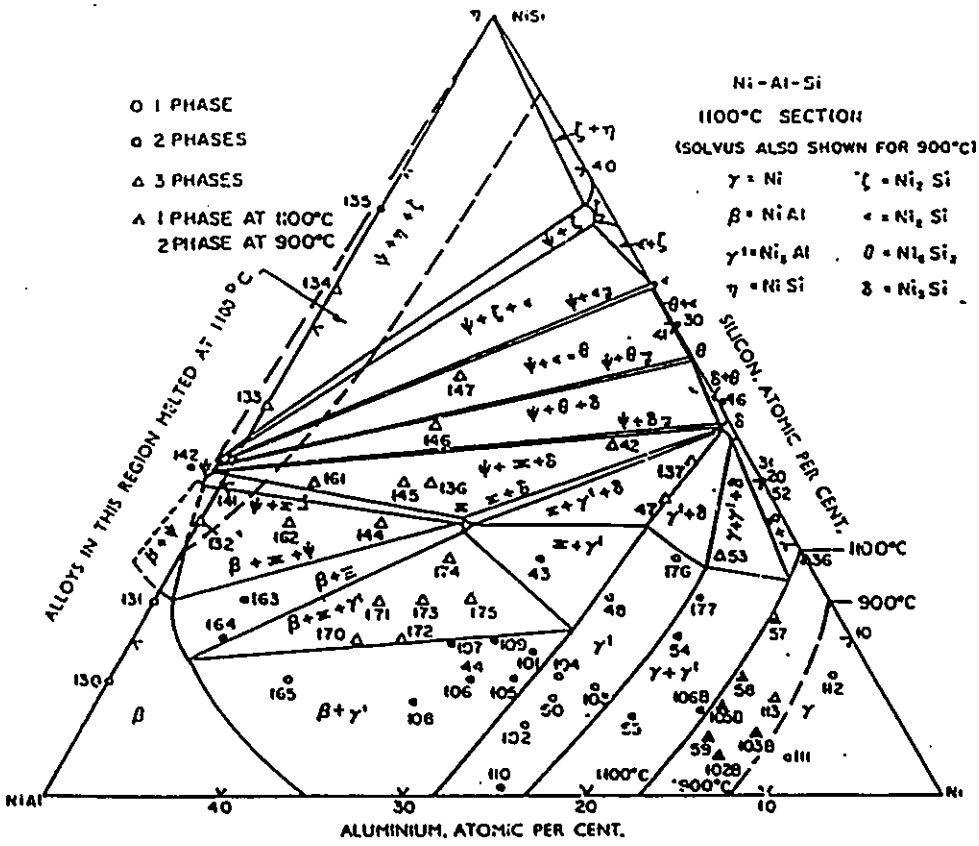

Fig. 3.11 Isothermal section of the system Ni-Si-Al at 1373 K, showing also the γ solvus for 1173 K. [3.140]

CHAPTER 4

Theoretical Considerations for Ternary Alloy Oxidation

4.1 Introduction

In the previous chapters it has been shown that a study of high temperature oxidation of a ternary alloy involves consideration of thermodynamic and kinetic interactions in the alloy plus oxygen system. At high temperatures the reaction rates are usually so fast that the overall reaction rate is controlled by transport phenomena [4.1]. In considering such transport controlled processes, it is usually convenient to recognize the concept of "local equilibrium". In the case of alloy oxidation, the reaction gas and the alloy are separated by an oxide layer soon after the beginning of the reaction. The total free energy change of the reaction takes place over a large distance. Taking a volume element of sufficiently small size, one can regard the microscopic volume element as being substantially in equilibrium within itself even during the course of a rapid reaction. This local equilibrium is characterized by a chemical potential of each element of species. In a case where the condition of local equilibrium prevails, the requirement that the various diffusing species are conserved at the interfaces leads to a coupling or interdependence of diffusion in the oxide and alloy phases. This interplay between diffusion in the two phases involves both kinetic and thermodynamic considerations. These considerations furnish the basis for a

theoretical study of the oxidation of ternary alloys.

In this chapter, models are proposed in order to explain more fully the oxidation behavior of ternary alloys. No attempt is made (nor is it possible) to give an overall quantitative description of oxidation of ternary alloys; rather, some of the main features of alloy oxidation are discussed briefly. These features include: (a) oxygen solubility in ternary alloys; (b) kinetics of selective internal oxidation in the absence or presence of an external scale; (c) the transition from internal to external oxidation; and finally (d) the protective scale formation and growth.

4.2 Oxygen Solubility in Ternary Alloys

Data on oxygen solubility in solid alloys as a function of alloy composition are usually not available because of the difficulty of these experiments. This fact limits the application of a thorough theoretical approach to the oxidation of alloys. To overcome this difficulty, one may use a method given by Smith [4.2] to estimate the variation of oxygen solubility with alloy composition, using the Gibbs-Duhem equations for the oxide and alloy phases in equilibrium and the Wagner formalism for the activity coefficients. Unfortunately, Smith's model focused only on oxygen solubility in binary alloys. In this study, his analysis is expanded in order to include the oxygen solubility behavior in a ternary alloy.

For a four component system of solutes 1, 2, 3, and solvent 4 at constant temperature and pressure, one may apply the Gibbs-Duhem equation for phase I and II in equilibrium ($\mu_i^I = \mu_i^{II}$) as

$$N_1^I\, d\mu_1 + N_2^I\, d\mu_2 + N_3^I\, d\mu_3 + N_4^I\, d\mu_4 = 0 \qquad (4.1)$$

$$N_1^{II} d\mu_1 + N_2^{II} d\mu_2 + N_3^{II} d\mu_3 + N_4^{II} d\mu_4 = 0 \qquad (4.2)$$

Recalling that $\Sigma\, N_i = 1$, and subtracting Eq. (4.2) from Eq. (4.1) one obtains

$$(N_1^{II}-N_1^I)(d\mu_1 - d\mu_4) + (N_2^{II}-N_2^I)(d\mu_2 - d\mu_4) + (N_3^{II}-N_3^I)(d\mu_3 - d\mu_4) = 0 \qquad (4.3)$$

For a dilute solution if Wagner formalism is assumed to be applicable, one obtains

$$d\mu_1 = RT[dN_1/N_1 + \varepsilon_1^1\, dN_1 + \varepsilon_1^2\, dN_2 + \varepsilon_1^3\, dN_3] \qquad (4.4)$$

$$d\mu_2 = RT[dN_2/N_2 + \varepsilon_1^2\, dN_1 + \varepsilon_2^2\, dN_2 + \varepsilon_2^3\, dN_3] \qquad (4.5)$$

$$d\mu_3 = RT[dN_3/N_3 + \varepsilon_1^3\, dN_1 + \varepsilon_2^3\, dN_2 + \varepsilon_3^3\, dN_3] \qquad (4.6)$$

$$d\mu_4 = RT[-\, dN_1 - dN_2 - dN_3] \qquad (4.7)$$

where in the case of the solvent, component 4, it is assumed that if N_1, N_2, and N_3 approach zero, then $N_4 \to 1$ in which case Raoultian ideality is achieved and the activity coefficient of the solvent $\gamma_4 = 1$. Substitution of these four equations into Eq. (4.3) results after simplification in the following equation:

$$\left(\frac{a}{N_1} - bN_1 - cN_2 - dN_3 + e\right)dN_1 + \left(\frac{f}{N_2} - cN_1 - gN_2 - hN_3 + j\right)dN_2 + \left(\frac{l}{N_3} - dN_1 - hN_2 - mN_3 + p\right)dN_3 = 0 \qquad (4.8)$$

where $a = N_1^{II}$, $b = (1+\varepsilon_1^1)$, $c = (1+\varepsilon_1^2)$, $d = (1+\varepsilon_1^3)$, $e = (1+\varepsilon_1^1)N_1^{II} + (1+\varepsilon_1^2)N_2^{II} + (1+\varepsilon_1^3)N_3^{II} - 1$, $f = N_2^{II}$, $g = (1+\varepsilon_2^2)$, $h = (1+\varepsilon_2^3)$, $j = (1+\varepsilon_2^2)N_2^{II} + (1+\varepsilon_1^2)N_1^{II} + (1+\varepsilon_2^3)N_3^{II} - 1$, $l = N_3^{II}$, $m = (1+\varepsilon_3^3)$, $p = (1+\varepsilon_3^3)N_3^{II} + (1+\varepsilon_1^3)N_1^{II} + (1+\varepsilon_2^3)N_2^{II} - 1$. In Eq. (4.8), the mole fractions refers to phase I. The superscript 'I' has been dropped for purposes of visual clarity.

If phase II is a small phase field in which the solubility of component 3 and 4 are very small, then N_3^{II} and $N_4^{II} \rightarrow 0$. This describes the condition of a stoichiometric compound of the type M_xO_y, when O and M are components 1 and 2 and $N_1^{II} = y/(x+y)$, and $N_2^{II} = x/(x+y)$. Referring to Eq. (4.8), one can determine by integration the precise equation defining the effect of addition of component 3 on the solubility of 1 in phase I when N_2 is fixed. The integrated result is

$$a \ln N_1 - \frac{bN_1^2}{2} - cN_1N_2 - 2dN_1N_3 + eN_1 - hN_2N_3 - \frac{mN_3^2}{2} + pN_3 = q \qquad (4.9)$$

where q is an integration constant. Now for $N_1 \ll 1$, equation (4.9) may be simplified by neglecting the second and fifth term so that

$$a \ln N_1 - cN_1N_2 - 2dN_1N_3 - hN_2N_3 - \frac{mN_3^2}{2} + pN_3 = q \qquad (4.10)$$

To find the value of q, let $N_2 = N_3 = 0$ (and thus $N_1 = N_1^o$, the solubility of 1 in phase I for the 1-4 binary) in Eq. (4.10) to yield

$$q = a \ln N_1^o \qquad (4.11)$$

Thus the solubility equation is

$$N_1^{II} \ln N_1 - [(1 + \varepsilon_1^2)N_2 + 2(1 + \varepsilon_1^3)N_3] N_1 = \frac{(1 + \varepsilon_3^3)}{2} N_3^2 + (1 + \varepsilon_2^3)(N_2 - N_2^{II})N_3 - (1 + \varepsilon_3^3)N_1^{II}N_3 + N_3 + N_1^{II} \ln N_1^o \quad (4.12)$$

For another case when N_3 is fixed, the dependence of the solubility of 1 in phase I on the concentration of 2 can be given by Eq. (4.8) as

$$\left(\frac{dN_1}{dN_2}\right)_{N_3} = \frac{-N_2^{II}+(1+\varepsilon_2^2)[(N_2)^2-N_2N_2^{II}]+(1+\varepsilon_1^2)N_2(N_1-N_1^{II})+(1+\varepsilon_2^3)N_2N_3+N_2}{N_1^{II}-(1+\varepsilon_1^1)[(N_1)^2-N_1N_1^{II}]-(1+\varepsilon_1^2)N_1(N_2-N_2^{II})-(1+\varepsilon_1^3)N_1N_3-N_1} \frac{N_1}{N_2} \quad (4.13)$$

At the minimum solubility of 1 in phase I, $\left(\frac{dN_1}{dN_2}\right)_{N_3} = 0$. Therefore N_2^m, at which the minimum solubility of 1 occurs, would satisfy the equation given by

$$-N_2^{II}+(1+\varepsilon_2^2)(N_2^m)^2+(1+\varepsilon_1^2)N_1N_2^m+(1+\varepsilon_2^3)N_2^mN_3-(1+\varepsilon_2^2)N_2^mN_2^{II}-(1+\varepsilon_1^2)N_2^mN_1^{II}+N_2^m = 0 \quad (4.14)$$

Thus N_2^m would be a function of the concentration of component 3.

For a ternary A-B-C alloy plus oxygen system, if 1, 2, 3, and 4 refer respectively to oxygen, the most reactive metal B, the third element C and the solvent A, one may use the above theory to quantitatively describe the oxygen solubility behavior in the alloy beneath a stoichiometric oxide scale of BO_v as a function of alloy composition. In particular, one can quantitatively determine whether the addition of the third element C into the A-B alloy does or does not reduce the oxygen solubility in the alloy by solving or plotting Eq. (4.12).

4.2 Kinetics of Selective Internal Oxidation of Ternary Alloys

4.2.1 Kinetics in the Absence of an External Scale

This section gives details of the treatment of the kinetics of internal oxidation of an A-B-C ternary alloy in the absence of an external scale. The analysis deals with the case when oxidation conditions favor the simultaneous formation of the metal solute oxides of both B and C. This is essentially an extension to ternary alloy cases of classical models of internal oxidation of binary alloys [4.3-4].

Consider a planar specimen of a ternary alloy A-B-C in which B and C are dilute solutes which form very stable oxides. Assume the ambient oxygen partial pressure is too low to oxidize A but high enough to oxidize both B and C. Atomic oxygen diffuses into the specimen from the surface ($x = 0$) in the positive x-direction and combines with the outward diffusing solutes, B and C, at $x = \xi$ to form $xCO_y \cdot (1\text{-}x)BO_v$ particles. Since the solute metal oxides are very stable, the concentrations of solutes remaining dissolved in the alloy within the internal oxidation zone and of oxygen beyond the zone could be very low. A schematic illustration of the concentration profiles under these conditions is given in Fig. 4.1.

The diffusion of oxygen within the internal oxidation zone is determined by Fick's second law as

$$\frac{\partial N_O}{\partial t} = D_O \frac{\partial^2 N_O}{\partial x^2} \tag{4.15}$$

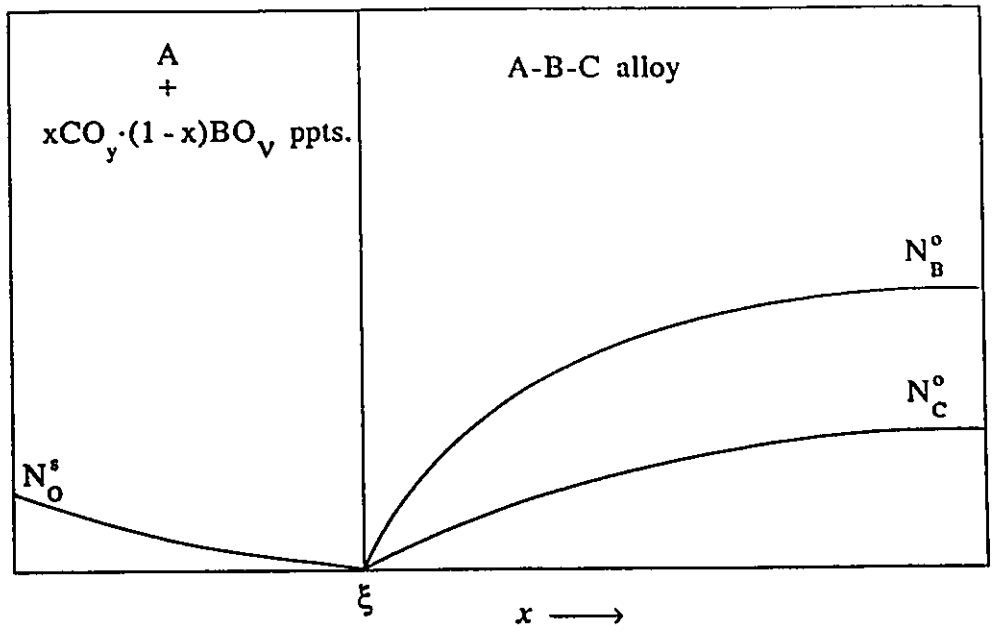

Fig. 4.1 Schematic illustration of concentration profiles of internal oxidation

where D_O is the diffusivity of oxygen in the base metal. We assume that the depth of penetration of the internal oxidation zone ξ is a parabolic function of time t such that

$$\xi = 2\gamma(D_O t)^{1/2} \tag{4.16}$$

where γ is a dimensionless parameter. The solution of Eq. 4.1 subject to the boundary conditions illustrated in Fig. 4.1 will be of the form

$$N_O = N_O^s - \frac{N_O^s}{erf(\gamma)} \, erf\left[\frac{x}{2(D_O t)^{1/2}}\right] \tag{4.17}$$

where N_O^s is the mole fraction of dissolved oxygen at alloy surface. The

concentration gradient of oxygen at the reaction front $x = \xi$ is then

$$\left.\frac{\partial N_O}{\partial x}\right|_{\xi} = -\frac{N_O^s \exp(-\gamma^2)}{(\pi D_O t)^{1/2}\mathrm{erf}(\gamma)} \tag{4.18}$$

The diffusion of the two solutes, B and C, in the alloy is also determined by Fick's second law in a form of matrix as

$$\frac{\partial (N)}{\partial t} = [D]\frac{\partial^2 (N)}{\partial x^2} \tag{4.19}$$

where (N) is the one-column matrix of mole fractions of B and C given as

$$(N) = \begin{bmatrix} N_C \\ N_B \end{bmatrix} \tag{4.20}$$

and [D] is the matrix of interdiffusion coefficients of the A-B-C alloys given as

$$[D] = \begin{bmatrix} D_{CC} & D_{CB} \\ D_{BC} & D_{BB} \end{bmatrix} \tag{4.21}$$

Following the general method given by Toor [4.5] and discussed in §2.2.2, the solutions of Eq. (4.19) may be given by

$$N_C = \sum_{k=1}^{2} \theta_{Ck} U_k + \sum_{k=1}^{2} \theta_{Ck} W_k \mathrm{erf}\left(\frac{x}{2(D_k t)^{1/2}}\right), \text{ and} \tag{4.22}$$

$$N_B = \sum_{k=1}^{2} \theta_{Bk} U_k + \sum_{k=1}^{2} \theta_{Bk} W_k \operatorname{erf}\left[\frac{x}{2(D_k t)^{1/2}}\right] \tag{4.23}$$

where θ's are the elements of the eigenvector matrix, [θ], of the diffusivity matrix [D]. Differentiation of Eq. (4.22) and (4.23) yields

$$\left.\frac{\partial N_C}{\partial x}\right|_{\xi} = \sum_{k=1}^{2} \theta_{Ck} W_k \frac{\exp[-\gamma^2 (D_O/D_k)]}{(\pi D_k t)^{1/2}} \tag{4.24}$$

$$\left.\frac{\partial N_B}{\partial x}\right|_{\xi} = \sum_{k=1}^{2} \theta_{Bk} W_k \frac{\exp[-\gamma^2 (D_O/D_k)]}{(\pi D_k t)^{1/2}} \tag{4.25}$$

W_k is obtained by solving Eq. (2.18) and (2.21) subject to the boundary conditions for B and C illustrated in Fig. 4.1:

$$W_k = \frac{(\theta^C_{Ck} N^o_C + \theta^C_{Bk} N^o_B)/|\theta|}{\operatorname{erfc}[\gamma (D_O/D_k)^{1/2}]} \qquad k = 1, 2 \tag{4.26}$$

where θ^C_{Ck} and θ^C_{Bk} are the cofactors of element θ_{Ck} and θ_{Bk}, respectively. $|\theta|$ is the determinant of [θ]. N^o_C and N^o_B is the bulk mole fraction of B and C in the alloy, respectively.

The reaction involves the mixture formation of precipitated oxides of both B and C, $xCO_y \cdot (1-x)BO_V$, could be written as

$$xC + (1-x)B + [xy + (1-x)v]O = xCO_y \cdot (1-x)BO_V \tag{4.27}$$

where x represents the relative fraction of CO_y precipitated in the internal oxidation zone. At a first approximation, it may be assumed as $N_C^o/(N_C^o + N_B^o)$. This satisfies the restriction that if $N_C^o = 0$, *i.e.*, for the case of binary A-B alloy, only BO_v would form. Equating the stoichiometric flux of oxygen and the solutes arriving in the region of the reaction front $x = \xi$, one obtains

$$\lim_{\varepsilon \to 0} \left[- D_O \frac{\partial N_O}{\partial x}\bigg|_{\xi-\varepsilon} = \frac{xy + (1-x)v}{(1-x)} \left\{ D_{BC} \frac{\partial N_C}{\partial x}\bigg|_{\xi+\varepsilon} + D_{BB} \frac{\partial N_B}{\partial x}\bigg|_{\xi+\varepsilon} \right\} \right] \tag{4.28}$$

Substituting Eq. (4.18), (4.22), and (4.23) into Eq. (4.28) one obtains

$$\frac{D_O^{1/2} N_O^s \exp(-\gamma^2)}{erf(\gamma)} = \frac{xy + (1-x)v}{(1-x)|\theta|} \sum_{k=1}^{2} \frac{F_k \exp[-\gamma^2 (D_O/D_k)]}{D_k^{1/2} \operatorname{erfc}[\gamma (D_O/D_k)^{1/2}]} \tag{4.29}$$

where

$$F_k = (D_{BC}\theta_{Ck} + D_{BB}\theta_{Bk})(\theta_{Ck}^C N_C^o + \theta_{Bk}^C N_B^o) \qquad k = 1, 2 \tag{4.30}$$

At this point the problem remaining is to evaluate the parameter γ so that Eq. (4.16) may be used to express the penetration of the internal oxidation zone. A graphical or numerical solution of Eq. (4.29) is required to obtain γ for substitution into Eq. (4.16) but for most practical problems limiting cases may be applied, and then mathematical asymptotical analysis may be used.

(a) $\gamma \ll 1$ and $\gamma(D_O/D_k)^{1/2} \gg 1$ (*i.e.*, diffusion of oxygen in the alloy is more important in determining the kinetics of internal oxidation). For this case,

the following asymptotical expansions may be made

$$\exp(-\gamma^2) \approx 1 - \gamma^2 \tag{4.31}$$

$$\mathrm{erf}(\gamma) = 2\gamma/\pi^{1/2} \tag{4.32}$$

$$\mathrm{erfc}[\gamma(D_O/D_k)^{1/2}] = \exp[-\gamma^2(D_O/D_k)]/[(\pi D_O/D_k)^{1/2}\gamma] \tag{4.33}$$

and Eq. (4.29) reduces to

$$\gamma = \left[\frac{N_O^s\ (1-x)\ |\theta|}{2[x_y\ +\ (1-x)v]\ \sum_{k=1}^{2} \frac{F_k}{D_k}} \right]^{1/2} . \tag{4.34}$$

When $x = 0$, $N_C^o = 0$, and those interdiffusion coefficients involving solute C are eliminated, Eq. (4.34) will reduce to

$$\gamma = \left[\frac{N_O^s}{2\ v\ N_B^o} \right]^{1/2} \tag{4.35}$$

which is exactly the same as obtained in the classic models of internal oxidation of binary alloys [4.3]. Substitution of Eq. (4.34) into Eq. (4.16) yields

$$\xi = \left[\frac{2\ N_O^s\ (1-x)\ |\theta|\ D_O}{[x_y\ +\ (1-x)v]\ \sum_{k=1}^{2} \frac{F_k}{D_k}} \right]^{1/2} t^{1/2} \tag{4.36}$$

(b) $\gamma \ll 1$ and $\gamma(D_O/D_k)^{1/2} \ll 1$ (*i.e.*, diffusion of alloying elements is

important). For this case, besides Eqs. (4.31-32) the following asymptotical expansions are also made

$$\exp[-\gamma^2(D_o/D_k)] \approx 1 - \gamma^2(D_o/D_k) \tag{4.37}$$

$$\mathrm{erfc}[\gamma(D_o/D_k)^{1/2}] \approx 1 - 2\gamma(D_o/D_k)^{1/2}/\pi^{1/2} \approx 1 \tag{4.38}$$

Therefore, Eq. (4.29) reduces to

$$\gamma = \frac{N_o^s\ (1-x)|\theta|(\pi D_o)^{1/2}}{2[x_y + (1-x)\nu]\sum_{k=1}^{2}\frac{F_k}{D_k^{1/2}}} \tag{4.39}$$

which can be further reduced to the same form as in the case of binary alloys ($x = 0$, $N_C^o = 0$) [4.4]

$$\gamma = \frac{N_o^s\ (\pi D_o)^{1/2}}{2\nu N_B^o\ D_B^{1/2}} \tag{4.40}$$

Substitution of Eq. (4.39) into Eq. (4.16) yields

$$\xi = \frac{N_o^s\ D_o(1-x)|\theta|\pi^{1/2}}{[x_y + (1-x)\nu]\sum_{k=1}^{2}\frac{F_k}{D_k^{1/2}}}\ t^{1/2} \tag{4.41}$$

4.3.2 Kinetics in the Presence of an External Scale

In most practical cases internal oxidation of alloys is associated with the formation of an external oxide scale of the solvent metal. In deriving the kinetic equations under this condition, we begin with the simplest case, viz. binary alloys. Referring to the discussions in §2.3.1 on the previous work of Rhines *et al.* [4.6], Maak [4.7], and Gesmundo and Viani [4.8], it is noted that even the rate law for the internal oxidation of binary alloys below the external scale has not distinctly been expressed.

In the case of a binary alloy A-B, it is assumed that both the internal oxide BO_ν and the outer oxide scale AO grow according to a parabolic rate law. The rate law for the internal oxidation is still taken as the same form as Eq. (4.16), in which ξ is the position of the internal oxidation front measured from the original alloy surface while that for the outer scale growth is given in the form

$$X^2 = 2k_C t \tag{4.42}$$

where X is the thickness of the metal consumed and k_C is the parabolic rate constant. Thus, the effective thickness of the internal oxidation zone is given by $\xi - X$. The general appearance of a cross-section of a oxidized sample is shown in Fig. 4.2 with the definition of the different terms [4.8].

Following Wagner's treatment, Maak [4.7] solved the diffusion equations for oxygen and B in the alloy and obtained the expression for γ, Eq. (2.27), which is rewritten as follows

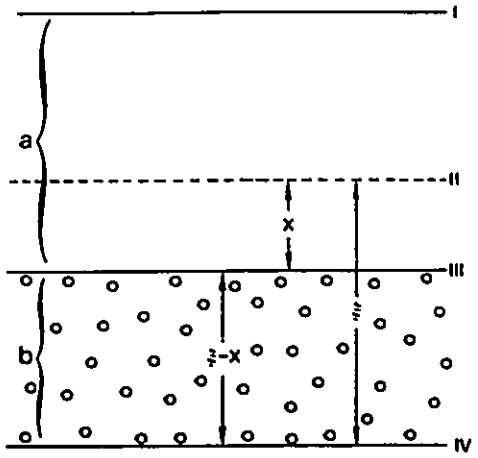

Fig. 4.2 Schmatic illustration of an oxidized sample. *I*, actual scale/gas interface; *II*, original alloy/gas interface; *III*, actual alloy/scale interface; *IV*, internal oxidation front; a, external scale; b, internal oxidation region; *X*, thickness of alloy consumed; ξ, position of the internal oxidation front. [4.8]

$$\frac{N_O^s}{\nu N_B^o} = \frac{\{\mathrm{erf}(\gamma)-\mathrm{erf}[(k_c/2D_O)^{1/2}]\}}{\mathrm{erf}(\gamma)} \frac{G(\gamma)}{F(\gamma\phi^{1/2})} \qquad (4.43)$$

note that N_O^s now equals the oxygen mole fraction at the alloy/scale interface rather than that at the alloy/gas interface. The other parameters as well as the auxiliary functions G and F in Eq. (4.43) are as defined in 2.3.1.

Mathematical asymptotical analysis may also be applied in order to evaluate the parameter γ from Eq. (4.43) for several limiting cases. In this study, we consider the situation when the ratio of growth rate constant of AO to

the diffusion coefficient of oxygen in the alloy, $k_C/2D_O$, is relatively very small (*i.e.*, 10^{-3} – 10^{-4} for Ni-Al alloys [4.9]). Thus two limiting cases exist:

(a) $\gamma \ll 1$, $(k_C/2D_O)^{1/2} \ll 1$, and $\gamma\phi^{1/2} = \gamma(D_O/D_B)^{1/2} \gg 1$.

For this case, besides (4.32), the following asymptotic expansion can be made

$$\mathrm{erf}[(k_C/2D_O)^{1/2}] \approx (2k_C/\pi D_O)^{1/2} \tag{4.44}$$

$$G(\gamma) \approx 2\gamma^2 \tag{4.45}$$

$$F(\gamma\phi^{1/2}) \approx 1 \tag{4.46}$$

Therefore, Eq. (4.43) can be simplified to yield

$$\gamma = \left[\frac{k_C}{8D_O}\right]^{1/2} + \left[\frac{k_C}{8D_O} + \frac{N_O^s}{2\,\nu\,N_B^o}\right]^{1/2} \tag{4.47}$$

It is seen that Eq. (4.47) reduces to Eq. (4.35) when external scale formation is prevented ($k_C = 0$).

(b) $\gamma \ll 1$, $(k_C/2D_O)^{1/2} \ll 1$, but $\gamma\phi^{1/2} = \gamma(D_O/D_B)^{1/2} \ll 1$.

For this case the asymptotical expansions made in (a) are still valid, except that

$$F(\gamma\phi^{1/2}) = F[\gamma(D_O/D_B)^{1/2}] \approx \gamma(\pi D_O/D_B)^{1/2} \tag{4.48}$$

Thus, from Eq. (4.43), one obtains

$$\gamma = \left[\frac{k_c}{2D_O}\right]^{1/2} + \frac{N_O^s \ (\pi D_O)^{1/2}}{2\nu N_B^o \ D_B^{1/2}} \tag{4.49}$$

This can be further reduced to Eq. (4.40) when the external scale formation is prevented ($k_c = 0$).

The treatment in **4.2.1** is followed in order to examine the kinetics of internal oxidation of an A-B-C alloy associated with the formation of an external scale of oxide AO, assuming that the oxidation conditions favor the simultaneous formation of oxides of both solutes B and C. In this case, the expressions for the diffusion of B and C in the alloy will be kept in the same form as Eq. (4.22-28). However, the profile of oxygen concentration in the alloy will take the form [4.7]

$$N_O = N_O^s \frac{\mathrm{erf}(\gamma)-\mathrm{erf}[x/2(D_O t)]^{1/2}}{\mathrm{erf}(\gamma)-\mathrm{erf}[(k_c/2D_O)^{1/2}]} \tag{4.49}$$

The concentration gradient of oxygen at the reaction front $x = \xi$ is then

$$\left.\frac{\partial N_O}{\partial x}\right|_{\xi} = -\frac{N_O^s \exp(-\gamma^2)}{(\pi D_O t)^{1/2} \ \{\mathrm{erf}(\gamma)-\mathrm{erf}[(k_c/2D_O)^{1/2}]\}} \tag{4.50}$$

Substitution of Eq. (4.22), Eq. (4.23) and Eq. (4.50) into Eq. (4.28) yields

$$\frac{D_O^{1/2} \ N_O^s \exp(-\gamma^2)}{\mathrm{erf}(\gamma)-\mathrm{erf}[(k_c/2D_O)^{1/2}]} = \frac{x_y + (1-x)\nu}{(1-x)|\theta|} \sum_{k=1}^{2} \frac{F_k \exp[-\gamma^2(D_O/D_k)]}{D_k^{1/2} \ \mathrm{erfc}[\gamma(D_O/D_k)^{1/2}]} \tag{4.51}$$

where all parameters are as defined before.

Similarly, there exist two limiting cases for the internal oxidation of the ternary alloy below the external scale of AO:

(a) $\gamma \ll 1$, $(k_c/2D_O)^{1/2} \ll 1$, and $\gamma(D_O/D_k)^{1/2} \gg 1$.

Applying asymptotic expansions of Eqs. (4.31-33) and Eq. (4.44), one obtains from Eq. (4.51)

$$\gamma = \left[\frac{k_c}{8D_O}\right]^{1/2} + \left[\frac{k_c}{8D_O} + \frac{N_O^s\,(1-x)\,|\theta|}{2[x_y + (1-x)v]\sum_{k=1}^{2}\frac{F_k}{D_k}}\right]^{1/2} \tag{4.52}$$

(b) $\gamma \ll 1$, $(k_c/2D_O)^{1/2} \ll 1$, but $\gamma(D_O/D_k)^{1/2} \ll 1$.

Substitution of Eqs. (4.31-32), (4.37-38), and (4.44) into Eq. (4.51) yields

$$\gamma = \left[\frac{k_c}{2D_O}\right]^{1/2} + \frac{N_O^s\,(1-x)|\theta|(\pi D_O)^{1/2}}{2[x_y + (1-x)v]\sum_{k=1}^{2}\frac{F_k}{D_k^{1/2}}} \tag{4.53}$$

It is clear that Eq. (4.52) and (4.53) can reduce to Eq. (4.34) and (4.39), respectively, when the external scale formation is prevented ($k_c = 0$).

The above analysis demonstrates that by applying a mathematical asymptotic expansion the parameter γ can be evaluated so that Eq. (4.16) may be used to express the kinetics of internal oxidation of binary or ternary alloys. However, it is important to notice that use of these simplified expressions may involve significant errors when the conditions for their validity do not apply strictly. A perfectly general treatment will require either graphical or numerical solutions

of corresponding equations.

4.4 The Transition from Internal to External Oxidation

4.4.1 A General Treatment for Cases of Binary Alloys

A number of investigators have successfully applied Wagner's criterion for the transition from internal to external oxidation, Eq. (2.32), to some practical binary alloy systems (for instance, Ag-In [4.10], Fe-Si [4.11], Ni-Si [4.12], and Ni-Al [4.13] systems) and showed its applicability for predicting minimum solute concentration in the alloy for the formation of an exclusive external scale. Unfortunately, the implementation of this criterion requires an empirical or experimental knowledge of the critical volume fraction of oxide f_v^* needed for the transition.

Referring to the discussion in §2.3.2, there appear to be essentially two ways to understand the criteria for the transition from internal oxidation to exclusive external scale formation on a binary A-B alloy. On the one hand, it is possible to focus on the initial formation of the external scale of BO_v. As a result of selective oxidation, internal precipitates of the oxide BO_v may form at low concentrations of B. These impermeable particles locally block further reaction between the oxygen atoms and B atoms because inward diffusion of oxygen can occur only though the channels between those precipitated particles. Then further reaction may occur either by the sidewise growth of the existing particles or the nucleation of new particles. If the sidewise growth of the particles is maintained (without nucleation), they would grow together and establish a compact

oxide layer which would prevent further internal oxidation —— *i.e.*, a transition from internal to external oxidation. The critical solute concentration, or the critical internal oxide volume fraction, for this transition may be considered as that necessary to maintain the sidewise growth of the oxide particles previously precipitated (without further nucleation of internal oxide precipitates) or to achieve an oxidation rate which is comparable to the exclusively external oxidation [4.4]. An example of this approach is Wagner's criterion for the transition from internal to external oxidation, Eq. (2.32). On the other hand, one might begin by assuming that an external oxide of BO_v is already formed and is compact and pore free, and then examine the conditions required for the growth and stability of this external scale. The growth and stability of the protective scale requires that the flux of solute to the alloy/scale interface remains large enough to provide sufficient B atoms to be further oxidized for development of BO_v, to prevent the possible internal oxidation of B and to prevent oxides of A from becoming stable. These requirements would also define a critical concentration of B for the exclusively external oxidation. An example of this second approach is the criterion developed by Smeltzer and Whittle for the onset of internal oxidation under an external scale of BO_v, Eq. (3.35). When making a comparison between theoretically predicted and experimentally observed minimum concentrations of B for the formation of the external scale of BO_v, in an ideal case, the above two approaches could arrive at the same prediction. Based on the above understanding, we can unify the two different approaches and give a general treatment of the exclusive external scale formation and the transition from internal to external oxidation. Thus the value of the critical volume fraction of the oxide f_v^* may be theoretically estimated from more basic data involving

thermodynamics, diffusion data and interface reactions.

Let us now reconsider Wagner's criterion for the transition from internal to exclusive external oxidation. Comparing Eq. (2.31) with Eq. (2.24), one finds there is a correlation between the parameter γ and the mole fraction of the oxide BO_v, f, or the volume fraction of the oxide f_v in the internal oxidation zone:

$$G(\gamma) = \frac{N_O^s}{\nu f} = \frac{N_O^s \varphi}{\nu f_v} \tag{4.54}$$

where φ is the ratio of the molar volume of BO_v, V_{ox}, to that of the alloy, V_a. If $\gamma \ll 1$, an asymptotical expansion, Eq. (4.45), can be made for the auxiliary function $G(\gamma)$. Thus

$$\gamma = \left[\frac{N_O^s \varphi}{2\nu f_v}\right]^{1/2} \tag{4.55}$$

This implies that when the volume fraction of the oxide f_v reaches the critical value f_v^*, there also exists a critical value of γ^* and the penetration of the internal oxidation zone will follow a rate law as

$$\xi^2 = 2\gamma^*(D_O t)^{1/2} \tag{4.56}$$

Once the critical volume fraction of the oxide is reached, the penetration rate of the internal oxidation zone may be regarded to be comparable to the growth rate of an "equivalent exclusive external oxide scale". The internal oxidation reaction front may be regarded as an "equivalent interface" to the moving

scale/alloy interface in the case of exclusive external oxidation. Mass balance at this equivalent interface may be also assumed, *i.e.*, the amount of the solute B consumed due to internal oxidation could be related to the number of moles of B arriving at the interface through diffusion from the alloy as well as the interfacial concentration of B, $N^*_{B,i}$, built up at the interface due to the enrichment of B. Therefore, Eq. (2.30) is modified as:

$$\left(\frac{f^*}{V_{OX}}\right) A \frac{d\xi}{dt} = \lim_{\epsilon \to 0} \left[\frac{D_{AB} A}{V_A}\left(\frac{\partial N_B}{\partial x}\right)_{x=\xi+\epsilon}\right] + \frac{N^*_{B,i}}{V_A} A \frac{d\xi}{dt} \qquad (4.57)$$

where the molar concentration of the oxide internal oxidation zone becomes f/V_{OX} instead of f/V_A, because the amount of unoxidized metal is very small in the internal oxidation zone. The concentration gradient at the "equivalent interface" is given as [4.14]

$$\left(\frac{\partial N_B}{\partial x}\right)_{x=\xi} = \frac{N^*_B - N^*_{B,i}}{(\pi D_{AB} t)^{1/2}} \frac{\exp(-k^*/2D_{AB})}{\mathrm{erfc}(k^*/2D_{AB})^{1/2}} \qquad (4.58)$$

where k^* is the critical rate constant when regarding the internal oxidation zone as the "equivalent exclusive external scale", and N^*_B is the critical bulk concentration required for the exclusive external scale formation. If k^*/D_{AB} is assumed to be very small, substitution of Eq. (4.55), (4.56) and (4.58) into Eq. (4.57) will yield

$$\frac{f^*_v - N^*_{B,i}\cdot\varphi^2}{(f^*_v)^{1/2}} = \left(\frac{2\nu D_{AB}\varphi^3}{\pi D_O N^s_O}\right)^{1/2} \cdot (N^*_B - N^*_{B,i}) \qquad (4.59)$$

The critical interfacial concentration $N^*_{B,i}$ is related to N^*_B by the relationship [4.14]

$$N^*_B = N^*_{B,i} + (1 - N^*_{B,i})F(u) \tag{4.60}$$

where the auxiliary function F(u) for $u = (k_C/2D_{AB})^{1/2}$ is as previously defined in Eq. (2.34), k_C can be taken from typical values of the parabolic rate constant for the exclusive external oxidation of the A-B alloys. The value of N^*_B may be estimated using the criterion of Smeltzer and Whittle [4.14], Eq. (2.35).

For the oxidation of Ni-Al alloys at 1373 K, the value of the parabolic rate constant for the exclusive growth of Al_2O_3 scales is approximately 4.6×10^{-12} $g^2/cm^4 \cdot sec$ [4.15], and the value of thermodynamic interaction parameter ε_O^{Al} can be taken from the measurement in a nickel melt as -116 [4.16]. Based on the thermodynamic and diffusion data outlined in Chapter 3 for the Ni-Al-O system, we have used Eq. (2.35) and Eq. (4.60) to obtain values of N^*_{Al} and $N^*_{Al,i}$ as 0.123 and 0.106, respectively. This predicted critical Al bulk concentration required for exclusive external Al_2O_3 scale formation on Ni-Al alloys at 1373 K is consistent with the experimental observation by Pettit [4.15]. Substitution of the values of N^*_{Al} and $N^*_{Al,i}$ into Eq. (4.59) yields a value of the critical Al_2O_3 volume fraction f^*_v of 0.34 for Ni-Al alloys at 1373 K. This value agrees very well with the experimentally observed value by Hindam and Whittle [4.16] for Ni-8at% Al oxidized in air at the same temperature (0.33).

Let us then apply Eq. (4.59) to the well-known value of f^*_v (0.30) obtained by Rapp [4.10] in the oxidation of Ag-In alloys at 823 K at an oxygen pressure of 1 atm. At this temperature and oxygen pressure, $D_O N^s_O = 2.5 \times 10^{-10}$ cm^2/sec, $D_{InAg} =$

2.3×10^{-11} cm^2/sec, $\nu = 1.5$, and $\varphi = V_{ox}/V_A = 1.9$. Rapp [4.10] found that the critical In bulk content for the transition from internal to external oxidation under these oxidizing conditions was 15 at%. When assuming a critical interfacial In concentration of 7.7 at%, we find that f_v^* would be equal to 0.30 using Eq. (4.59). Although there is not enough information (*i.e.*, ε_O^{In} in an Ag matrix) to allow us to verify this value of the critical interfacial In concentration, it demonstrates that exclusive external scale formation and the transition from internal to external oxidation can be treated with a general expression given by Eq. (4.59), and the critical volume fraction of the oxide f_v^* may be theoretically predicted.

4.4.2 A Criterion for the Transition from Internal to External Oxidation of Ternary Alloys

The purpose of this section is to use multicomponent diffusion theory to expand Wagner's analysis for the onset of internal oxidation beneath the external scale when oxidizing conditions favor formation of the oxide of the least noble metal in a ternary alloy.

A simple diffusion model is shown schematically in Fig. 4.3. An external scale of oxide $(BCA)O_\nu$ forms on a dilute A-B-C ternary alloy, and the quaternary oxide is assumed to contain a negligible concentration of the solvent metal A and alloying element C so that its composition corresponds closely to that of the binary oxide BO_ν. For convenience, we designate 1 as oxygen, 2 as the least noble metal B, 3 as the third alloying element C, and 4 as the solvent metal A.

The diffusion of alloying elements A, B and oxygen in the A-B-C alloy is

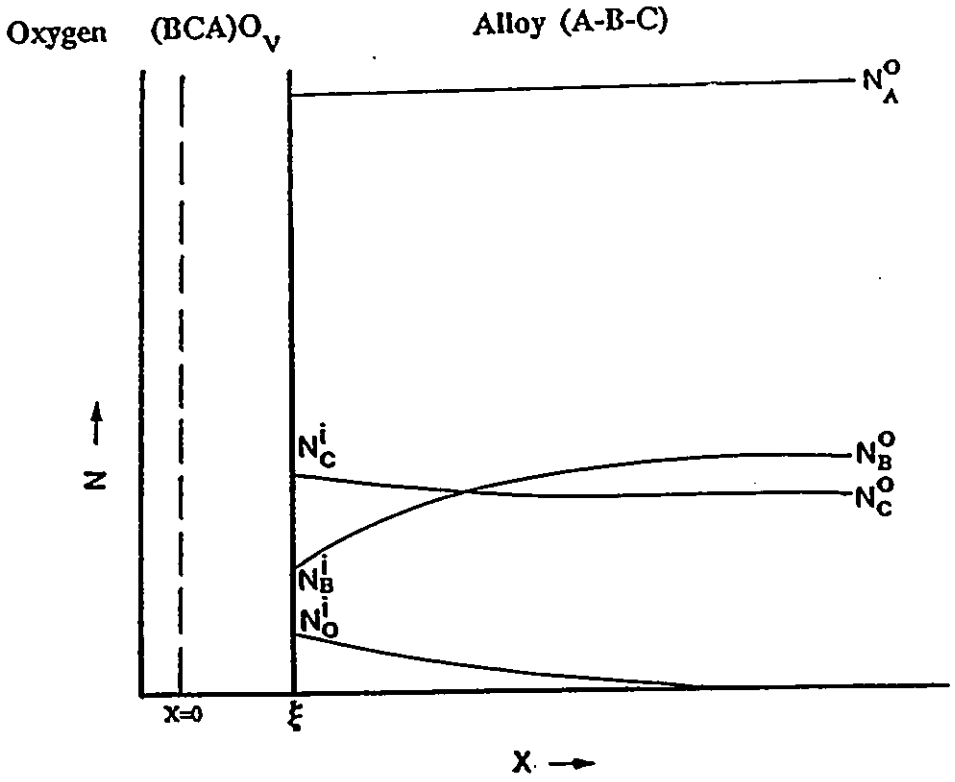

Fig. 4.3 An oxidation model for a dilute A-B-C alloy

determined by Fick's second law in matrix form. Following Toop's method [4.5], the solution of the diffusion equations may be given as

$$N_j = \sum_{k=1}^{3} \theta_{ik} U_k + \sum_{k=1}^{3} \theta_{jk} W_k \operatorname{erf}\left[\frac{x}{2(D_k t)^{1/2}}\right] \qquad j = 1, 2, 3 \tag{4.61}$$

where θ's are the elements of the eigenvector matrix, [θ], of the 3 × 3 diffusivity matrix of the quaternary system [D]. D_k is the eigenvalue of the [D] matrix. U_k and W_k are constants.

The oxide scale of BO_v is assumed to grow by diffusion of either or both oxygen or B in the oxide, so that the scale may thicken according to a parabolic growth law:

$$\xi = (2kt)^{1/2} \tag{4.62}$$

Therefore the concentration gradient of the diffusing species at the scale/alloy interface will be given by differentiation of Eq. (4.61)

$$\left.\frac{\partial N_j}{\partial x}\right|_{\xi} = \frac{1}{(\pi t)^{1/2}} \sum_{k=1}^{3} \theta_{jk} W_k \frac{\exp(-k/2D_k)}{D_k^{1/2}} \qquad j = 1, 2, 3 \tag{4.63}$$

To evaluate the constant W_k in Eq. (4.61) and (4.63), one may consider that the various diffusing species are conserved at the scale/alloy interface, viz., mass balance should be applied. The flux equation of these species towards the interface may have the usual form

$$J_j = -\sum_{k=1}^{3} \frac{D_{jm}}{V_a} \frac{\partial N_m}{\partial x}\bigg|_{\xi} = -\frac{1}{(\pi t)^{1/2}} \sum_{k=1}^{3} \frac{D_{jm}\theta_{mk}W_k \exp(-k/2D_k)}{V_a \quad D_k^{1/2}} j,\ m = 1, 2, 3 \quad (4.64)$$

where V_a is the molar volume of the alloy. This would result in very complicated mathematical calculations. We therefore apply Morral's diffusion analysis (see §2.3.3) here by introducing a square root diffusivity matrix [r], with [r][r] = [D]. At the scale/alloy interface, it yields

$$\frac{1}{V_a}(v - N_1^i)\frac{d\xi}{dt} = \frac{1}{V_a(\pi t)^{1/2}}[-r_{11}N_1^i + r_{12}(N_2^o - N_2^i) + r_{13}(N_3^o - N_3^i)] \quad (4.65)$$

$$\frac{1}{V_a}(1 - N_2^i)\frac{d\xi}{dt} = \frac{1}{V_a(\pi t)^{1/2}}[-r_{21}N_1^i + r_{22}(N_2^o - N_2^i) + r_{23}(N_3^o - N_3^i)] \quad (4.66)$$

where the r terms are the elements of the square root diffusivity matrix, and N_j^o and N_j^i are the bulk and interfacial concentration of species j, respectively.

For the dilute ternary alloy, one may assume that the difference between bulk and interfacial concentrations of the solvent is quite small. Therefore

$$N_3^o - N_3^i = N_1^i - (N_2^o - N_2^i) \quad (4.67)$$

Thus substitution of Eq. (4.62) and (4.67) into Eq. (4.65) and (4.66) yields

$$N_1^i = \frac{[r_{12} - r_{13} + (r_{22} - r_{23})v](\pi k/2)^{1/2}}{(r_{23} - r_{21})(r_{12} - r_{13}) - (r_{13} - r_{11})(r_{22} - r_{23})} \quad (4.68)$$

$$N_2^i = N_2^o - f(r,k) = N_2^o - \frac{[r_{11} - r_{13} - (r_{21} - r_{23})v](\pi k/2)^{1/2}}{(r_{23} - r_{21})(r_{12} - r_{13}) - (r_{13} - r_{11})(r_{22} - r_{23})} \quad (4.69)$$

Then according to Eq. (2.18) and Eq. (2.21), we obtain

$$W_k = \frac{(\theta_{3k}^c - \theta_{1k}^c)N_1^i + (\theta_{3k}^c - \theta_{1k}^c)f(r,k)}{|\theta| \operatorname{erfc}[(k/2D_k)^{1/2}]} \quad (4.70)$$

where $|\theta|$ is the determinant of $[\theta]$, and θ_{1k}^c, θ_{2k}^c and θ_{3k}^c are the cofactors of elements θ_{1k}, θ_{2k} and θ_{3k} respectively.

Let a_2 be the chemical activity of B in the alloy, and a_1 the chemical activity of oxygen in the alloy. In equilibrium with BO_v we have

$$a_2 a_1^v = K^{-1} \quad (4.71)$$

where K is the equilibrium constant for the reaction

$$B\ (alloy) + v\ O\ (alloy) = BO_v \quad (4.72)$$

Consider now the concentration profiles of B and oxygen which are depicted by Fig. 4.3 where the external oxide scale forms and grows without an internal oxidation zone. Eq. (4.71) must be satisfied at the alloy/oxide interface. However, to ensure that no internal oxidation occurs inside the alloy, we must have $a_2 a_1^v < K^{-1}$ as we move into the alloy, which means at the interface [4.17]

$$\left[\frac{\partial \ln a_2 a_1^{\nu}}{\partial x}\right]_{x=\xi} \leq 0 \qquad (4.73)$$

Defining the activity coefficients of all elements according to the Wagner formalism for dilute and real solution behavior of the A-B-C alloy

$$\ln \gamma_j = \ln \gamma_j^0 + \varepsilon_j^1 N_1 + \varepsilon_j^2 N_2 + \varepsilon_j^3 N_3 \qquad j = 1, 2, 3 \qquad (4.74)$$

The criterion is then obtained from Eq.(4.73) and Eq. (4.63) as

$$\sum_{k=1}^{3}\left[\left[\varepsilon_1^2 + \nu\varepsilon_1^1 + \frac{\nu}{N_1^i}\right]\theta_{1k} + \left[\varepsilon_2^3 + \nu\varepsilon_1^3\right]\theta_{3k} + \left[\varepsilon_2^2 + \nu\varepsilon_1^2 + \frac{1}{N_2^i}\right]\theta_{2k}\right]F_k \leq 0 \qquad (4.75)$$

where

$$F_k = \frac{W_k \exp(-k/2D_k)}{(D_k)^{1/2}} \qquad k = 1, 2, 3 \qquad (4.76)$$

Substituting Eq. (4.69) into Eq. (4.75) yields

$$N_2^o \geq f(r,k) - \left\{\sum_{k=1}^{3}\left[\left[\varepsilon_1^2 + \nu\varepsilon_1^1 + \frac{\nu}{N_1^i}\right]\theta_{1k} + \left[\varepsilon_2^2 + \nu\varepsilon_1^2\right]\theta_{2k} + \left[\varepsilon_2^3 + \nu\varepsilon_1^3\right]\theta_{3k}\right]F_k\right\}^{-1}\sum_{k=1}^{3}\theta_{2k}F_k \qquad (4.77)$$

Thus, Eq. (4.77) may be utilized to define the critical bulk concentration of solute B above which no internal oxidation occurs and an exclusively external

BO_ν scale forms on the ternary alloy in terms of diffusivities of the alloying element and oxygen within the alloy, the parabolic rate constant for the external scale growth, and the activity coefficients or interaction parameters of B, C and oxygen.

4.5. Protective Scale Formation and Growth on Ternary Alloys

Wagner [4.18] recognized that a condition for protective scale formation is that the reactive solute must have sufficient mobility to reach the surface before it is internally oxidized by oxygen which has dissolved into the metal from the atmosphere. For the oxidation of binary alloys, this condition may be achieved by having a high bulk concentration of the solute. In the case of ternary alloys, however, it has been noticed that certain third element additions encourage protective scale formation of the oxide of the least noble metal. To quantitatively explain this third element effect, one may use the model developed early in this chapter (§4.2) to examine the effect of alloy composition on the solubility and then diffusion behavior of oxygen in the ternary alloys. It is also important, as suggested by Morral [4.18], to investigate the effect of the third element addition on the diffusion flux of the least noble metal from the alloy to the scale/alloy interface. Such a research effort has already been made by Morral [4.19]. Unfortunately, in Morral's work, he assumed that both alloy solutes were oxidized and their concentrations at the scale/alloy interface were zero. Thus the concentration gradients of the solutes within the alloy were along the same direction. These assumptions do not quite represent the real situation when the exclusive external oxide scale of only one solute is desired.

In this section, we consider a more practical case of the oxidation of a dilute A-B-C ternary alloy. Oxidation conditions favor the scale formation of the oxide of only the least noble metal B, and the scale/alloy interface moves according to a parabolic rate law defined by Eq. (4.62). To simplify the analysis, the flux of oxygen in the alloy is ignored because its effect on solute diffusion will be very small as long as internal oxidation does not occur. By assuming a negligible concentration of B at the scale/alloy interface and also the negligible difference between concentrations of the solvent A in the bulk of the alloy and at the scale/alloy interface, the boundary conditions for diffusion are

$$\begin{aligned} &t = 0, \ N_B = N_B^o, \ N_C = N_C^o && \text{for } x \geq 0 \\ &\text{All } t, \ N_B = N_B^o, \ N_C = N_C^o && \text{for } x = \infty \\ &\qquad N_B = 0, \ \ N_C = N_C^o + N_B^o && \text{for } x = \xi \end{aligned} \tag{4.78}$$

The diffusion of B and C in the ternary alloy can be described by Fick's second law in a form of matrix as Eq. (4.19). The diffusivity matrix [D] given by Eq. (4.21) has its eigenvector matrix [θ] as

$$[\theta] = \begin{bmatrix} \theta_{CC} & \theta_{CB} \\ \theta_{BC} & \theta_{BB} \end{bmatrix} \tag{4.79}$$

The solutions subject to the boundary conditions above will be of the forms

$$N_C = N_C^o - \theta_{CB} W_1 - \theta_{CC} W_2 + \theta_{CB} W_1 \mathrm{erf}(x/2\sqrt{u_1 t}) + \theta_{CC} W_2 \mathrm{erf}(x/2\sqrt{u_2 t}) \tag{4.80}$$

$$N_B = N_B^o - \theta_{BB} W_1 - \theta_{BC} W_2 + \theta_{BB} W_1 \mathrm{erf}(x/2\sqrt{u_1 t}) + \theta_{BC} W_2 \mathrm{erf}(x/2\sqrt{u_2 t}) \tag{4.81}$$

where u_1 and u_2 are the eigenvalues of the diffusivity matrix [D] obtained by solving its characteristic equation, the constants W_1 and W_2 are written as

$$W_1 = N_B^o(\theta_{BB}^C - \theta_{CB}^C)/|\theta| \tag{4.82}$$

$$W_2 = N_C^o(\theta_{BC}^C - \theta_{CC}^C)/|\theta| \tag{4.83}$$

where $|\theta|$ is the determinant of the matrix $[\theta]$, θ_{ij}^C are the cofactors of the relevant elements θ_{ij}. Therefore the flux of B from the bulk of alloy to the scale/alloy interface can be written as

$$J_B = \frac{1}{\sqrt{\pi t}\, V_a}\left[(D_{BB}\theta_{BB} + D_{BC}\theta_{CB})\frac{W_1}{\sqrt{u_1}}\exp\left[\frac{-\xi^2}{4u_1 t}\right] + (D_{BB}\theta_{BC} + D_{BC}\theta_{CC})\frac{W_2}{\sqrt{u_2}}\exp\left[\frac{-\xi^2}{4u_2 t}\right]\right] \tag{4.84}$$

In general, for the case of exclusive external oxidation, $\xi^2/4u_1 t$ and $\xi^2/4u_1 t \ll 1$. Eq. (4.84) may become

$$J_B = \frac{1}{\sqrt{\pi t}\, V_a}\left[(D_{BB}\theta_{BB} + D_{BC}\theta_{CB})\frac{W_1}{\sqrt{u_1}} + (D_{BB}\theta_{BC} + D_{BC}\theta_{CC})\frac{W_2}{\sqrt{u_2}}\right] \tag{4.85}$$

For the particular case when oxygen diffusion is the predominant diffusion process within the oxide BO_ν and the extent of its nonstoichiometry is very small, one may write the expression of oxygen flux through the oxide as

$$J_O = - D_O \frac{\Delta N_O}{V_{ox} X} = - D_O \frac{V_a \Delta N_O}{(V_{ox})^2 \xi} = \frac{V_a}{2(V_{ox})^2 \xi} \int_{p^i_{O_2}}^{p^s_{O_2}} D_O \, d \ln p_{O_2} \qquad (4.86)$$

where D_O is the effective oxygen diffusion coefficient in the oxide BO_ν, V_{ox} is the molar volume of BO_ν, X is the thickness of the oxide scale, ΔN_O is oxygen concentration difference across the scale, and $p^s_{O_2}$ and $p^s_{O_2}$ are the oxygen partial pressures at the scale surface and at the scale/alloy interface, respectively. One may also equate the stoichiometric flux of oxygen from the scale and that of B from the alloy at the scale/alloy interface. Therefore,

$$\xi = \left[\frac{V_a^2 \pi^{1/2}}{2\nu (V_{ox})^2 f(D_{ij}, W_i)} \int_{p^i_{O_2}}^{p^s_{O_2}} D_O \, d \ln p_{O_2} \right] t^{1/2} \qquad (4.87)$$

where

$$f(D_{ij}, W_i) = \left[(D_{BB}\theta_{BB} + D_{BC}\theta_{CB}) \frac{W_1}{\sqrt{u_1}} + (D_{BB}\theta_{BC} + D_{BC}\theta_{CC}) \frac{W_2}{\sqrt{u_2}} \right] \qquad (4.88)$$

Eq. (4.88) shows that a beneficial third element effect occurs if alloy additions increase the value of $f(D_{ij}, W_i)$, which in turn will enhance the flux of the solute B from the alloy to the scale/alloy interface and decrease the oxidation rate.

CHAPTER 5

Experimental Methods and Analytical Techniques

5.1 Introduction

The experimental component of this thesis includes a study of the oxidation properties of Fe-Si-Al and Ni-Si-Al alloys. A variety of experimental techniques were used for the preparation and analysis of materials and the oxidation of alloy specimens. For characterization of oxidation products, the major analytical methods used were scanning electron microscopy, transmission electron microscopy, Auger sputter profiling, x-ray diffraction, and optical microscopy. Detailed descriptions of the experimental methods and techniques are given below.

5.2 Sample Preparation and Analysis

Alloys were made with 99.99% electrolytic iron chips from Advent Laboratories Inc., 99.999% nickel from Johnson Matthey, 99.999% aluminum from A.D. Mackey, and semiconductor grade single crystal silicon. The assay for the iron, nickel and aluminum is given in Table 5.1. The metal pieces were ultrasonically cleaned and rinsed in acetone and carefully weighed to produce alloys of nominal compositions as listed in Table 5.2. The alloys were cast in an arc melter with a

water-cooled hearth. The weight of each batch was about 40 g. The chamber was evacuated to less than 1 torr, purged with prepurified argon for 5 seconds and backfilled with 300 torr of argon. This procedure was repeated before each melting and casting step. The metals were melted together to form a button which was inverted and re-melted at least three times to produce a homogeneous alloy. The button was then cast in the form of an ingot approximately 60 mm long and 10 mm in diameter. The ingots were encapsulated in quartz tubes under high vacuum with an alumina lining to prevent silicon contamination and further annealed for 72 hours at 1373 K. The annealed ingots were machined into rods of 9 mm diameter, encapsulated in quartz tubes under high vacuum, and reannealed for 72 hours at 1373 K. The composition of the ingots was checked by wet chemical analysis, and sample homogeneity was checked by EDAX. The analysed alloy compositions are listed in Table 5.2.

To prepare samples from the ingots, disks approximately 1 mm thick were cut with the Microtech Precision Wafering Machine using a SiC blade and kerosene as a lubricant. The disks were ground successively on 220, 320, 400, and 600 grit SiC paper with water as a lubricant. The samples were stored in a desiccator until required. Just prior to being oxidized, a final polishing of the samples was done with 6 μm and 1 μm diamond paste impregnated on cloths using kerosene as a lubricant. The thickness and diameter of the polished samples was measured using a micrometer. The samples were ultrasonically washed in soap and water, rinsed in ethyl alcohol, and finally weighed on a Mettler Microgramattic Balance.

5.3 Oxidation Procedure

Oxidation experiments of Fe-Si-Al alloys were carried out at 1073 K in 760

Table 5.1 Chemical analysis of iron, aluminum and nickel in ppm

Impurity	Iron	Aluminum	Nickel
C	<70	-	-
Mn	<60	-	-
P	<30	-	-
S	<80	-	-
Si	<80	-	1
Cu	<30	<1	1
Cr	<50	-	-
V	<6	-	-
Mo	<20	-	-
Ti	<6	-	-
Mg	<10	10	<1
Ca	<10	-	<1
Al	<7	By difference	<1
Fe	By difference	2	1
Ni	<130	<1	By difference

Table 5.2 Nominal and exact alloy compositions

Nominal	Exact
Fe-6 at% Al	Fe-6.16 at% Al
Fe-6 at% Si	Fe-5.87 at% Si
Fe-6 at% Si-1 at% Al	Fe-5.91 at% Si-0.88 at% Al
Fe-6 at% Si-3 at% Al	Fe-5.86 at% Si-2.85 at% Al
Fe-6 at% Si-5 at% Al	Fe-5.94 at% Si-4.93 at% Al
Ni-1 at% Si-4 at% Al	Ni-0.95 at% Si-3.79 at% Al

or 0.04 to 0.07 torr of dry oxygen. Two grades of oxygen, supplied by Canadian Liquid Air and Matheson Gas, were used: Ultra High Purity and Research Purity. The assay for the two gases is given in Table 5.3 and 5.4. A Research Purity grade mixture of 4% natural oxygen (^{16}O) and 96% ^{18}O, supplied by Icon Services Inc., was also used.

The experimental setup schematically shown in Fig. 5.1 was used to measure oxidation kinetics manometrically. It consists of an oxygen supply, a quartz reaction tube, an infrared heating furnace and a vacuum system. The sample was spot-welded on a Pt – Pt13wt%Rh thermocouple and was then inserted into the center of the reaction tube. The whole system was evacuated to less than 4×10^{-9} torr and then the reaction tube and chamber were filled with 0.9 torr of Research Purity oxygen for 1.5 hours in order to saturate the system wall. After saturation, the pressure was reduced to approximately 0.04-0.07 torr and the sample was heated to 1073 K within about 1.5 minutes. The temperature was controlled to ± 0.5 K. The lamp reflector bodies of the heating furnace and the quartz tube ends were water-cooled. The exterior of the tube was cooled by forced air flow. Gas pressure inside the tube was measured to a precision of ± 0.1% with an MKS Baritron temperature compensated differential capacitance gauge. The gauge was zeroed with respect to a reference vacuum kept at less than 10^{-8} torr. Output from the gauge was simultaneously recorded on a computer and the oxygen pressure drop due to oxidation was converted into oxygen uptake per unit area of the sample surface. The pressure within the system was maintained within the desired range by periodically dosing with oxygen through a gas leak valve.

Oxidation of the Ni-Si-Al alloys was carried out at the dissociation pressure of NiO and in 760 torr of oxygen at 1073 K, respectively. The oxygen

Table 5.3 Assay of ultra high purity oxygen

N_2	<50 ppm
Ar	<30 ppm
H_2, H_2O	<5 ppm
CH_4	<2 ppm
CO, CO_2	<0.5 ppm

Table 5.4 Assay of research purity oxygen

N_2	<5 ppm
Ar	<5 ppm
H_2, H_2O	<1 ppm
CH_4	<0.1 ppm
CO, CO_2	<0.1 ppm
He	<1 ppm
Xe	<1 ppm
Kr	<1 ppm

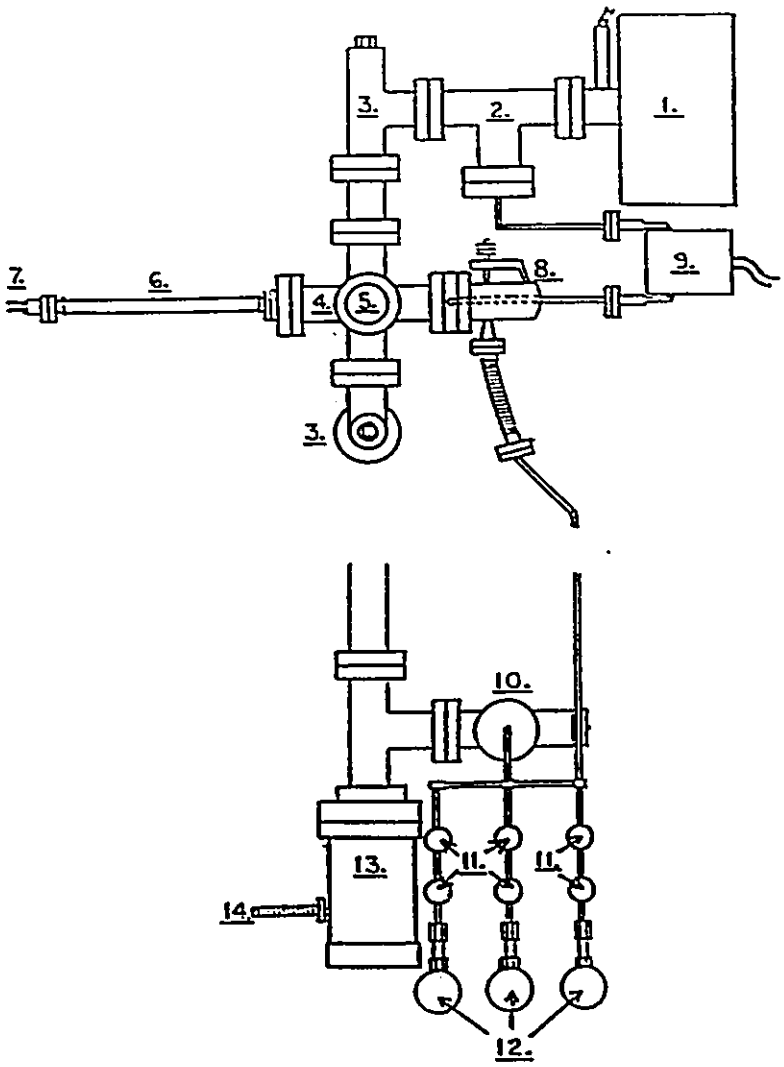

Fig. 5.1 Schematic of manometric oxidation assembly: 1 – 20 l/s ion pump, 2 – reference vacumm chamber, 3 – all metal valve, 4 – 6 way flange, 5. – ionization gauge head, 6 – reaction tube, 7 – thermocouple feedthrough, 8 – UHV gas dosing valve, 9 – temperature compensated capacitance gauge, 10 – Viton valve, 11 – packless valves, 12 – gas cylinders, 13 – 50 l/s turbomolecular pump, 14 – flexible bellows to a rotary pump

activity was maintained at the dissociation pressure of NiO by a mixture of Ni and NiO powders. The amount of NiO powder used in the NiO+Ni mixture was enough to oxidize the two alloying elements (Al and Si) in the samples. The mixture of powders was pressed to get a porous compact pellet. The polished samples, suspended in open-ended α-alumina tubes by Pt wires, and the Ni/NiO pellet were encased in an evacuated quartz tube, which was then put into a horizontal furnace for periods of 8, 20, 48, 120 and 500 hours. For the oxidation in 760 torr of oxygen at 1073 K, the polished samples were put onto alumina crucibles and then were placed into the horizonal furnace with a flow of dry oxygen of 760 torr.

5.4 Analytical Techniques

5.4.1 Optical Metallography

The oxidized samples were mounted vertically and vacuum impregnated with cold setting epoxy resin. They were polished in cross-section on SiC papers of 220, 320, 400, and 600 grit using water as a lubricant. Final polishing was done on cloths impregnated with 6 μm and 1 μm diamond paste using kerosene as a lubricant. Microstructure of the samples was viewed in a Zeiss optical microscope. Samples of unoxidized alloys were etched by dilute nitric acid. The average grain size for these samples was found to be 1.0±0.3 mm. Thicknesses of external and internal oxide layers of the Ni-Si-Al alloys were measured by a computer-controlled image analyzer attached to the optical microscope. More than 30 data points were collected from each sample and average thickness values and standard deviations were obtained.

5.4.2 Scanning Electron Microscopy

Two scanning electron microscopes (Philips 505B and Philips 515) were used in this investigation. Oxidized samples were mounted on aluminum studs using a silver dag and were gold coated to minimize surface charging.

Photomicrographs of surfaces and cross-sections of the oxidized sample were taken on type 52 Polaroid film using secondary electron images. The cross-sections were prepared by polishing.

The X-ray Energy Dispersive Analysis (EDAX) attachments to the two SEM models were used to analyze the oxide composition. In cases where small features were analyzed, the interaction volume may have been larger than the feature of interest so that areas of different composition were included in the analysis. In particular, for thin oxide layers the analysis may include compositional information from the alloy matrix. X-ray data were collected in numerical form. As a practical limit of resolution, the electron interaction volume was estimated to be no less than 1 μm^3.

5.4.3 X-ray Diffraction

X-ray diffraction analysis of the oxidation product was carried out using a Philips x-ray diffractometer and a Debye-Scherrer camera. Either the whole sample was analyzed or the oxide was removed from the sample and crushed into a powder. In either case the sample was attached to a glass holder for analysis. A voltage of 30 kV and 20 mA (Cu K_α radiation) was used throughout this investigation. Data was acquired in graph form with x-ray peaks drawn at

characteristic angles. The experimental results were then compared with those recorded in JCPDS tables.

5.4.4 Scanning Auger Microscopy

The compositions of oxide phases and depth profiles through the oxide were determined using a PHI Model 600 scanning Auger microscope. An argon beam was used to sputter away the sample, which was tilted at 45 degrees. Depth profiles were obtained at a magnification of 5000× by alternate sputtering and data collection. The oxide/alloy interfaces may not be shown accurately in the depth profiles as sputtering tends to cause profile broadening. This is due to a number of factors which include preferential sputtering, sputter-induced surface roughness and ion mixing [5.1]. Some operating parameters used in this investigation are listed in Table 5.5.

Table 5.5 SAM operating parameters

	Electron Beam	Auger Ion Beam
Voltage (keV)	5	4
Current (μA)	0.5	2
Beam diameter (μm)	0.1	200
Pressure (Pa)	2.0×10^{-8}	2.7
Raster size (μm×μm)	40×40	2000×2000

5.4.5 Transmission Electron Microscopy

A Philips CM 12 transmission electron microscope was used in this investigation. Oxide film specimens required were stripped from the alloy surface by direct chemical attack of the underlying alloy with a methanol 10% bromine solution. Before stripping a sample, the oxide on all of the edges was ground off with SiC paper, and the flat surfaces scored with a scalpel into 3 mm squares. The oxide film specimens were washed several times in methanol following stripping in order to remove all trace of bromine. They were then stored in methanol, and finally floated onto copper grids prior to being observed.

Bright field electron microscope techniques was employed along with selected area electron diffraction (SAD). SAD patterns were interpreted using the relation $R = L\lambda/d$, where R is the distance between the transmitted spot and the diffracted spot on the photographic plate, L is the distance between the sample and the photographic plate which is known as the camera length, λ is the wavelength of the incident electrons which depends on the accelerating voltage of the microscope, and d is the spacing of the diffracting planes in the sample. The camera length of the microscope was calibrated against a gold standard and is known within $\pm$ 1%. Values of experimentally observed atomic spacings were compared to ASTM tables for inorganic compounds in order to identify oxide phases.

5.4.6 Secondary Ion Mass Spectrometry

Some oxidized samples were sent to the Institute for Microstructural Sciences (NRC, Ottawa) and to the University of Toronto, and were examined using a

Perkin-Elmer 590 scanning Auger microprobe with a SIMS-II attachment or a Leybold SSM 200 secondary ion mass spectrometry (SIMS), respectively.

To prepare samples for SIMS depth profiling, oxidation was carried out at 1073 K in the manometric apparatus at a pressure of ~0.05 torr. Samples were oxidized first in natural oxygen (^{16}O) and then in oxygen enriched with 95% ^{18}O.

CHAPTER 6

Experimental Results

6.1 Introduction

The oxidation behavior of binary and ternary Fe-Si-Al alloys containing 0-6 at% Si and 0-6 at% Al was investigated at 1073 K in 0.04-0.07 and/or 760 torr of dry oxygen. In this chapter, results on the oxidation kinetics of these alloys are presented first, and then observations of oxide morphology, composition and structure are categorized for each alloy composition examined.

Oxidations of Ni-Si-Al alloys containing 1 at% Si and 4 at% Al were carried out at 1073 K in oxygen at the dissociation pressure of NiO and at the pressure of 760 torr. Results on the oxidation kinetics are reported in this chapter. More detailed results on oxide morphology and structure are given in a paper written by H.C. Yi and the author [6.1].

6.2 Fe-Si-Al Alloys

6.2.1 Oxidation Kinetics

Typical oxidation kinetics were obtained for Fe-6Al, Fe-6Si, Fe-6Si-1Al,

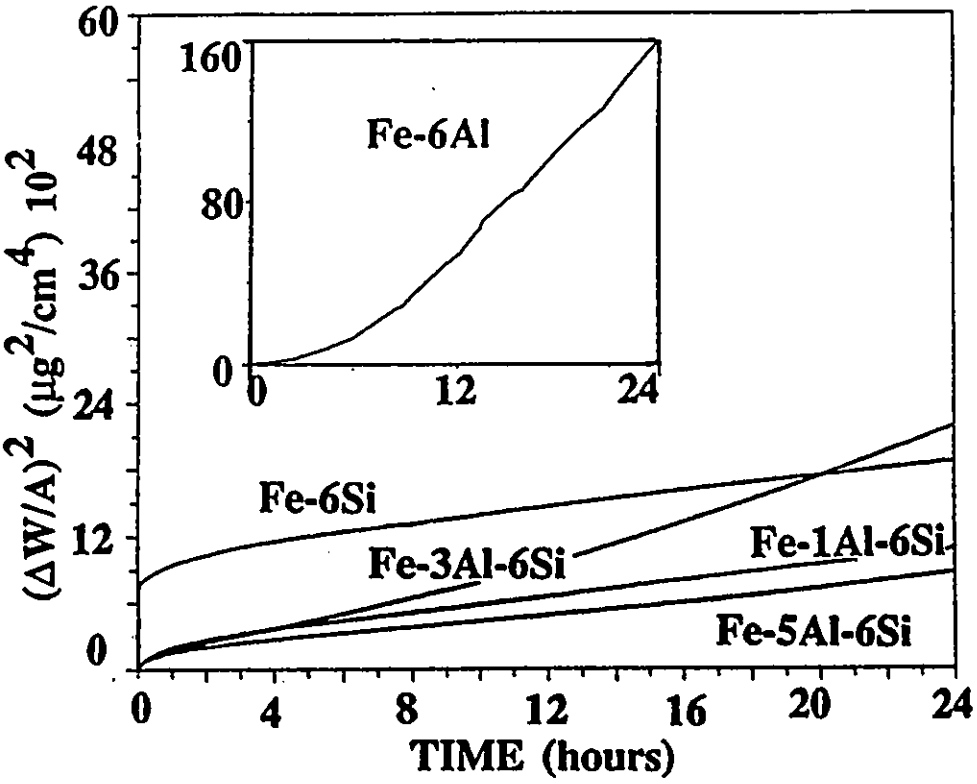

Fig. 6.1 Oxidation kinetics of the Fe-Si-Al alloys in 0.04-0.07 torr of oxygen at 1073 K

Fe-6Si-3Al, and Fe-6Si-5Al alloys oxidized at 1073 K in 0.04-0.07 torr of dry oxygen, as shown in Fig. 6.1. The oxidation rate data are displayed in parabolic coordinates, in order to indicate the relative protectiveness of the scales formed on the various alloys. The order of increasing oxidation resistance based on overall weight gains for oxidation times up to 24 hours was: Fe-6Al « Fe-6Si-3Al < Fe-6Si < Fe-6Si-1Al < Fe-6Si-5Al. The Fe-6Al alloy showed a very large oxidation rate with increasing time. The initial rapid oxidation rate of the Fe-6Si alloy was followed by a very much slower oxidation weight gain. In contrast, after a very brief period of logarithmic kinetics, parabolic kinetics were followed for the Fe-6Si-1Al alloy, with no rapid initial oxidation rate being observed. After a period of two hours, the initial oxidation rate was seen to increase slightly. At the early stage of oxidation, the Fe-6Si-3Al alloy exhibited similar kinetics to those of the Fe-6Si-1Al alloy, but with a slightly lower oxidation rate. After six hours, however, the oxidation rate of the Fe-6Si-3Al alloy accelerated and breakway kinetics were observed. With the same oxidation kinetics as the Fe-6Si-1Al alloy but a lower rate, the Fe-6Si-5Al was the most oxidation resistant alloy.

The weight gains of these binary and ternary Fe-Si-Al alloys after 200 and 500 hours in flowing dry oxygen of 760 torr at 1073 K are given in Table 6.1. The ternary alloys had much smaller values of weight gain than the binary Fe-6Al and Fe-6Si alloys. Unlike the oxidation in 0.04-0.07 torr of oxygen, the overall weight gains of the Fe-6Si-3Al alloy are lower than those of the Fe-6Si-1Al alloy, indicating a trend to better oxidation resistance with increasing Al bulk concentration. This apparent discrepency will be explained in chapter 7.

Table 6.1 Oxidation of Fe-Si-Al alloys in 760 torr of oxygen at 1073 K

Alloys	Weight gain, g/cm^2	
	200 hours	500 hours
Fe-6Al	$7.34\pm0.30\times10^{-3}$	$1.27\pm0.11\times10^{-2}$
Fe-6Si	$1.53\pm0.09\times10^{-3}$	$2.51\pm0.12\times10^{-3}$
Fe-6Si-1Al	$3.04\pm0.18\times10^{-4}$	$4.50\pm0.20\times10^{-4}$
Fe-6Si-3Al	$9.35\pm0.35\times10^{-5}$	$2.09\pm0.17\times10^{-4}$
Fe-6Si-5Al	$5.46\pm0.23\times10^{-5}$	$1.57\pm0.06\times10^{-4}$

6.2.2 Oxide Morphology, Composition and Structure

6.2.2.1 Fe-6Al

Oxidation of the Fe-6Al alloys in 0.04-0.07 torr of oxygen for 24 hours resulted in the formation of a greyish nonprotective oxide, mixing with bulky iron oxide nodules. Lateral growth of the nodules resulted in their overlap and the formation of a continuous scale. As illustrated in Fig. 6.2 (a) and (b), the oxide was made up of at least three distinct layers. Similar oxide morphology was observed for samples oxidized in 760 torr of oxygen up to 200 and 500 hours. In these cases, however, the external oxide scale spalled during cooling, as shown in Fig. 6.2 (c).

Compositional information obtained from EDAX analyses on various morphological features is summarized in Table 6.2. The EDAX results are normalized by dividing the K_{α_1} energy peak of Al by the K_{α_1} energy peak of Fe, which allows qualitative comparisons to be made. Because of the spalling of the external scale during cooling, it was also possible to perform x-ray powder diffraction analysis

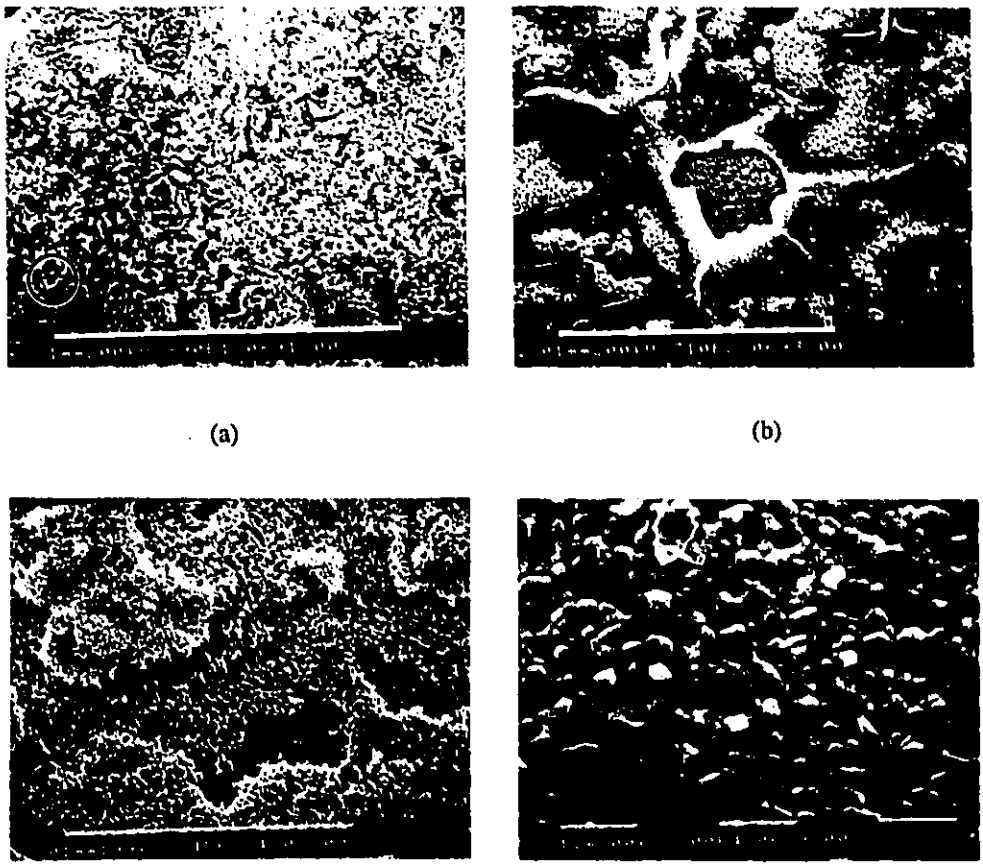

Fig. 6.2 SEM observations of the oxide morphology formed on Fe-6Al alloys.
(a) Sample surface after 24 hours of oxidation in 0.04-0.07 torr of O_2.
(b) Magnified image of the cycle shown in (a).
(c) After 200 hours of oxidation in 760 torr of O_2.
(d) Magnified image of the inner layer in (c).

on the oxides. The results indicated that the oxide scales were composed of outer Fe_2O_3, Fe_3O_4 in the middle and $FeAl_2O_4/Al_2O_3$ next to the metal. After 500 hours of oxidation, the scales contained only layers of Fe_2O_3 and Al_2O_3.

Table 6.2 EDAX compositional analysis

Area of analysis	Al counts ($K_{\alpha_1}Al/K_{\alpha_1}Fe$)
Outer surface Fig. 6.2 (a)	0.021
Smooth oxide surface Fig. 6.2 (b)	0.110
Inner layer Fig. 6.2 (b)	2.231
Outer layer Fig. 6.2 (c)	0.048
Middle layer Fig. 6.2 (c)	0.230
Inner layer Fig. 6.2 (d)	2.629

6.2.2.2 Fe-6Si

The Fe-6Si alloys ultimately formed continuous oxide scales in both 0.04-0.07 and 760 torr of dry oxygen at 1073 K, as shown in Fig. 6.3 (a) and (c). After 500 hours of oxidation in 760 torr of oxygen, however, Fig. 6.3 (d) shows the formation of oxide nodules near specimen edges and corners. The alloy surfaces were greyish in colour after 200 hours of oxidation, becoming reddish after 500 hours of oxidation. The oxide formed on the alloys did not remain adherent on cooling from 1073 K, but exhibited some degree of spallation.

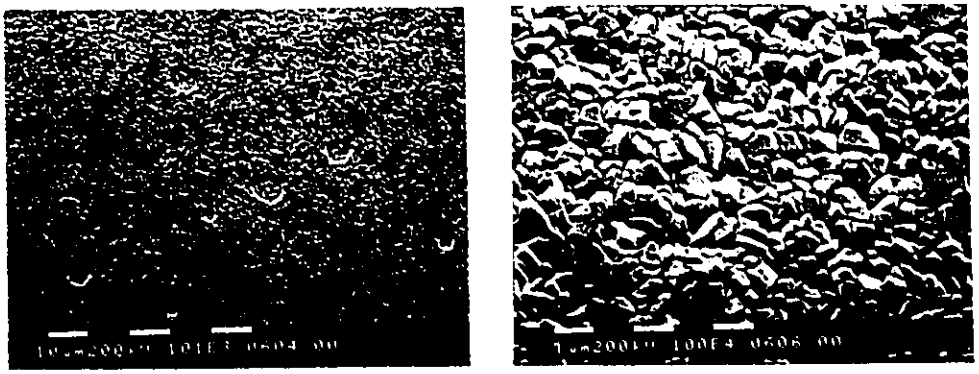

(a) (b)

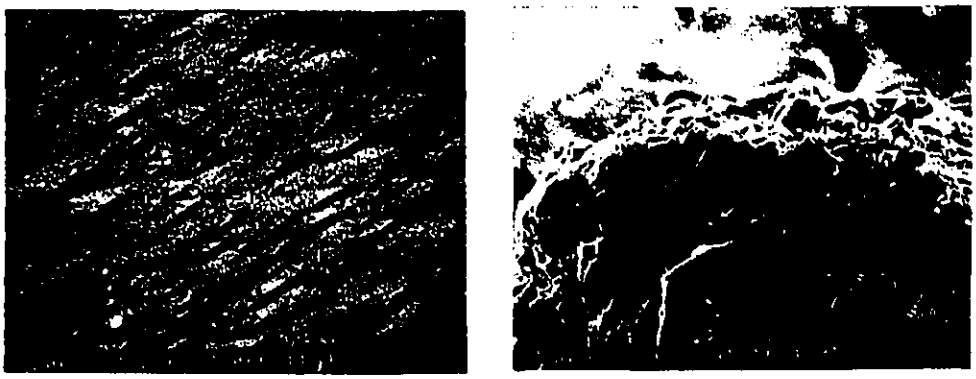

(c) (d)

Fig. 6.3 SEM observations of the oxide morphology formed on Fe-6Si alloys.

(a) Sample surface after 24 hours of oxidation in 0.04-0.07 torr of O_2.

(b) Magnified image of (a).

(c) After 500 hours of oxidation in 760 torr of O_2.

(d) Oxide nodule formed at the specimen eadge after 500 hours of oxidation in 760 torr of O_2.

Table 6.3 EDAX compositional analysis

Area of analysis	Si counts ($K_{\alpha 1}Si/K_{\alpha 1}Fe$)
Smooth surface Fig. 6.3 (a)	0.068
Oxide pit Fig. 6.3 (a)	0.065
Outer oxide layer Fig. 6.3 (c)	0.071
Outer oxide layer Fig. 6.3 (d)	0.021
Second outer layer Fig. 6.3 (d)	0.120
Middle oxide layer Fig. 6.3 (d)	0.882
Inner oxide layer Fig. 6.3 (d)	1.936
Alloy substrata Fig. 6.3 (d)	0.046

Table 6.3. The results indicate that the oxide nodules have a multilayer structure. The outer surface of the nodular oxide is Fe rich, becoming richer in Si with increasing depth. Eventually, a silicon oxide healing layer is formed at the base of the nodule. The oxide nodules formed on the alloys were scraped off the samples and ground to a fine powder. X-ray diffraction analysis of the powder indicated that the nodular oxide comprised of an outer Fe_2O_3 + Fe_3O_4 layer overlying a middle Fe_2SiO_4 layer and an inner SiO_2 layer next to the metal.

The results in Table 6.3 also indicate that the outer surface of the continuous oxide is Fe rich. Auger survey analysis was performed on the oxide formed after 24 hours of oxidation in 0.04-0.07 torr of oxygen at 1073 K. As shown

in Fig. 6.4, the result confirms that the protective oxide has a layer of essentially pure iron oxide at the surface, with no Si signal being detected. The oxide phases were further examined by TEM. A bright field image and associated selected area diffraction pattern (SAD) are shown in Fig. 6.5, for a sample oxidized 30 minutes in 0.04-0.07 torr of oxygen at 1073 K. SAD results indicate the presence of α-Fe_2O_3 and β cristobalite (SiO_2). These two oxide phases were also found in the specimen after 200 hours of oxidation in 760 torr of oxygen by x-ray diffraction analysis, as shown in Fig. 6.6. The above results suggest that the oxide is duplex in nature, with an outer Fe_2O_3 layer and an inner SiO_2 layer.

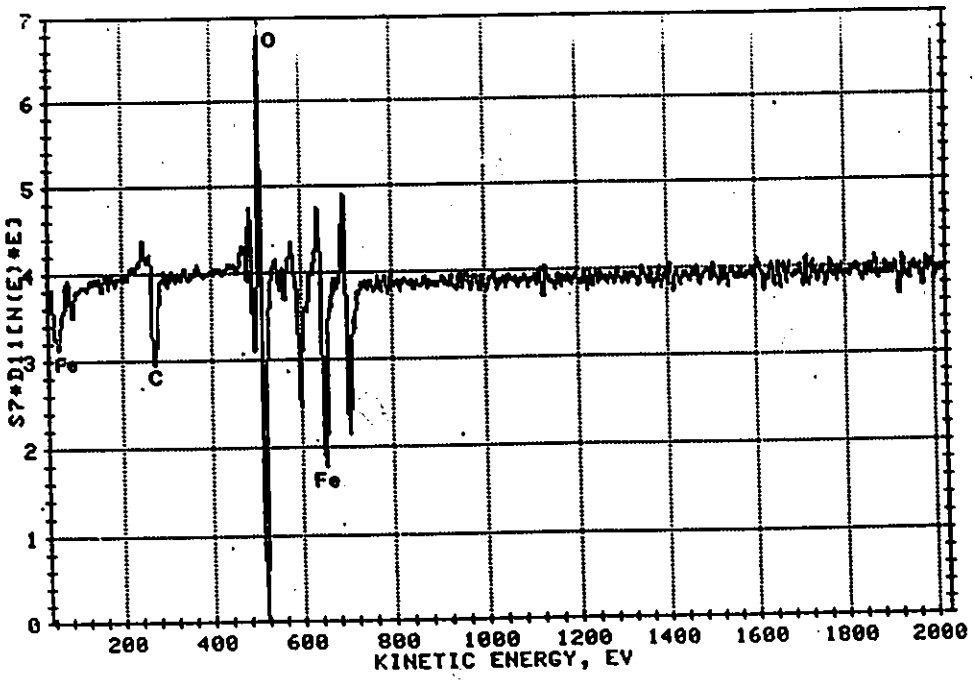

Fig. 6.4 Auger survey analysis of the sample surface after 24 hours of oxidation in 0.04-0.07 torr of O_2 at 1073 K

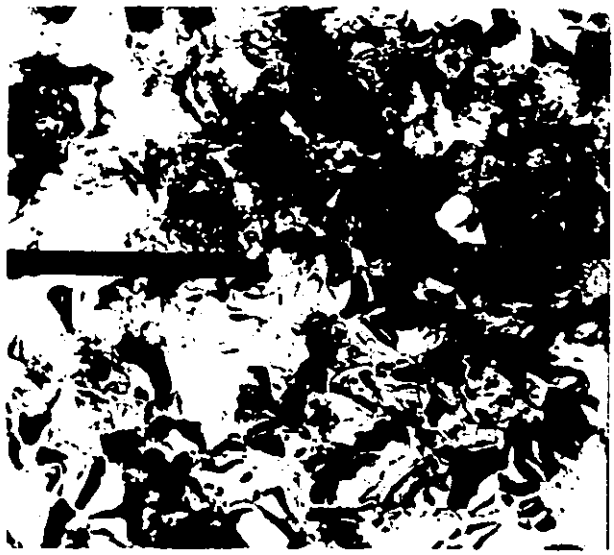

(a) 75000×

(b)

Fig. 6.5 A TEM bright field image and associated SAD pattern for the Fe-6Si alloy oxidized 30 minutes in 0.04-0.07 torr of O_2 at 1073 K. The SAD pattern indicates the presence of α-Fe_2O_3 and β cristobalite.

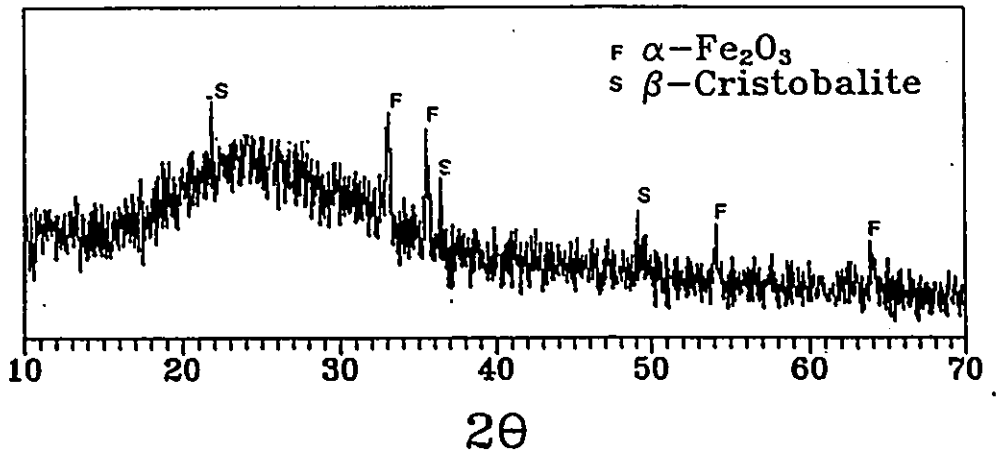

Fig. 6.6 X-ray analysis of the scale formed on the Fe-6Si alloy after 200 hours of oxidation in 760 torr of O_2 at 1073 K

6.2.2.3 Fe-6Si-1Al

As seen in Fig. 6.7 (a) and (b), alloys of this composition formed an adherent continuous oxide after 24 hours of oxidation in 0.04-0.07 torr of oxygen at 1073 K. The protective oxide had a convoluted morphology, with oxide ridges apparently following alloy grain boundaries. The oxide grains were very small with most less than 0.25 μm in diameter. Only one oxide nodule was found on the oxide surface, which is shown in Fig. 6.7 (c) and (d). Qualitative compositional information obtained from EDAX analyses is summarized in Table 6.4. The results indicated that the oxide ridges were Al rich, with no measurable Si present. The nodular oxide had a thin layer of iron oxide at the surface, and significant Al enrichment increasing with depth into the nodule.

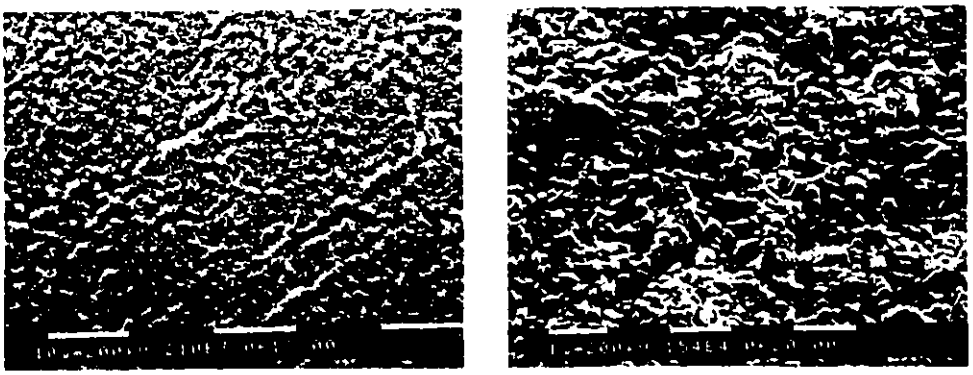

(a) (b)

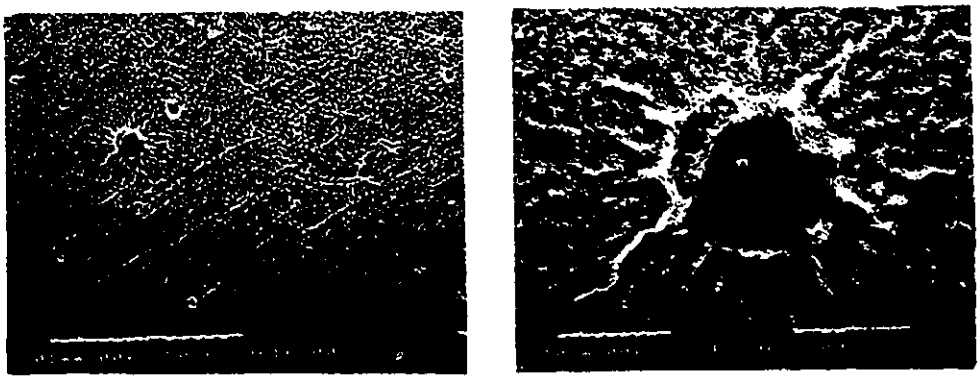

(c) (d)

Fig. 6.7 SEM observations of the oxide morphology formed on Fe-6Si-1Al alloys after 24 hours oxidation in 0.04-0.07 torr of O_2 at 1073 K.

(a) Protective oxide, interspersed with Al rich particles.

(b) Magnified image of (a).

(c) An oxide nodule formed on the sample surface.

(d) Magnified image of (c).

Table 6.4 EDAX compositional analysis

Area of analysis	Al counts ($K_{\alpha 1}Al/K_{\alpha 1}Fe$)	Si counts ($K_{\alpha 1}Si/K_{\alpha 1}Fe$)
Protective oxide Fig. 6.6 (a)	0.183	0.045
Oxide ridges Fig. 6.6 (a)	1.918	–
Oxide particles Fig. 6.6 (a)	5.647	–
Oxide grains Fig. 6.6 (b)	1.256	0.040
Protective oxide Fig. 6.6 (c)	0.280	0.011
Oxide ridges Fig. 6.6 (d)	3.840	–
Oxide nodule (center) Fig. 6.6 (d)	1.256	0.021
Oxide nodule (edge) Fig. 6.6 (d)	5.468	0.001

The oxides formed in 0.04-0.07 torr of oxygen were examined by Auger electron spectroscopy. Fig. 6.8 gives results obtained for the oxide formed after 5 minutes of oxidation. Surveys of the oxide surface before sputtering indicated that oxides of Fe, Al and Si were present. The profile of Fig. 6.8 shows Fe enrichment near the oxide surface, with Al enrichment increasing with depth into the oxide/alloy interface. For the oxide formed after 24 hours of oxidation, some enrichment of Fe was observed at the oxide surface, while Si was not detected in the oxide by Auger survey analysis as shown in Fig. 6.9 (a). The Fe oxide was likely present as segments rather than a continuous outer layer at the sample surface, since strong Al peaks were also found there. After ion sputtering for 30 minutes, very weak Fe peaks are seen from Fig. 6.9 (b), indicating the oxide was

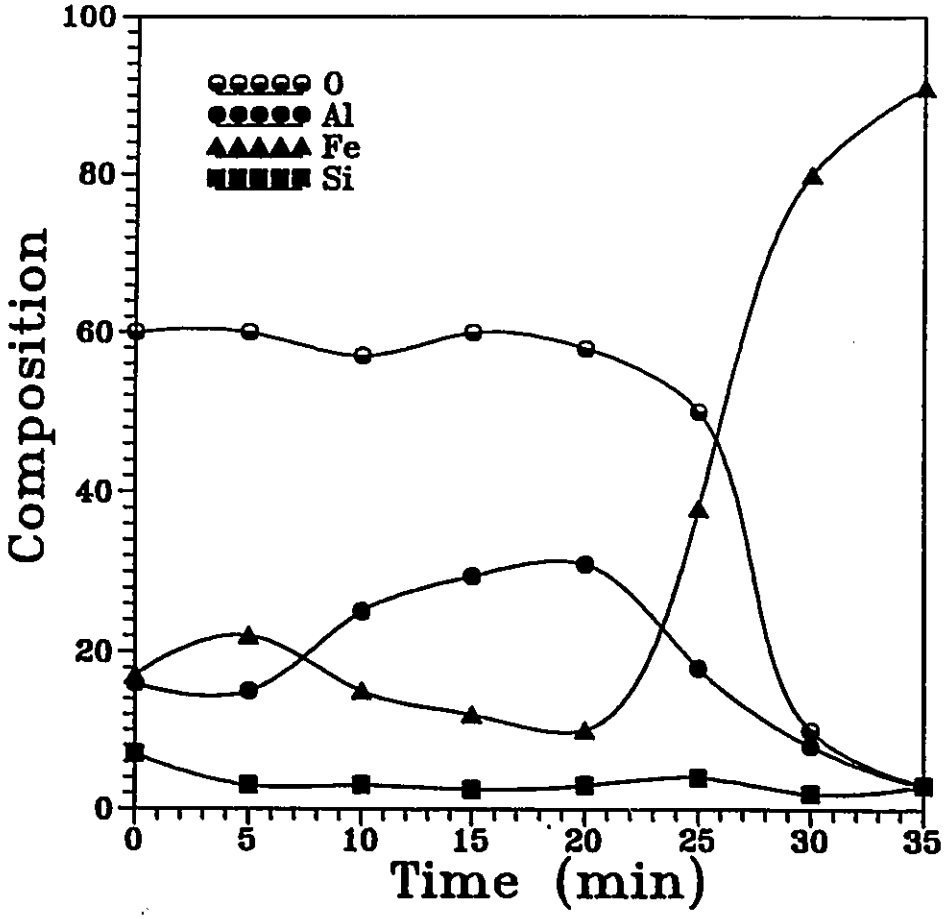

Fig. 6.8 Auger depth profile of oxide formed on an Fe-6Si-1Al alloy after 5 minutes of oxidation in 0.04-0.07 torr of oxygen at 1073 K

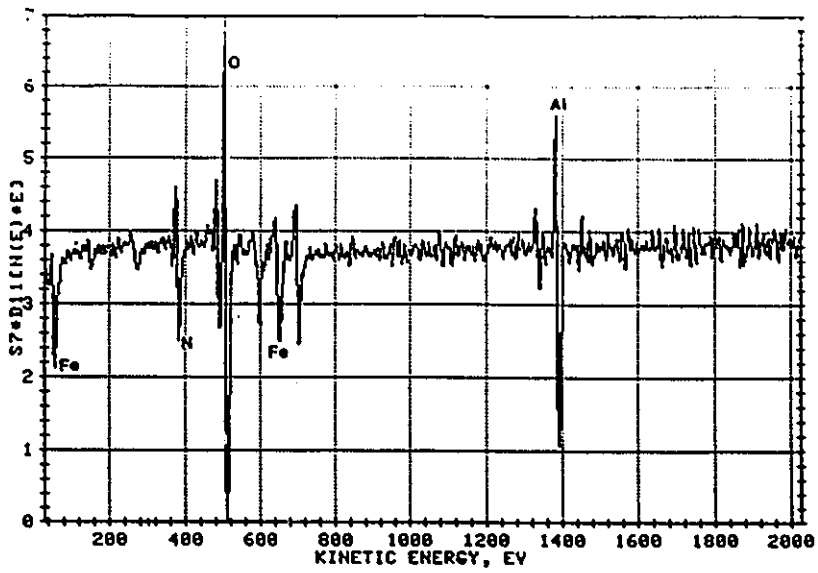

(a)

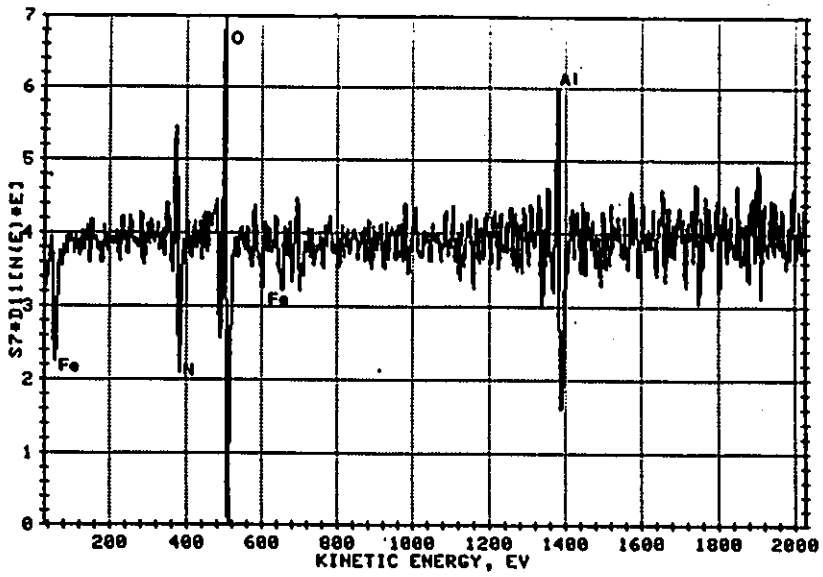

(b)

Fig. 6.9 Auger survey analyses of the oxide formed on Fe-6Si-1Al alloys after 24 hours of oxidation in 0.04-0.07 torr of oxygen at 1073 K. (a) before ion sputtering; (b) after ion sputtering for 30 minutes.

mainly Al_2O_3 doped with Fe. The oxides formed in 0.04-0.07 torr of oxygen were further examined by TEM. Bright field images and associated selected area diffraction (SAD) patterns are shown in Fig. 6.10 (a) and (b). After 5 minutes of oxidation, SAD results indicated the presence of α-Fe_2O_3, β-cristobalite, and α-Al_2O_3. After 50 minutes of oxidation, only α-Al_2O_3 and α-Fe_2O_3 were detected.

Protective oxides were also formed on the alloys oxidized up to 200 and 500 hours in 760 torr of oxygen at 1073 K. Examples are shown in Fig. 6.11 for the alloys after 500 hours of oxidation. The protective oxides exhibit nodular growth which increases with oxidation time. EDAX analyses of these oxide nodules indicated that they were very Al rich with no Si being detected. Auger depth profiles of the oxide formed after 200 hours of oxidation are presented in Fig. 6.12. The results show that the scales formed on these alloys are mainly Al_2O_3 doped with Fe and covered by segments of an Fe rich oxide at the scale surface. These scales have been assumed to be Al_2O_3 doped with Fe since the Al and oxygen concentrations in the profile corresponded well with the composition of Al_2O_3 and Fe was detected across the whole scale. Also, x-ray diffraction analysis of the scale formed after 500 hours of oxidation indicated the presence of α-Al_2O_3 and α-Fe_2O_3, as seen from Fig. 6.13. Auger survey analyses of these oxide scales before and after ion sputtering did not detect any significant Si peaks. Thus the Si profile in Fig. 6.12 may be attributed to background noise.

A cross section of a sample after 500 hours of oxidation in 760 torr of oxygen at 1073 K was prepared by cooling the sample in liquid nitrogen and then fracturing it. The SEM image of the cross section is shown in Fig. 6.11 (c). The oxide scale formed had a thickness of about 7 μm. Compositional information in the oxide scale and in the alloy was obtained using EDAX as shown in Fig. 6.14.

(a) 160000×

(b) 260000×

Fig. 6.10 TEM bright field images and associated SAD patterns for the Fe-6Si-1Al alloy oxidized 5 minutes (a) and 50 minutes (b) in 0.04-0.07 torr of O_2 at 1073 K. The SAD patterns indicate (a) α-Fe_2O_3, β cristobalite, and α-Al_2O_3; (b) α-Al_2O_3 and α-Fe_2O_3.

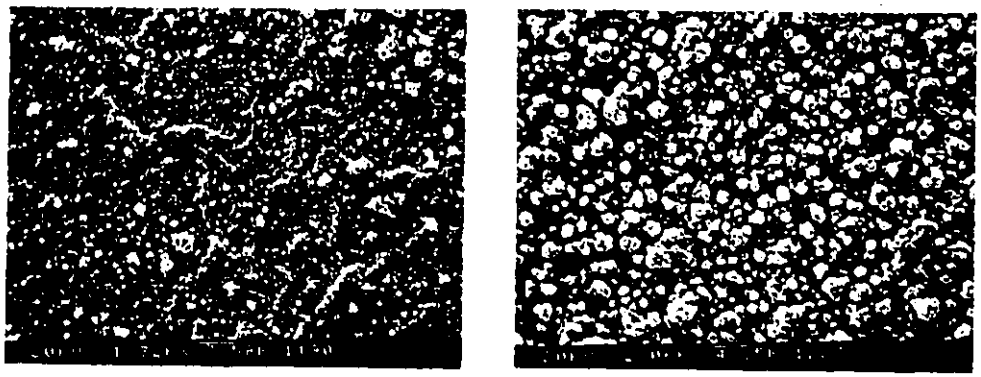

(a) (b)

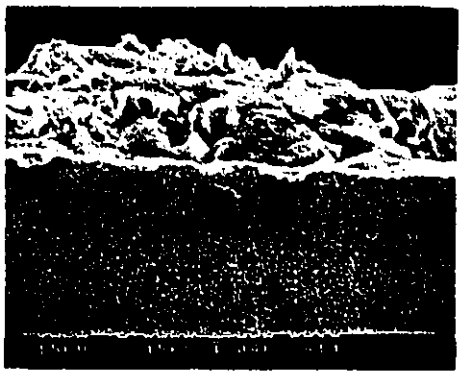

(c)

Fig. 6.11 SEM observations of the oxide morphology formed on Fe-6Si-1Al alloys after 500 hours oxidation in 760 torr of O_2 at 1073 K.

(a) Protective oxide, interspersed with Al rich particles.

(b) Magnified image of (a).

(c) A cross section of a sample.

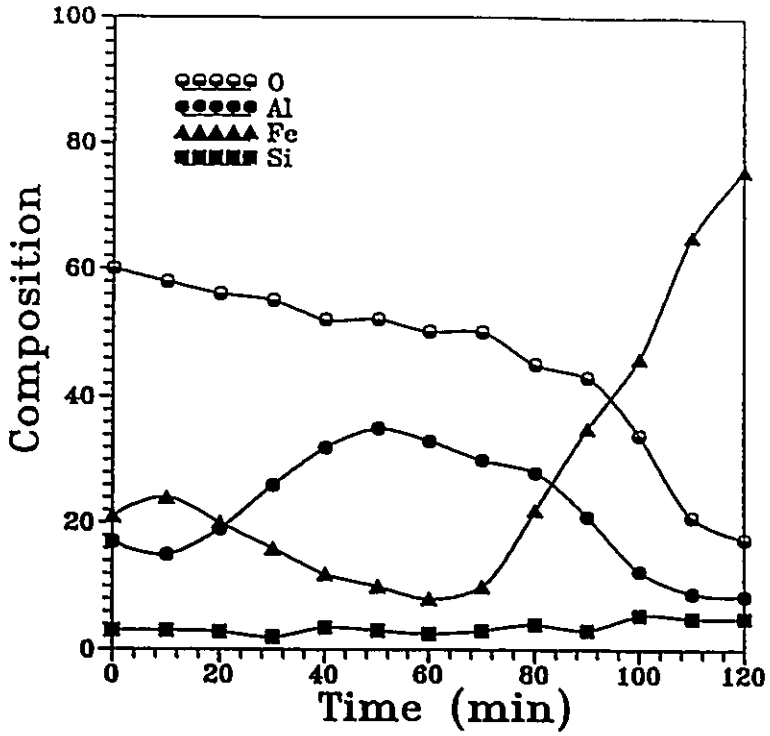

Fig. 6.12 Auger depth profile of oxide formed on an Fe-6Si-1Al alloy after 200 hours of oxidation in 760 torr of oxygen at 1073 K

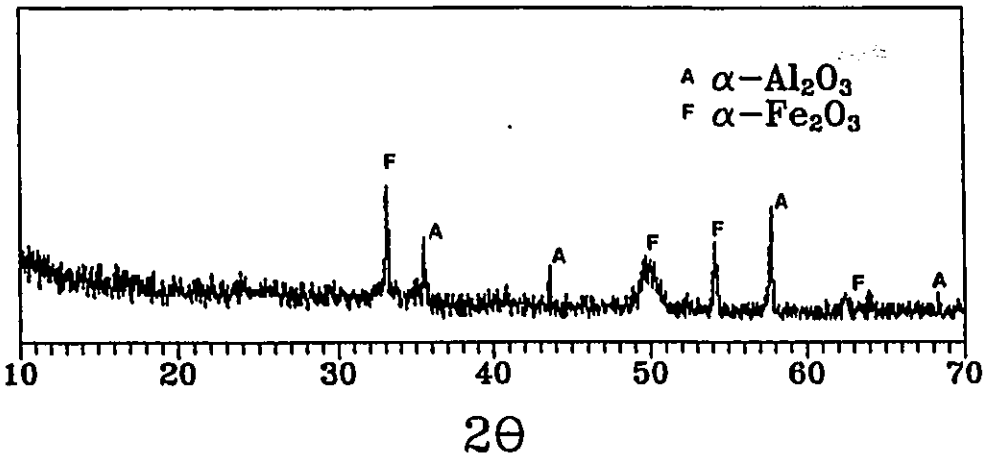

Fig. 6.13 X-ray analysis of the scale formed on the Fe-6Si-1Al alloy after 500 hours of oxidation in 760 torr of O_2 at 1073 K

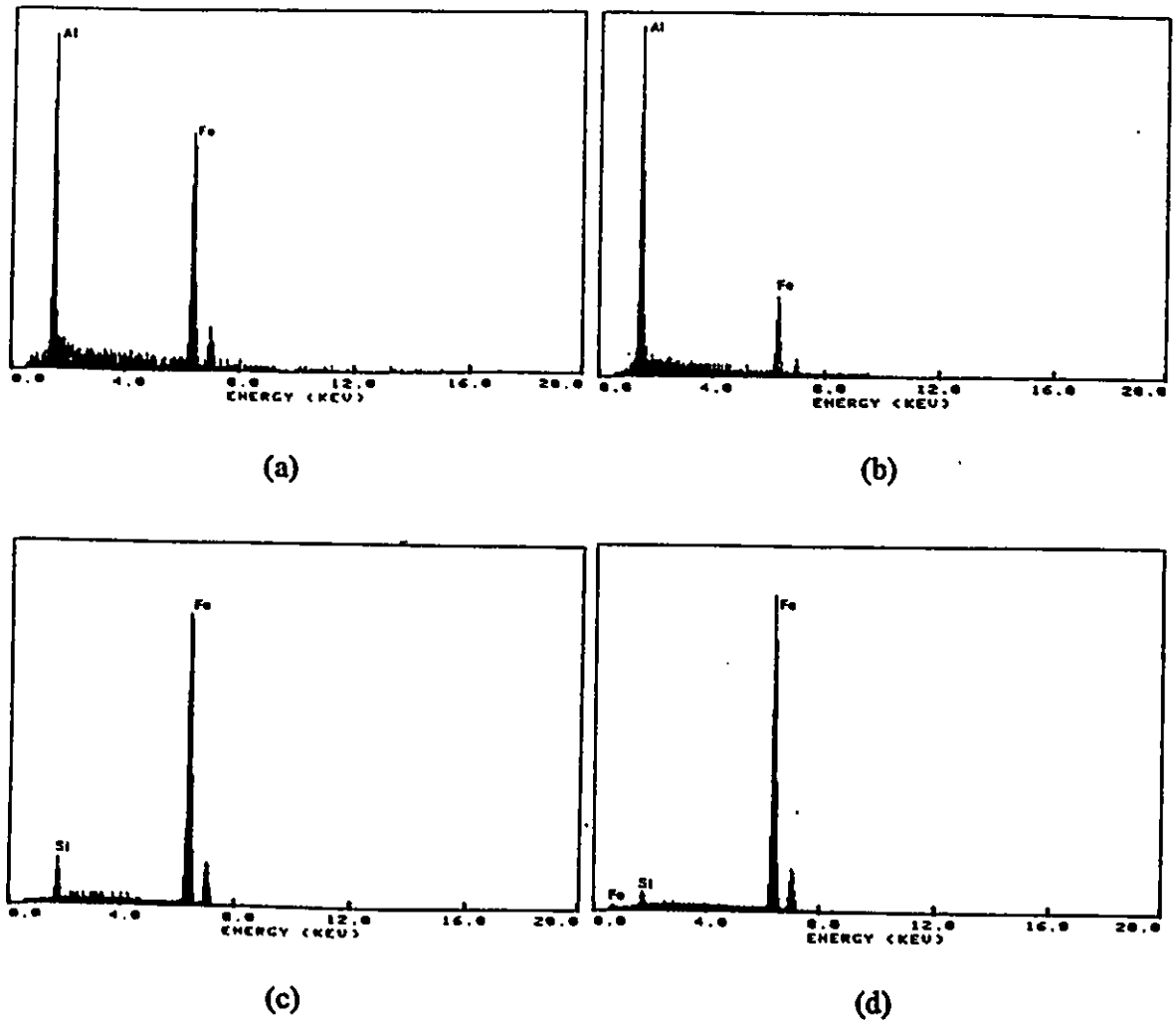

Fig. 6.14 EDAX analyses of the oxide scale in cross section of an Fe-6Si-1Al alloy after 500 hours of oxidation in 760 torr of oxygen at 1073 K. (a) Outer surface of the scale. (b) The bulk of the scale. (c) The alloy side of the scale/alloy interface. (d) The bulk of the alloy.

The results confirm that the oxide formed is mainly Al_2O_3 doped with Fe and covered by segments of Fe_2O_3 at the scale surface. A small amount of Si enrichment was detected at the scale/alloy interface, but Si was not detected in the oxide.

Fig. 6.15 shows SIMS profiles of oxide formed on an Fe-6Si-1Al alloy at 1073 K. The oxide was produced in two stages - first, in ~0.05 torr of $^{16}O_2$ for 7 hours and then in $^{18}O_2$ for another 7 hours. Shown are AlO^{16}, AlO^{18} profiles and the Fe_3 signal which provides an indication of the oxide/alloy interface. An Fe_2^+ signal was detected at the oxide surface, indicating the presence of Fe oxide segments. The expanded Si^+ profile is also shown in the figure. XPS analysis of the oxide formed on an alloy after oxidation under the same conditions as above revealed that there was only about 1.3 at% Si at the outer oxide surface. As seen in Fig. 6.15, the AlO^{18} profile falls from an initial average of ~50% at the outer oxide surface to a low value of 10% at the oxide/alloy interface. There is a noticeable increase in the signal as the oxide/alloy interface is approached. The oxide/alloy interface is broad due to the non-uniformity of the oxide. The general shape of the profile would indicate that there is outward cation diffusion to some extent, but inward oxygen diffusion is the major transport process. The profiles are very similar to the results obtained by Graham and coworkers [6.2] for Fe-25Al alloys oxidized at 1100°C. In the absence of other data, one could conclude that the AlO^{18} profile shows predominantly lattice diffusion of oxygen and that the AlO^{18} shoulder at the oxide/alloy interface illustrates a minor short-circuit (eg. grain boundary) diffusion component [6.2]. The Si peak between the ^{16}O and ^{18}O layers is of interest. The surface of the oxide could have become contaminated with Si from the walls of the heating tube during evacuation between the change over from $^{16}O_2$ to $^{18}O_2$.

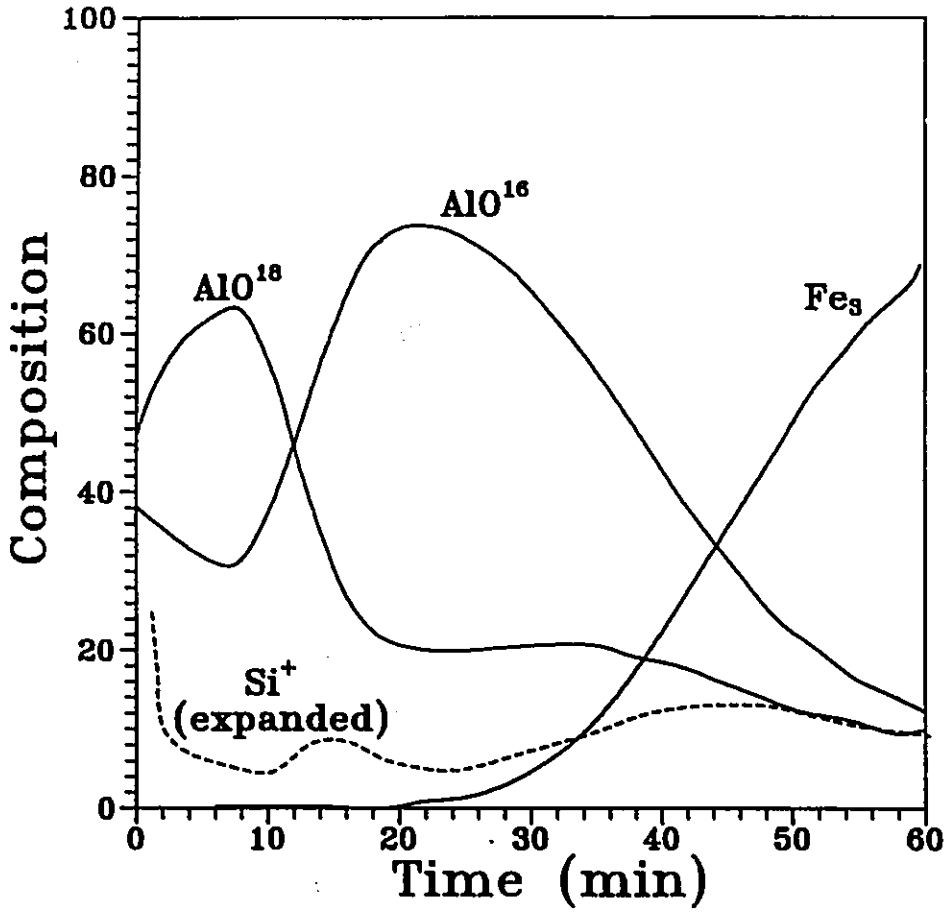

Fig. 6.15 SIMS profiles of Fe-6Si-1Al alloy oxidized at 1073 K first in $^{16}O_2$ for 7 hours followed by 7 hours in $^{18}O_2$.

6.2.2.4 Fe-6Si-3Al

The scale formed on alloys of this composition was protective for periods of up to 6 hours in 0.04-0.07 torr of oxygen at 1073 K and then the oxidation rate accelerated and breakway kinetics were observed as seen from Fig. 6.1. As shown in Fig. 6.16, the oxide was thin and had a convoluted morphology. Oxide nodules which were on the order of several microns in diameter were observed, especially at specimen edges as shown in Fig. 6.16 (c). The nodules occurred predominantly at crests of the convolutions, as seen in Fig. 6.16 (d). Observations of the oxide surface also indicated that voids were associated with the spallation of some oxide nodules which formed at the crests of the convolutions. This resulted in areas of local scale detachment on various samples. These features could account for the breakway kinetics occurring at oxidation times greater than 6 hours.

After oxidation for 200 and 500 hours in 760 torr of oxygen, the oxide formed on the alloys also developed a convoluted morphology. Examples are shown in Fig. 6.17. The oxide ridges grew with oxidation time, thus coarsening the convoluted morphology. Several oxide nodules were found at specimen edges.

Qualitative compositional information obtained from EDAX analyses on various morphological features is summarized in Table 6.5. The results indicate that the convoluted oxide is Al rich, with no indication of Si being present. The particles interspersed at the oxide surface are essentially pure Al oxide. The oxide nodules have a layer of iron rich oxide at the surface, with the Al enrichment increasing with depth into the nodule. Some degree of Al enrichment at the base of voids associated with spallation of some nodules was also observed.

More compositional information of the oxides was obtained by Auger electron spectroscopy. Auger survey analysis indicated that the oxide formed

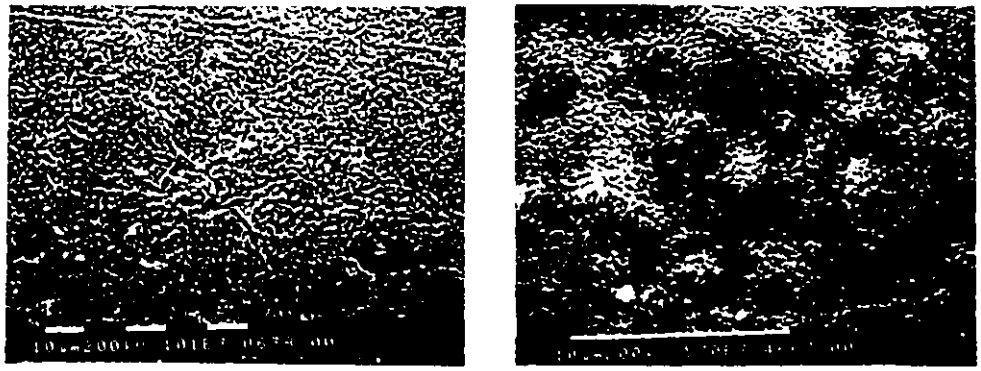

(a) (b)

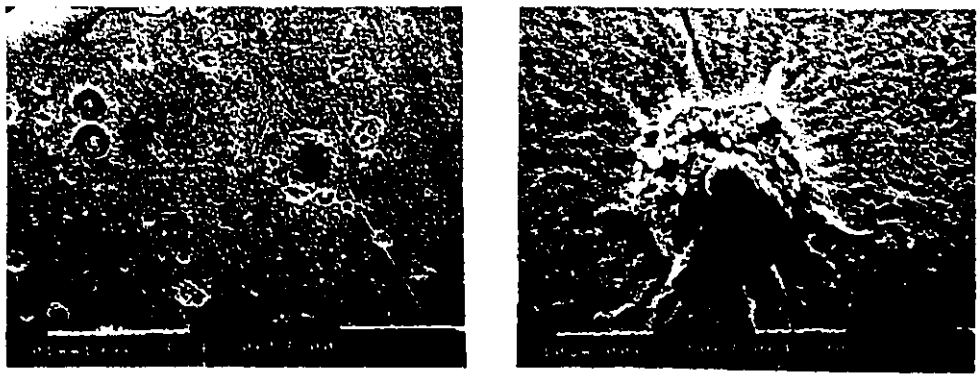

(c) (d)

Fig. 6.16 SEM observations of the oxide morphology formed on Fe-6Si-3Al alloys after 24 hours oxidation in 0.04-0.07 torr of O_2 at 1073 K.

(a) Convoluted oxide, interspersed with Al rich oxide particles.
(b) Magnified image of (a).
(c) oxide nodules and voids formed at the sample edge.
(d) Magnified image of an oxide nodule.

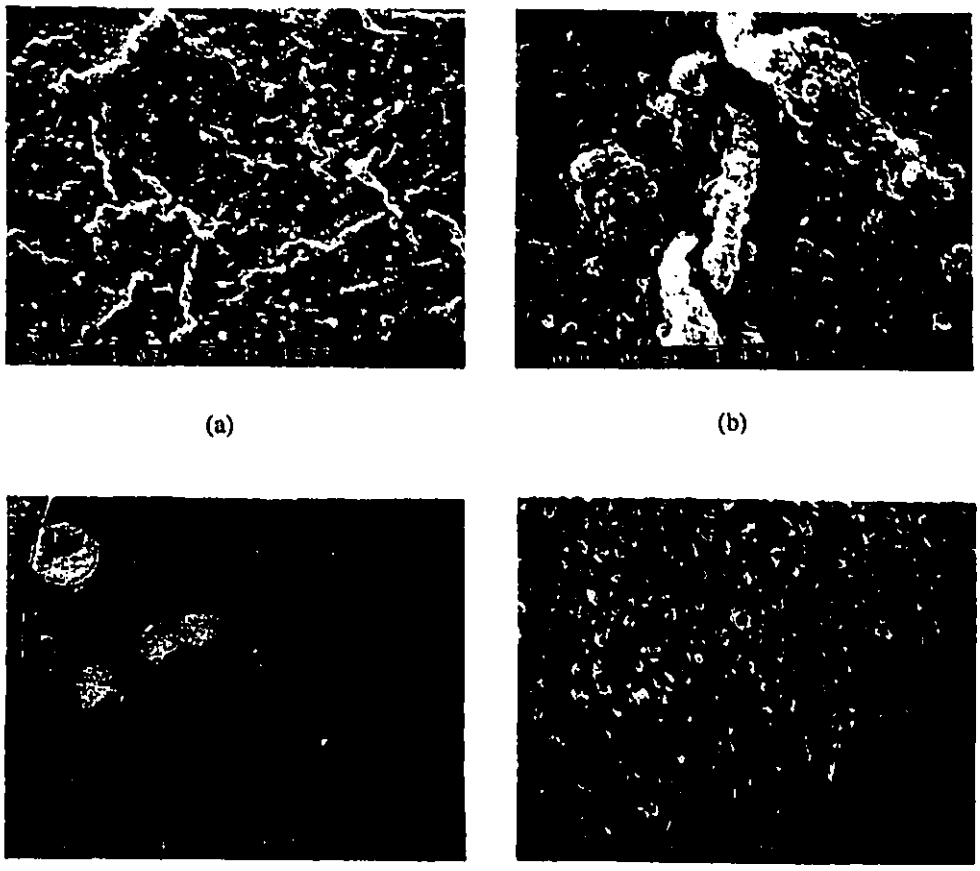

(a) (b)

(c) (d)

Fig. 6.17 SEM observations of the oxide morphology formed on Fe-6Si-3Al alloys after 500 hours oxidation in 760 torr of O_2 at 1073 K.

(a) Convoluted oxide morphology.
(b) Magnified image of (a).
(c) Morphology of the sample edge.
(d) Magnified image of an oxide nodule shown in (c).

Table 6.5 EDAX compositional analysis

Area of analysis	Al counts ($K_{\alpha 1}Al/K_{\alpha 1}Fe$)	Si counts ($K_{\alpha 1}Si/K_{\alpha 1}Fe$)
Alloy substrate	0.028	0.053
Convoluted oxide Fig. 6.16 (a)	0.661	0.009
Oxide voids Fig. 6.16 (a)	0.338	0.067
Oxide particles Fig. 6.16 (a)	23.01	–
Oxide ridges Fig. 6.16 (b)	8.386	–
Oxide nodule (center) Fig. 6.16 (c)	0.037	0.011
Oxide voids Fig. 6.16 (c)	0.458	0.059
Protective oxide Fig. 6.16 (c)	0.983	0.019
Oxide nodule (outer) Fig. 6.16 (d)	0.020	0.047
Oxide nodule (center) Fig. 6.16 (d)	5.468	–
Oxide nodule (edge) Fig. 6.16 (d)	12.20	–
Oxide particles Fig. 6.16 (d)	33.26	–
Oxide ridges Fig. 6.16 (d)	22.08	–

after 24 hours oxidation in 0.04-0.07 torr of oxygen was Al rich as seen in Fig. 6.18. Some enrichment of Fe was observed at the oxide surface, while Si was not detected in the oxide. An Auger depth profile of the oxides formed after 200 hours oxidation in 760 torr of oxygen is shown in Fig. 6.19. The oxygen content of the oxides is consistent with Fe_2O_3 and Al_2O_3, and the profile indicates that the

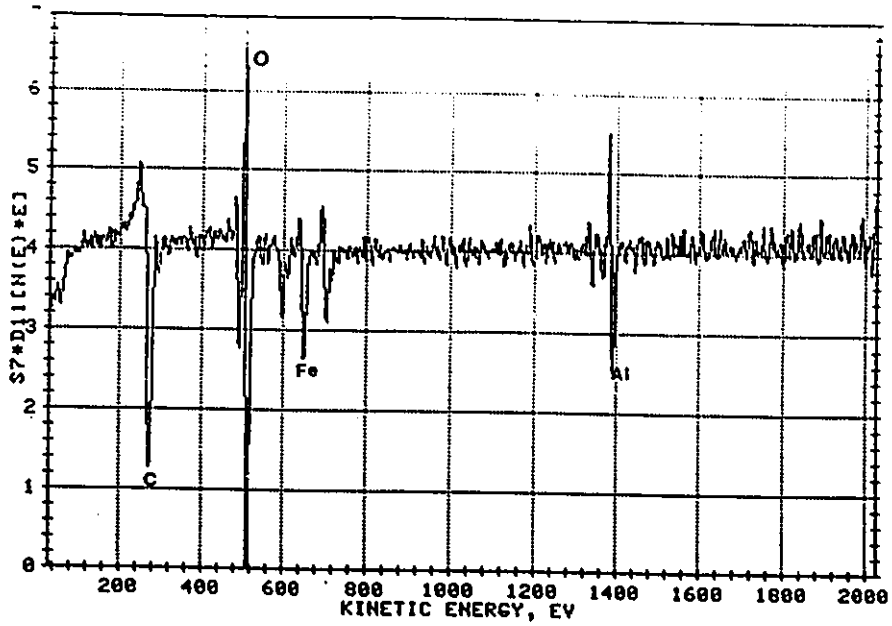

Fig. 6.18 Auger survey analysis of the oxide surface formed on Fe-6Si-3Al after 24 hours oxidation in 0.04-0.07 torr of oxygen at 1073 K.

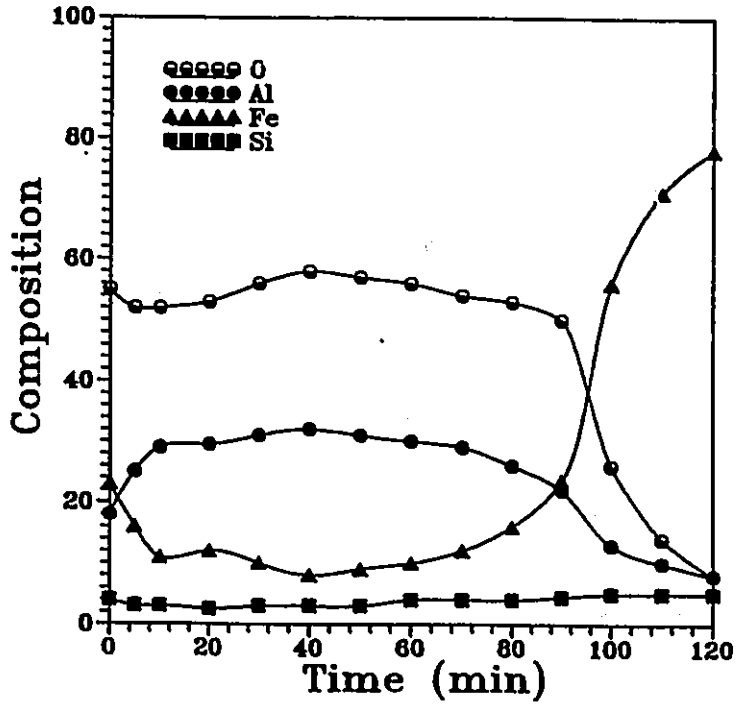

Fig. 6.19 Auger depth profile of oxide formed on Fe-6Si-3Al after 200 hours oxidation in 760 torr of oxygen at 1073 K.

scale is mainly Al_2O_3 covered with Fe_2O_3 segments.

The oxide formed after 24 hours oxidation in 0.04-0.07 torr of oxygen was too thin for X-ray diffraction analysis, and only the α-Fe peak was found by the x-ray diffractometer. X-ray diffraction analysis of the scale formed after 500 hours oxidation in 760 torr of oxygen indicated that it was composed of α-Al_2O_3 and α-Fe_2O_3 as shown in Fig. 6.20. Comparing this x-ray spectra with Fig. 6.13, one can see that the amount of α-Al_2O_3 in the oxide is much higher than that in the oxide formed on the Fe-6Si-1Al alloy.

The oxides formed on the alloys oxidized in 0.04-0.07 torr of oxygen were further examined by TEM. Bright field images and SAD patterns of the oxide examined are presented in Fig. 6.21. After only 5 minutes of oxidation, SAD results indicated the presence of α-Fe_2O_3, β cristobalite and α-Al_2O_3. After oxidation times of 30 minutes, SAD results indicated the presence of α-Al_2O_3 and α-Fe_2O_3, but no β-cristobalite.

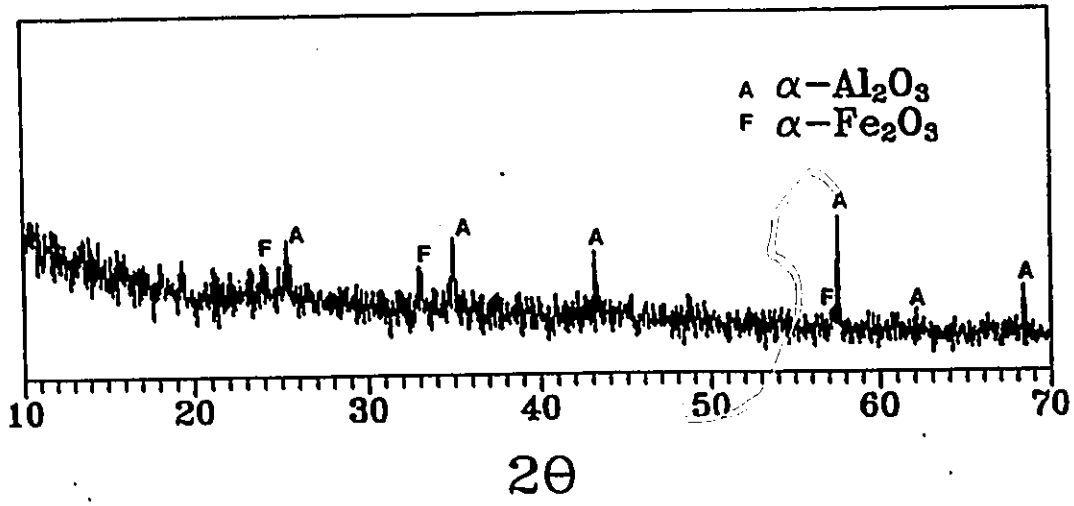

Fig. 6.20 X-ray analysis of the scale formed on the Fe-6Si-3Al alloy after 500 hours of oxidation in 760 torr of oxygen at 1073 K.

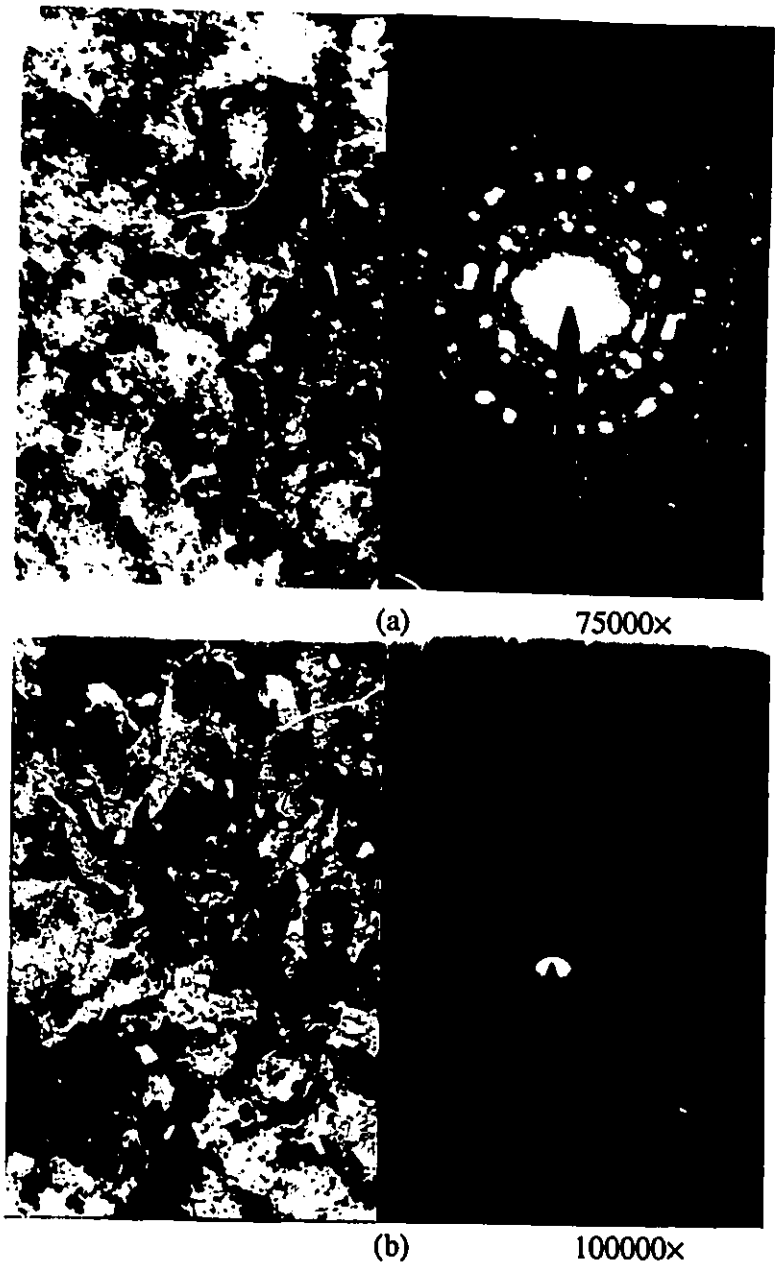

Fig. 6.21 TEM bright field images and associated SAD patterns for the Fe-6Si-3Al alloy oxidized 5 minutes (a) and 30 minutes (b) in 0.04-0.07 torr of O_2 at 1073 K. The SAD patterns indicate (a) α-Fe_2O_3, α-Al_2O_3, and β cristobalite; (b) α-Al_2O_3 and α-Fe_2O_3.

6.2.2.5 Fe-6Si-5Al

Alloys of this composition formed a very protective oxide after 24 hours of oxidation in 0.04-0.07 torr of oxygen at 1073 K. As shown in Fig. 6.22, the oxide formed was typically uniformly flat, although some surface undulations due to oxide convolutions aligned along alloy grain boundaries divided the whole oxide surface into several regions. Three circular ridges with a broken spot at the center were found on the surface, but the rest of the oxide was protective. The oxide grains were very small, about ~0.2 μm in diameter.

After 200 and 500 hours oxidation in 760 torr of oxygen, protective oxide scales also formed. An example is illustrated in Fig. 6.23. The oxide scale was relatively flat, but convoluted morphology was also seen with the larger oxide convolutions apparently aligned along alloy grain boundaries. Examination of a sample cross section revealed that the oxide scale was as thin as ≈4 μm (or less).

Compositional information obtained from EDAX analyses is summarized in Table 6.6. The results indicate that the protective oxide formed on the sample oxidized 24 hours in 0.04-0.07 torr of oxygen was thin and Al rich. There were no differences in either morphology or relative composition between the oxide regions divided by the surface undulations in Fig. 6.22 (a). The surface undulations and ridges which appeared to follow alloy grain boundaries were relatively Al rich. Si was not detected in the oxide formed after 500 hours oxidation in 760 torr of oxygen.

Fig. 6.24 shows the Auger depth profile of the oxide formed after 4 minutes of oxidation in 0.04-0.07 torr of oxygen. The oxide was Al rich, with the oxygen content consistent with Al_2O_3. Some enrichment of Fe and Si was observed at

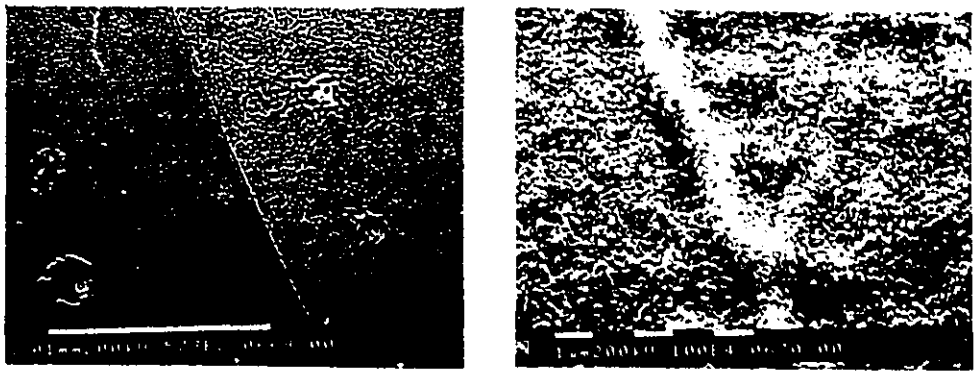

(a) (b)

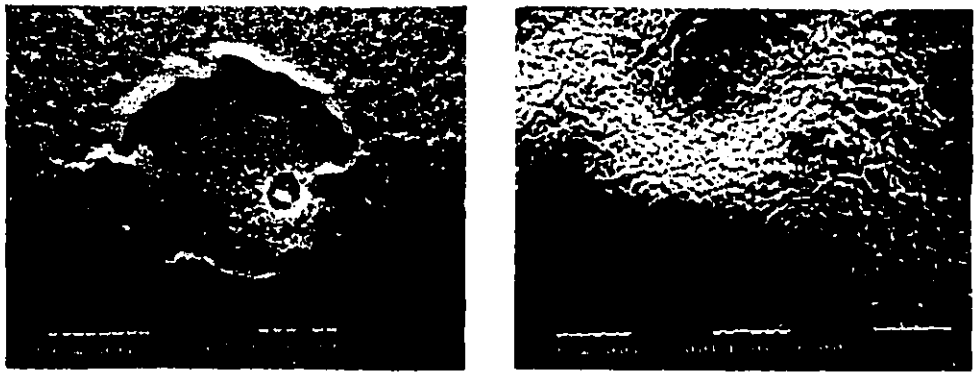

(c) (d)

Fig. 6.22 SEM observations of the oxide morphology formed on Fe-6Si-5Al alloys after 24 hours oxidation in 0.04-0.07 torr of O_2 at 1073 K.

(a) Protective oxide, with some surface undulations divided the whole surface into several regions.
(b) Magnified image of the undulations in (a).
(c) A circular ridge with a broken spot at the center.
(d) Magnified image of the oxide ridge in (c)

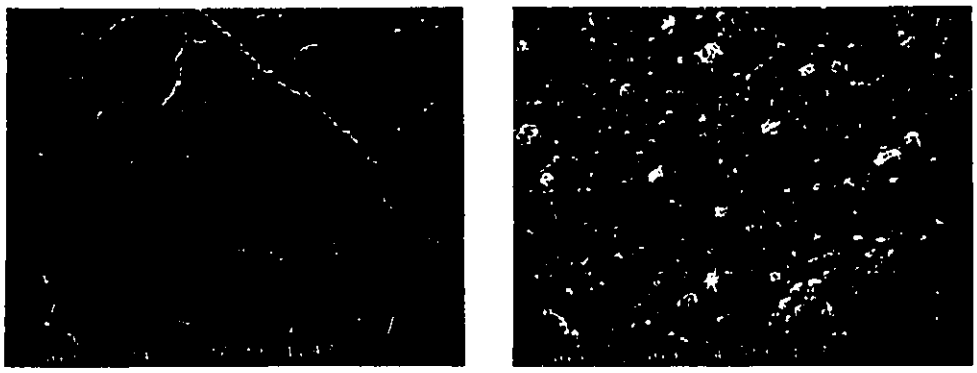

(a) (b)

(c)

Fig. 6.23 SEM observations of the oxide morphology formed on an Fe-6Si-5Al alloy after 500 hours oxidation in 760 torr of O_2 at 1073 K.

(a) Protective oxide, interspersed with Al rich oxide particles.

(b) Magnified image of (a).

(c) The cross section of the sample in (a).

Area of analysis	Al counts ($K_{\alpha 1}Al/K_{\alpha 1}Fe$)	Si counts ($K_{\alpha 1}Si/K_{\alpha 1}Fe$)
Alloy substrate	0.035	0.043
Protective oxide Fig. 6.22 (a), left side	0.231	0.025
Protective oxide Fig. 6.22 (a), right side	0.236	0.024
Surface undulations Fig. 6.22 (b)	0.661	0.018
Circular oxide ridges Fig. 6.22 (c)	0.845	0.008
Flat oxide Fig. 6.22 (c)	0.390	0.017
Oxide particle Fig. 6.22 (c)	1.890	–
Protective oxide Fig. 6.23 (a)	3.984	-
Oxide ridges Fig. 6.23 (a)	4.876	–
Oxide particles Fig. 6.23 (b)	12.56	–
Oxide ridges Fig. 6.23 (b)	7.890	–
Oxide scale Fig. 6.23 (c)	8.034	–

the oxide surface. However, after oxidation for over 24 hours in 0.04-0.07 torr of oxygen, Si was not detected at the outer oxide surface by Auger survey analysis, as shown in Fig. 6.25. The Auger depth profile of the oxide formed on the alloy oxidized in 760 torr of oxygen for 200 hours is shown in Fig. 6.26. The profile indicates that the oxide formed is Al_2O_3 doped with Fe. Some enrichment of Fe is also seen at the oxide surface.

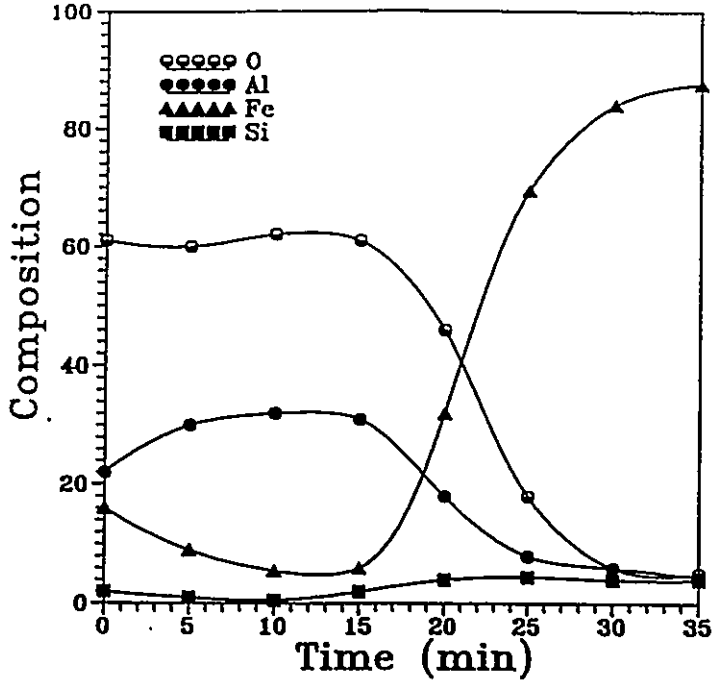

Fig. 6.24 Auger depth profile of oxide formed on an Fe-6Si-5Al alloy after 4 minutes oxidation in 0.04-0.07 torr of oxygen at 1073 K.

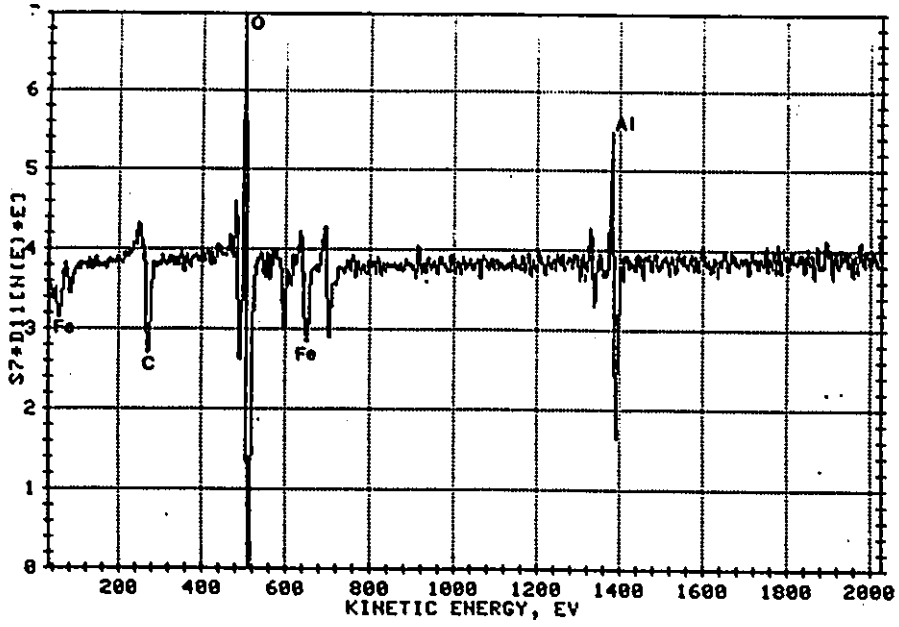

Fig. 6.25 Auger survey analysis of the oxide surface formed on an Fe-6Si-5Al alloy after 24 hours oxidation in 0.04-0.07 torr of oxygen at 1073 K.

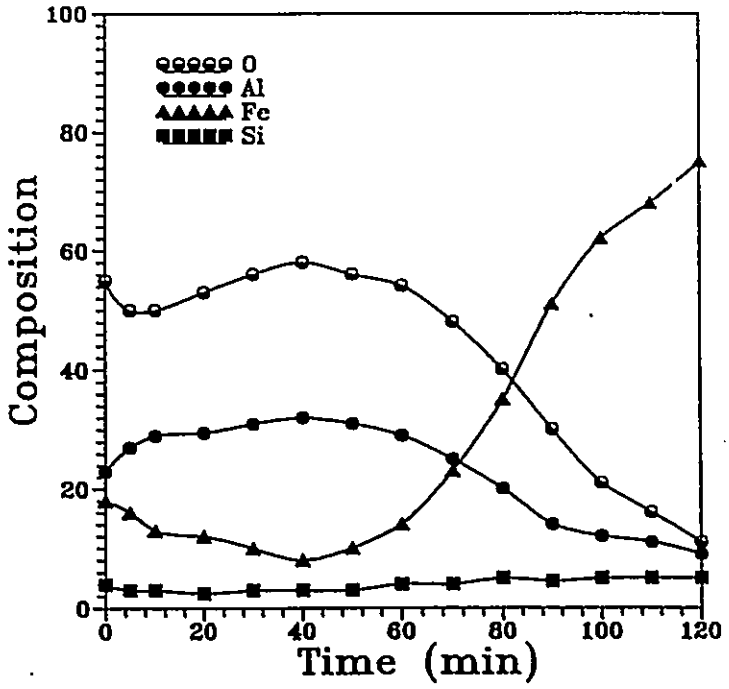

Fig. 6.26 Auger depth profile of oxide formed on an Fe-6Si-5Al alloy after 200 hours oxidation in 760 torr of oxygen at 1073 K.

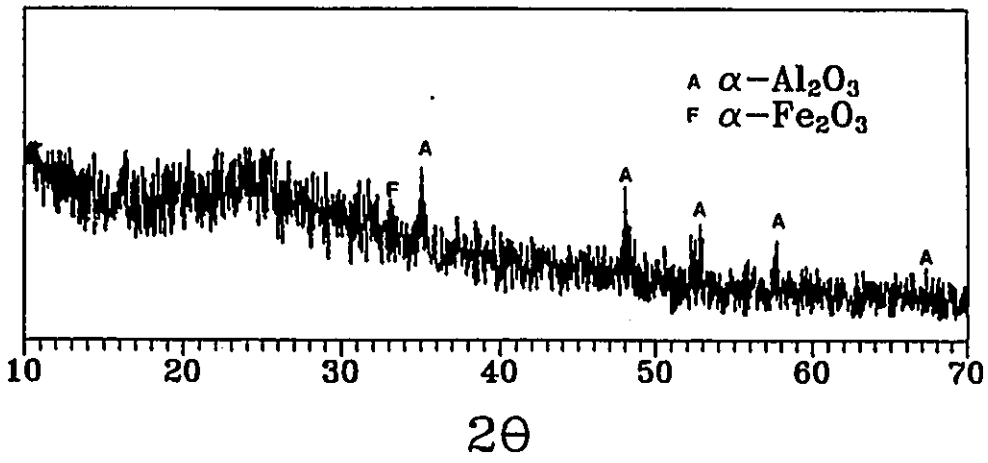

Fig. 6.27 X-ray analysis of the scale formed on the Fe-6Si-5Al alloy after 500 hours of oxidation in 760 torr of oxygen at 1073 K.

X-ray analysis of the oxide formed on the Fe-6Si-5Al alloys after 24 hours oxidation in 0.04-0.07 torr of oxygen showed the presence of the α-Fe substrate only, which indicated that the oxide formed was very thin. The oxide formed on the alloy oxidized in 760 torr of oxygen for 500 hours was identified as α-Al_2O_3 as shown in Fig. 6.27. The α-Fe_2O_3 x-ray signal was very weak.

The oxides formed in 0.04-0.07 torr of oxygen were further examined by TEM. Bright field images and associated SAD patterns obtained are presented in Fig. 6.28 (a) and (b). For the alloy oxidized 2 minutes, SAD results indicate the presence of α-Fe_2O_3, α-Al_2O_3, γ-Al_2O_3, and β cristobalite. After 10 minutes oxidation, only α-Al_2O_3 was observed.

SIMS profiles of oxide formed on an Fe-6Si-5Al alloy at 1073 K are shown in Fig. 6.29. The alloy was oxidized first in $^{16}O_2$ for 8 hours followed by 8 hours in $^{18}O_2$. As seen in the figure, ^{18}O is on the outside but tails in, and there is some Fe oxide at the outer oxide surface. Si was identified by using the mass 29 peak and its extended profile is shown in the figure too. It is seen that there is some Si enriched at the oxide/alloy interface. Indication of the location of the oxide/alloy interface was obtained by detecting the Fe_3 substrate signal.

SIMS profiles of $^{16}O^-$ and $^{18}O^-$ formed on an alloy oxidized first in $^{16}O_2$ for 7.5 hours and followed by 7.5 hours in $^{18}O_2$ were also obtained as shown in Fig. 6.30. The SIMS data is plotted on a logarithmic intensity scale. Results of XPS analysis performed before the SIMS profiles indicated that there was only 2.62 at% Fe and 1.00 at% Si at the outer oxide surface, and the oxygen and Al contents corresponded very well to Al_2O_3. The profile of $^{18}O^-$ in Fig. 6.30 indicates significant inward diffusion of oxygen.

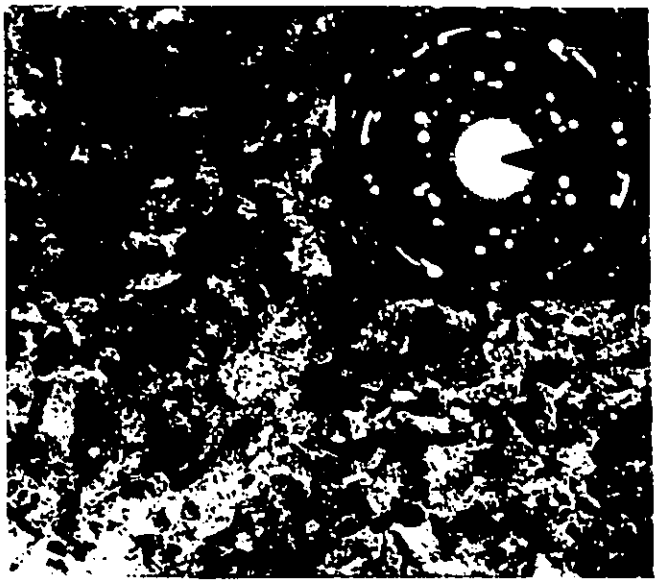

(a) 22000×

(b) 260000×

Fig. 6.28 TEM bright field images and associated SAD patterns for Fe-6Si-5Al alloys oxidized 2 minutes (a) and 10 minutes (b) in 0.04-0.07 torr of O_2 at 1073 K. The SAD patterns indicate (a) α-Fe_2O_3, α-Al_2O_3, γ-Al_2O_3, and β cristobalite; (b) α-Al_2O_3 only.

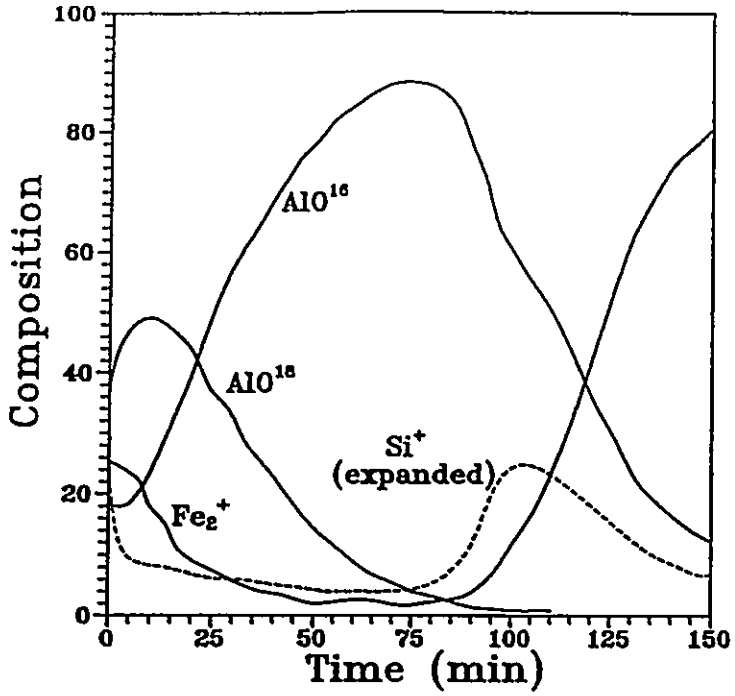

Fig. 6.29 SIMS profiles of Fe-6Si-5Al alloy oxidized at 1073 K first in $^{16}O_2$ for 8 hours followed by 8 hours in $^{18}O_2$.

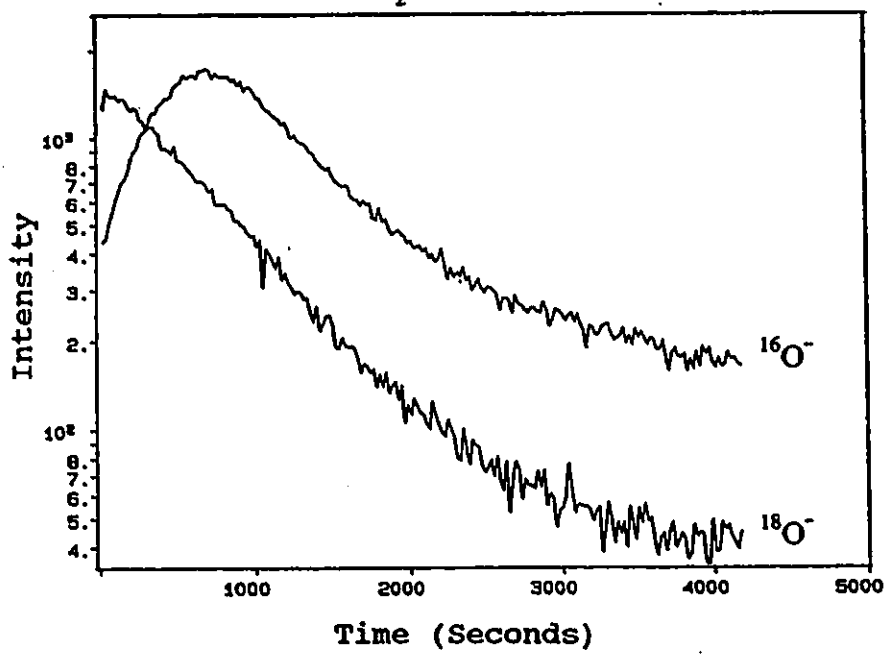

Fig. 6.30 SIMS profiles of Fe-6Si-5Al alloy oxidized at 1073 K first in $^{16}O_2$ for 7.5 hours followed by 7.5 hours in $^{18}O_2$.

6.3. Ni-1Si-4Al Alloys

Ni-1Si-4Al alloys were oxidized at 1073 K in oxygen at the dissociation pressure of NiO by using Ni/NiO packs for periods of 8, 20, 48, 120, and 500 hours. After oxidation, the samples were mounted vertically and vacuum impregnated with cold setting epoxy resin. They were polished in cross-section with 600 grit SiC abrasive papers and finally polished down to ~ 1 μm. Optical microscopy was used to study the morphology of the reaction product. A typical photomicrograph of the polished cross section of the sample oxidized 120 hours is shown in Fig. 6.31. The alloys exhibited uniform internal oxide penetration even in the vicinity of alloy grain boundaries. The depths of internal oxidation penetration in the alloys were measured by a LE2001 image analyzer. The results are given in Table 6.7.

Table 6.7 Depths of internal oxidation of Ni-1Si-4Al alloys oxidized at 1073 K in Ni/NiO packs.

Oxidation time (hours)	Depth (μm)
8	2.60±1.50
20	5.00±1.80
48	11.56±1.90
120	18.59±1.40
500	38.68±3.17

Fig. 6.31 A photomicrograph of the polished cross section of the internal oxidation zone in the Ni-1Si-4Al alloy oxidized at 1073 K in Ni/NiO packs for 120 hours

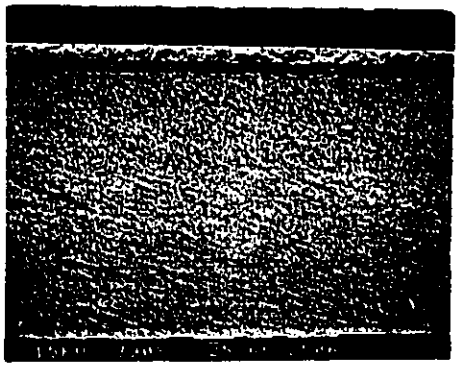

Fig. 6.32 SEM micrograph of the polished cross section of the internal oxidation zone in the Ni-1Si-4Al alloy oxidized at 1073 K in 760 torr of oxygen for 500 hours

For most of the Ni-1Si-4Al samples oxidized in Ni/NiO packs, protrusions were observed along the exposed surfaces. The protrusions tended to increase in size and in number density with increasing oxidation time. On samples oxidized for 120 hours, a thin external layer was observed along the exposed surfaces as can be seen in cross section in Fig. 6.31. Both EDAX and X-ray diffraction analyses indicated the surface protrusions and the thin external layer were essentially pure nickel. After polishing these internal oxide-denuded Ni nodules or thin layers, internal oxide precipitates were extracted by dissolving metals with a 10% iodine/methanol solution and then examined by X-ray diffractometer and TEM selective diffraction analysis. The results indicated that the internal oxide was a mixture of α-Al_2O_3 and β-cristobalite.

Ni-1Si-4Al alloys were also oxidized in 760 torr of oxygen for periods of 50, 120, 260, and 500 hours. The alloys exhibited uniform internal oxidation in combination with external oxidation, as seen in Fig. 6.32. The thickness of the external oxide layers and the depth of the internal oxidation zones are listed in Table 6.8. EDAX and x-ray diffraction analyses indicated that the external oxide was NiO and the internal oxide was a mixture of α-Al_2O_3 and monoclinic tridymite (another form of SiO_2). The external scale of NiO grew essentially according to a parabolic rate law with a rate constant $k_C \approx 3.83 \times 10^{-13}$ cm^2/sec.

Table 6.8 Thickness of external oxide layers and depth of internal oxidation of Ni-1Si-4Al alloys oxidized in 760 torr of oxygen at 1073 K.

Oxidation time (hours)	Thickness of NiO (μm)	Depth of internal oxide (μm)
50	5.80±1.10	18.68±0.76
120	8.36±1.00	33.41±1.15
260	9.91±0.50	49.56±1.24
500	12.16±3.17	64.32±0.50

CHAPTER 7

Analysis and Discussion

7.1 Introduction

In this chapter, experimental results on the oxidation properties of Fe-Si-Al, Ni-Cr-Al, and Ni-Si-Al ternary alloys, obtained from either this study or the literature, are analyzed and discussed. The theoretical considerations of ternary alloy oxidation, described in chapter 4, are applied to the above alloy systems. To apply these models, thermodynamic and diffusion properties of these ternary systems, if not available from the literature, are evaluated based upon the theoretical principles described in chapter 2. The applicability of the theoretical considerations is discussed.

7.2 Evaluations of Thermodynamic and Diffusion Properties

7.2.1 Thermodynamic Consideration for the Fe-Si-O System

In this section, thermodynamic data from the literature are used to calculate the activity variations of Fe and Si in the Fe-Si system at 1073 and 1173 K. The activity data are then applied to estimate the stable oxide phase in equilibrium with the metal phase and to derive oxygen pressure-composition

1173 K. The activity data are then applied to estimate the stable oxide phase in equilibrium with the metal phase and to derive oxygen pressure-composition equilibrium diagrams, assuming that the activity of the oxide phase is unity.

Referring to the Fe-Si phase diagram shown in Fig. 3.3, there are four possible phases at 1073 K for the Fe-Si system in the whole composition range: bcc–Fe, ε (FeSi), ζ_β ($FeSi_2$), and (Si). Three ordering reactions take place in the bcc-Fe solid solution. They are the ferro-paramagnetic transition, the α/α_2 atomic ordering transition and α_2/α_1 atomic ordering transition. Thus the excess free energy of the bcc-Fe solution $G^E(N_{Si}^\dagger,T)$ is expressed as:

$$G^E(N_{Si}^\dagger,T) = G_\alpha^E(N_{Si}^\dagger,T) + G^{mag}(N_{Si}^\dagger,T) + G^{ord}(N_{Si}^\dagger,T) \qquad (7.1)$$

where $N_{Si}^\dagger$ is the mole fraction of Si, and T is the temperature in K. The first term in Eq. (7.1) is given in Eq. (3.2) (note that $N_{Fe}^\dagger = 1 - N_{Si}^\dagger$). The second and third terms are the magnetic ordering energy and the atomic ordering energy, respectively, and are given by Lee *et al.* [7.1]. The activities of Fe and Si in the bcc-Fe solution can be calculated using Eq. (2.3).

If a compound $A_{1-x}B_x$ (phase 1) is stoichiometric, the chemical potential of the compound μ(1) is equal to the molar Gibbs free energy of the compound $G^o(1)$, and is related to the chemical potentials of A and B (μ_A and μ_B) as [7.2]

$$G^o(1) = \mu(1) = (1-x)\mu_A + x\mu_B \qquad (7.2)$$

For the equilibrium between two compounds 1 and 2, one obtains

$$\mu_B = \frac{G^\circ(1)/x_1 - G^\circ(2)/x_2}{x_1/(1-x_1) - x_2/(1-x_2)} \quad . \tag{7.4}$$

Therefore, one can use Eq. (7.3) and (7.4) to calculate the activities of Fe and Si in the composition range of intermetallic compounds and pure Si (Si), assuming all of them are stoichiometric. The required values of Gibbs free energies of the compounds and (Si) are based on data in Ref. [7.1].

The calculated activity variation of Fe and Si in the Fe-Si system at 1073 K is shown in Fig. 7.1. Similarly, the activity variation in the system at 1173 K was calculated. To enable the theoretical estimation to be compared with experimental data, the activity variation of Fe in the bcc-Fe solid solution at 966 K was also calculated. Calculated results agree very well with the experimental data of Vecher *et al.* [7.3] as shown in Table 7.1.

Table 7.1 Activity of Fe, a_{Fe}, in the solid Fe-Si alloys at 966 K

Mole fraction of Fe	a_{Fe}(measured, [7.3])	a_{Fe} (calculated)
0.914	0.84±0.01	0.812
0.880	0.77±0.04	0.757
0.834	0.76±0.02	0.753
0.828	0.78±0.03	0.752
0.811	0.75±0.02	0.750
0.807	0.78±0.05	0.749
0.770	0.72±0.05	0.698
0.755	0.69±0.06	0.671

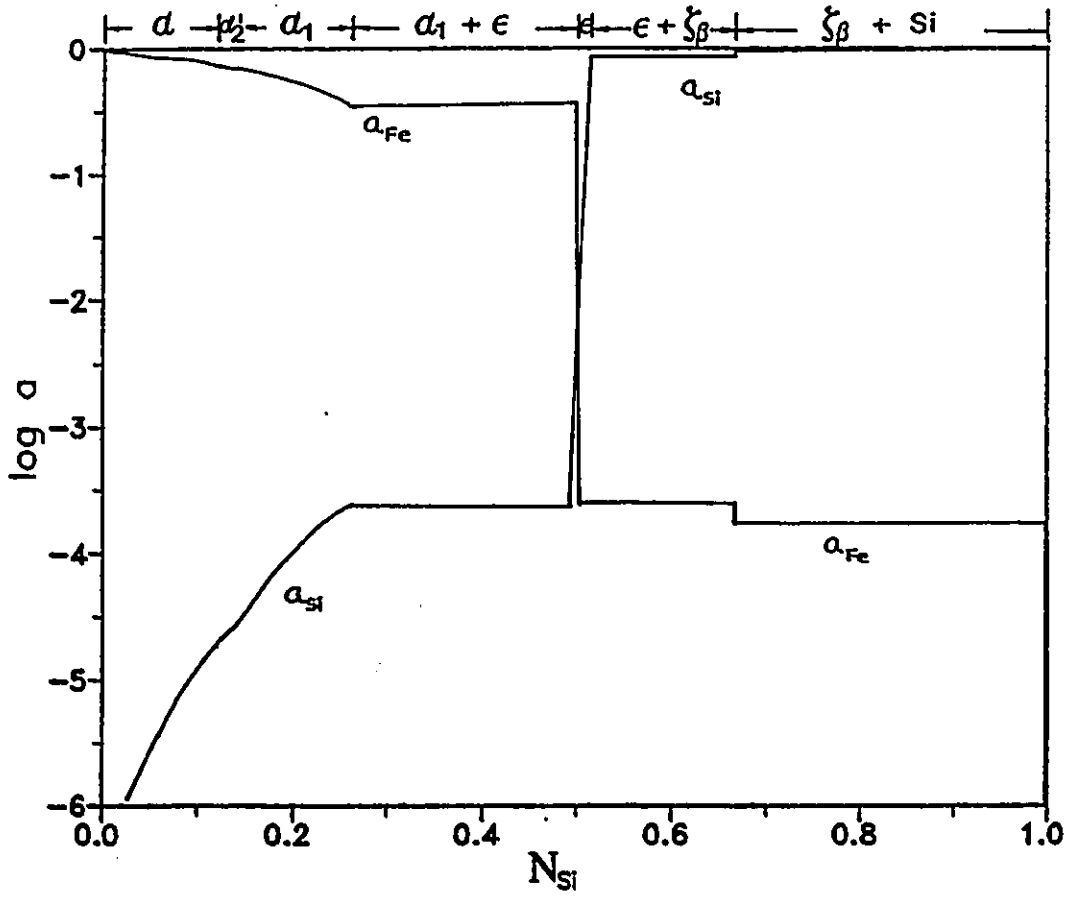

Fig. 7.1 Activities of Fe and Si in the Fe-Si system at 1073 K

The addition of Si into the Fe-O system introduces two important phases: silica and fayalite. 12 cases are present [7.4]: (1) silica + magnetite (M) + hematite (H) coexisting with gas; (2) silica + fayalite + M with gas; (3) fayalite + M + wustite (W) with gas; (4) fayalite + W + alloy with gas; (5) fayalite + silica + alloy with gas; (6) fayalite + W + alloy with gas; (7) fayalite + M with gas; (8) H + silica with gas; (9) M + silica with gas; (10) fayalite + alloy with gas; (11) fayalite + silica with gas; and (12) silica + alloy with gas.

The oxygen equilibrium pressure of a metal/oxide mixture can be calculated from the corresponding Gibbs free energy of formation, ΔG, taken from Elliot and Gleiser [7.5] or from Taylor and Schmalzried [7.6]. For instance, for the formation of SiO_2

$$Si + O_2 = SiO_2 \tag{7.5}$$

$$\Delta G = RT \ln K = RT \ln \frac{a_{SiO_2}}{a_{Si} p_{O_2}} \tag{7.6}$$

Assuming that the activity of the oxide is unity, one can calculate the oxygen equilibrium pressure from Eq. (7.6) based on the activity data of the metal estimated above. In an analogous manner, the oxygen pressure for an equilibrium between two oxides can also be calculated. The calculated results were used to establish oxygen pressure-composition equilibrium diagrams of the Fe-Si-O system at 1073 and 1173 K as shown in Fig. 7.2 and 7.3, respectively. The dissolved oxygen in the alloy will affect the activities of Fe and Si, but considering the extremely low solubility of oxygen in the solid Fe-Si system (*i.e.*, 2 ppm in iron at 1373 K [7.7]), we may ignore the effect of the dissolved oxygen.

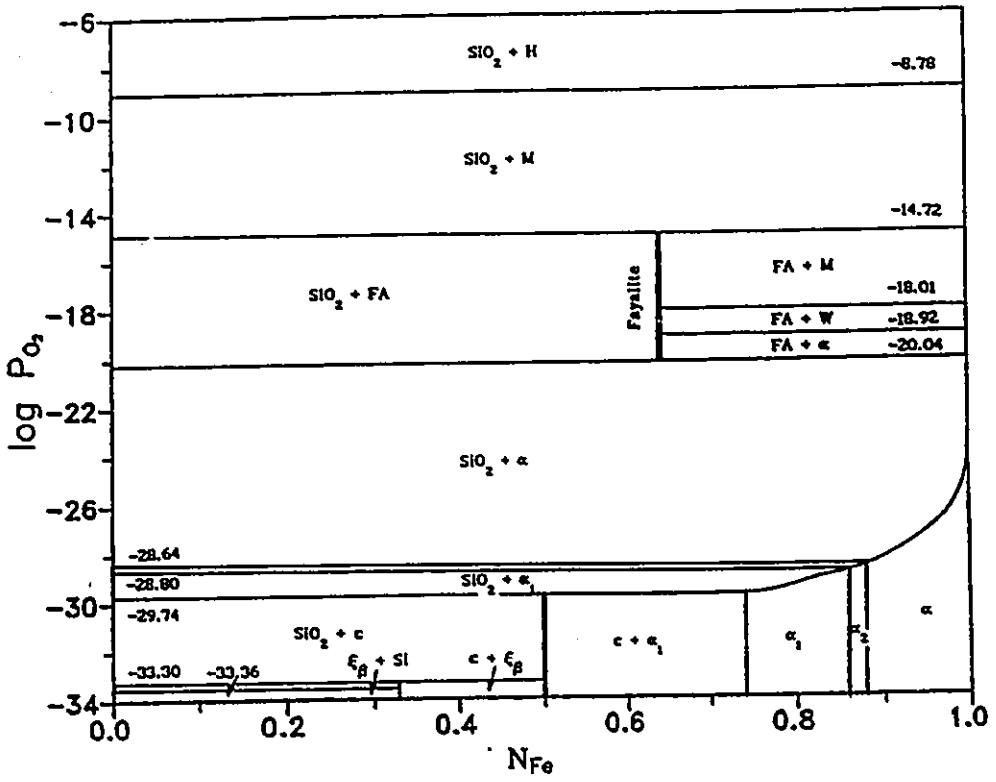

Fig. 7.2 Oxygen pressure-composition equilibrium diagram for the Fe-Si-O system at 1073 K

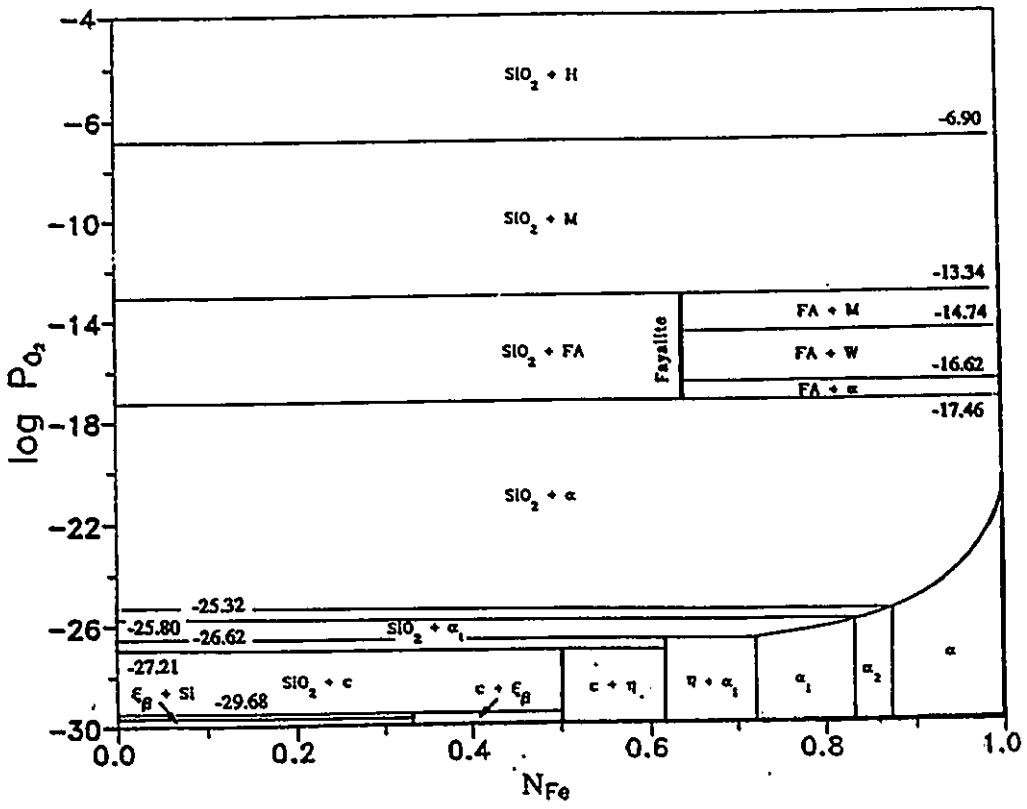

Fig. 7.3 Oxygen pressure-composition equilibrium diagram for the Fe-Si-O system at 1173 K

The above thermodynamic considerations provide a starting point for predicting the oxidation of Fe-Si alloys. Based on the alloy composition and oxygen partial pressure, it is possible to make predictions as to the oxidation products which the Fe-Si alloys are likely to form at 1073 and 1173 K. However, it should be borne in mind that the thermodynamic predictions are of limited value only, since the oxidation process is both a kinetic and thermodynamic problem which is governed by a number of factors. Accordingly, some reaction products that are expected on thermodynamic grounds may not form, and others may form.

7.2.2 Thermodynamic and Diffusion Properties of the Fe-Si-Al System

In what follows, the activity variations of Al and Si in the α–Fe region of the solid Fe-Si-Al ternary system are evaluated from the thermodynamic properties of the limiting binary systems. The activity data are then applied to estimate the interdiffusion coefficients of Al and Si in the Fe-Si-Al alloys.

As shown in Fig. 3.4, there exists a very wide range of composition in the α–Fe solid solution region of the Fe-Si-Al system. This is an indication of large repulsive thermodynamic interactions in the ternary system. Referring to the discussions in chapter 2, we may choose Chou's model to represent the Gibbs excess free energy of the α-Fe solid solution in the Fe-Si-Al system by taking into account the limiting binary systems. The excess free energies of the Fe-Al, Fe-Si and Al-Si binary systems are given in Eq. (3.1), (3.2) and (3.3), respectively. By applying Eq. (2.3), the activity coefficients of Al and Si in the α-Fe region were obtained as functions of temperature (T) and alloy mole fractions (N_{Al} and N_{Si})

$$\ln \gamma_{Si} = \frac{1 - N_{Al} - N_{Si}}{T} \left\{ \left[15.5T - 20129.9 \right] N_{Si} \left[1 - N_{Al} - N_{Si} \right] + N_{Si} \left[7045.46 + 1.71T - N_{Al} \left[20.53T - 28181.86 \right] \right] \right\} \quad (7.7)$$

and

$$\ln \gamma_{Al} = \ln \gamma_{Si} + \frac{1}{T} \left[N_{Si} \left[1107.16 + \frac{(4.95T - 2395.48)N_{Si} + 3150.35 - 6.21T}{1 - N_{Si}} \right] + 75.49 - 0.80T + (1 - N_{Al} - N_{Si})[N_{Al}(20.53T - 28181.86) - 7045.47 - 1.71T] \right] \quad (7.8)$$

In a concentration range of $0 < N_{Si} < 0.2$ and $0 < N_{Al} < 0.2$, the predictied effects of Si additions to the Fe-Si-Al alloys on the activity coefficient of Al at 1073 and 1173 K are shown in Fig. 7.4 and 7.5, respectively. Interactions between Si and Al in the bcc-iron region increase significantly the activity of Al. In contrast, it was found that the activity of Si increases only slightly with increasing Al and Si concentrations.

To enable our theoretical estimation to be compared with experimental measurement, we have also used Chou's model to evaluate the activity coefficient of Al in the liquid Fe-Si-Al alloy containing 2 at% Si and 2 at% Al at 1823 K. The excess free energies of the limiting binary systems are taken from Ref. [3.13], [3.21] and [3.23]. The calculated activity coefficient of Al, 0.271, agrees reasonably well with the value of 0.313 measured by Batalin and coworkers [7.8].

Having evaluated the activity variation of Al and Si in the Fe-Si-Al system, we used Eq. (2.15) and (2.16) to estimate the interdiffusion coefficients of the ternary system. Values of self diffusion coefficients of Al and Si in Fe are based on data by Nishida *et al.* [7.9] (for Al in Fe) and by Borg and Lai

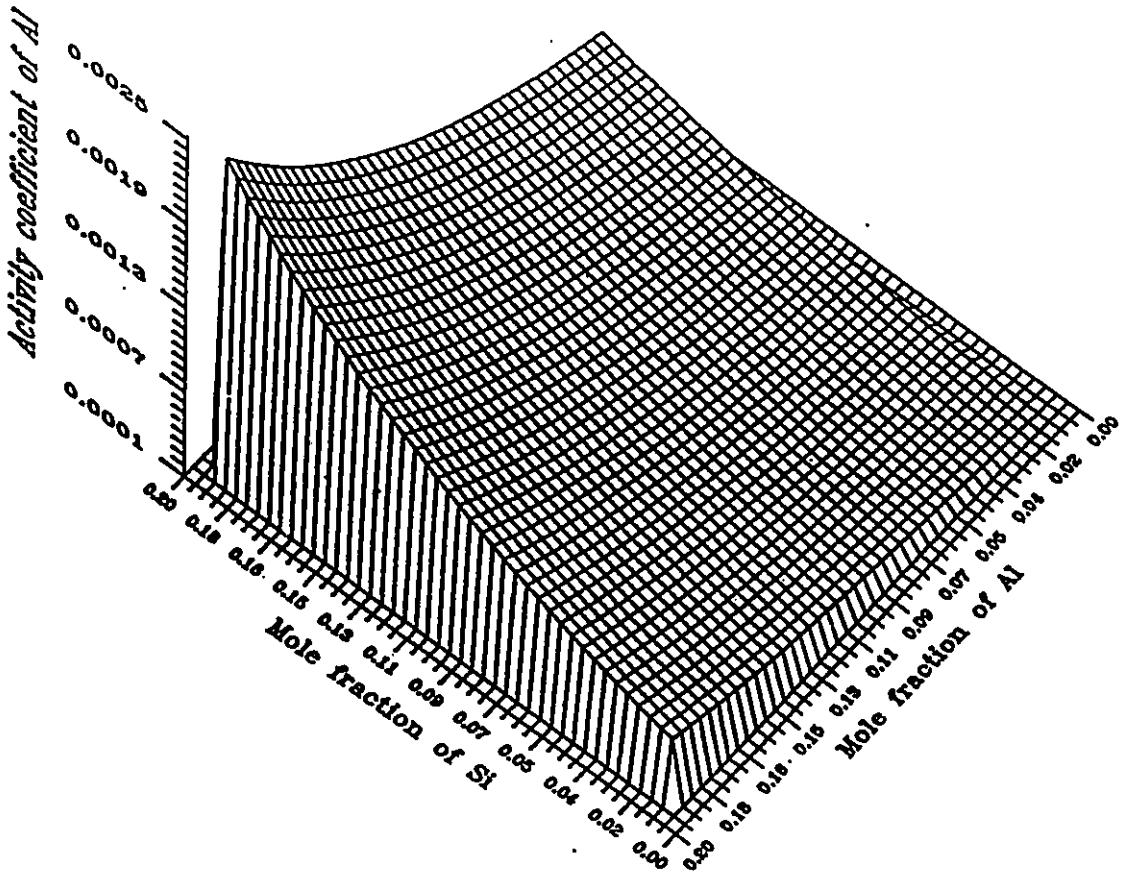

Fig. 7.4 Variation of the activity coefficient of Al in the Fe-Si-Al system at 1073 K

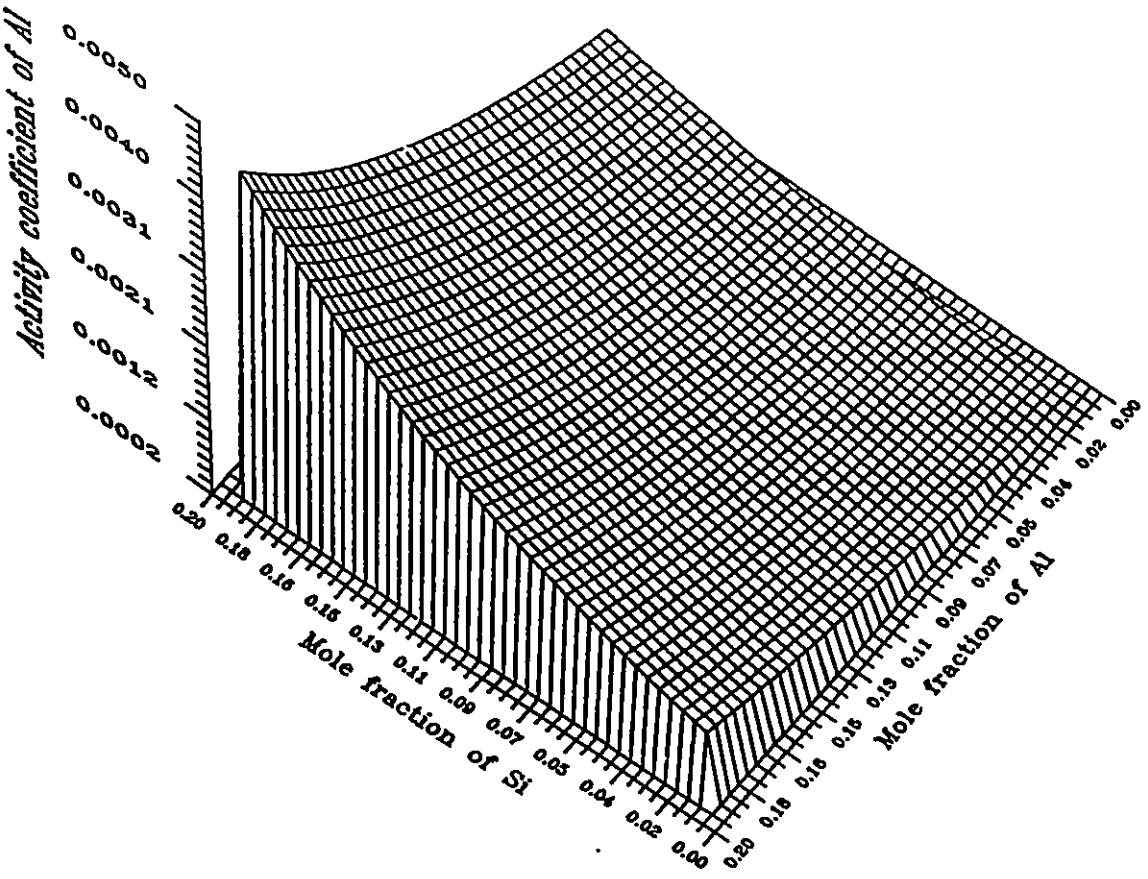

Fig. 7.5 Variation of the activity coefficient of Al in the Fe-Si-Al system at 1173 K

[7.10] (for Si in Fe), respectively. The estimated interdiffusion coefficients at 1073 and 1173 K as functions of Si and Al bulk concentrations are given in Table 7.2.

Table 7.2 The estimated interdiffusion coefficients of the Fe-Si-Al system at 1073 and 1173 K (in units of 10^{11}·cm^2/sec)

1073 K

$$D_{SiSi} = 1.49 - 13.58N_{Si} + 18.43N_{Al} - 40.71N_{Si}^2 - 62.70N_{Si}N_{Al} + 225.8N_{Si}^3 - 188.6N_{Si}^2N_{Al} - 45.72N_{Si}N_{Al}^2$$

$$D_{SiAl} = 12.30N_{Si} - 149.9N_{Si}^2 - 145.0N_{Si}N_{Al} - 42.05N_{Si}^3 - 152.7N_{Si}^2N_{Al} - 119.3N_{Si}N_{Al}^2$$

$$D_{AlSi} = 6.96N_{Al} + 9.98N_{Al}^2 + 46.38N_{Si}N_{Al} - 22.58N_{Al}^3 - 31.37N_{Si}^2N_{Al} - 32.73N_{Si}N_{Al}^2$$

$$D_{AlAl} = 2.51 + 27.15N_{Al} + 16.03N_{Al}^2 + 9.99N_{Si}N_{Al} - 43.18N_{Al}^3 - 16.37N_{Si}^2N_{Al} - 45.15N_{Si}N_{Al}^2$$

1173 K

$$D_{SiSi} = 12.30 + 130.3N_{Si} + 150.4N_{Al} - 169.2N_{Si}^2 - 303.1N_{Si}N_{Al} + 938.8N_{Si}^3 + 257.8N_{Si}^2N_{Al} - 72.34N_{Si}N_{Al}^2$$

$$D_{SiAl} = 93.59N_{Si} + 1107.0N_{Si}^2 + 1058.0N_{Si}N_{Al} - 701.2N_{Si}^3 - 2055.6N_{Si}^2N_{Al} - 1396.0N_{Si}N_{Al}^2$$

$$D_{AlSi} = 110.9N_{Al} + 159.2N_{Al}^2 + 739.1N_{Si}N_{Al} - 359.8N_{Al}^3 - 499.8N_{Si}^2N_{Al} - 521.7N_{Si}N_{Al}^2$$

$$D_{AlAl} = 40.0 + 432.7N_{Al} + 255.0N_{Al}^2 + 159.2N_{Si}N_{Al} - 688.0N_{Al}^3 - 260.8N_{Si}^2N_{Al} - 719.6N_{Si}N_{Al}^2$$

7.2.3 Evaluations for the Ni-1at%Si-4at%Al Alloy and the Ni-Cr-Al-O System

Experimental data are not yet available for interdiffusion coefficients in the Ni-Si-Al system. Therefore, values of the interdiffusion coefficients of the Ni-1 at% Si-4 at% Al alloy at 1073 K were estimated based on previous measurements of self diffusion coefficients and activity coefficients in the ternary alloy system, following the same method of calculations for the Fe-Si-Al system. The self diffusion coefficients of Si and Al in Ni at 1073 K are taken as the experimentally measured values: 4.05×10^{-13} [7.11] and 2.20×10^{-13} [7.12], cm^2/sec, respectively. The activity variations of Si and Al in the Ni-Si-Al system at 1073 K were calculated based on data of binary Ni-Si [7.13], Ni-Al [7.14], and Al-Si [7.15]. Accordingly, the values of interdiffusion coefficients for the Ni-1 at% Si -4 at% Al alloy at 1073 K were obtained as $D_{SiAl} = 4.83 \times 10^{-13}$, $D_{SiSi} = 7.32 \times 10^{-14}$, $D_{AlSi} = 2.52 \times 10^{-13}$, and $D_{AlAl} = 8.26 \times 10^{-13}$, cm^2/sec, respectively. It is interesting to note from these calculations that, unlike the Fe-Si-Al system, the influence of Si additions on the activity and diffusion coefficients of Al in the dilute Ni-Si-Al system is negligible.

Thermodynamic interaction parameters for the Ni-Cr-Al-O system at 1873 K were also estimated using Eq. (2.5-2.8). The thermodynamic properties of relevant binary systems were taken from data of Ref. [7.16] and [7.17]. Obtained values are: $\varepsilon_O^O = 2$, $\varepsilon_O^{Al} = -116$, $\varepsilon_O^{Cr} = -45$, $\varepsilon_{Al}^{Al} = 106$, $\varepsilon_{Cr}^{Cr} = 65$, and $\varepsilon_{Cr}^{Al} = 37$. The estimated values of ε_O^O, ε_O^{Al} and ε_O^{Cr} are consistent with the values experimentally measured by Janke and Fischer [7.18].

7.3. Internal Oxidation Kinetics of Ni-1at%Si-4at%Al Alloys

The following is an attempt to calculate the depths of internal oxidation of the Ni-1at%Si-4at%Al alloys oxidized at 1073 K in either Ni/NiO packs or in 760 torr of oxygen, based on the theoretical considerations described in chapter 4.

For the kinetics of internal oxidation in Ni/NiO packs, as discussed in §4.2.1, there exist two limiting cases to determine the value of the dimensionless parameter γ. These two limiting cases are: (a) $\gamma \ll 1$ and $\gamma(D_O/D_k)^{1/2} \gg 1$; (b) $\gamma \ll 1$ but $\gamma(D_O/D_k)^{1/2} \ll 1$. They also correspond to (a) insignificant diffusion of alloying elements but significant diffusion of oxygen during the internal oxidation process, and (b) significant diffusion of both oxygen and the alloying elements. In order to establish if either limiting case is applicable to the present system, the relevant solubility and diffusivity data must be applied. The mole fraction of oxygen dissolved in Ni at the dissociation of NiO at 1073 K has been experimentally measured as 0.0007 [7.19]. The diffusion coefficient of oxygen in Ni at 1073 K is taken directly from the measurements of Park and Altstetter [7.20] as 5.05×10^{-10} cm^2/sec. Interdiffusion coefficients of the alloy system at 1073 K were estimated in §7.2.3. Substituting these values into Eq. (4.29) (with $x = 0.2$, $y = 2$, and $\nu = 1.5$) one obtains $\gamma \leq 0.064$ and $\gamma(D_O/D_k)^{1/2} \geq 5.79$. Thus, in the Ni–Si–Al alloy system, the first limiting case is valid: the kinetics of internal oxidation is governed by the inward diffusion of dissolved oxygen with insignificant counterdiffusion of Al and Si. Therefore Eq. (4.36) can be applied to calculate the expected depths of internal oxidation of the Ni-1at%Si-4at%Al alloys oxidized at 1073 K in Ni/NiO packs.

The calculated values of depths of internal oxidation are in good

agreement with the experimentally measured values as shown in Table 7.3 and Fig. 7.6. This agreement demonstrates the applicability of the theoretical model in this study to describe the kinetics of exclusive internal oxidation of ternary alloys when oxidation conditions favor simultaneous internal oxidation of the two alloying elements.

The predictions above may suggest that the presence of the internal oxide-denuded Ni nodules or layers on the alloy surface plays a negligible role in the kinetics of internal oxidation of the Ni-1 at% Si-4 at% Al alloys at 1073 K. The formation of internal oxide-free nodules or even layers of the base metal during internal oxidation has been observed in several other alloy systems, such as the oxidation of Ni-Al [7.21], Ag-In [7.22], Pd-Ag-Sn-In [7.23], and in the nitridation of Ni-Cr-Al [7.24] alloys. Preferential grain boundary diffusion or dislocation pipe diffusion has been assumed to account for the transport of base metal atoms to the alloy surface [7.21]. The hypothesis of the dislocation pipe diffusion requires a very high dislocation density in the internal oxidation zone, generating high compressive stresses at the internal oxidation front and within the internal oxidation zone. The transport of the base metal could be caused by the stresses arising from the formation of internal oxides, due to the large molar volume difference between the oxides and the metals. A challenge for researchers in this field is to derive quantitative expressions to describe detailed modes and magnitudes for the formation of the internal oxide-denuded base metals on the alloy surface. In the case of internal oxidation of Ni-Si-Al alloys, the transport of Ni to the alloy surface is thought to be mainly by a mechanism of dislocation pipe diffusion controlled creep. The huge volume increase (~145 vol.%) due to the internal oxidation of Al and Si generates high stress in the Ni lattice.

Table 7.3 Comparison of predicted and experimentally observed depths of internal oxidation of Ni-1at% Si-4at% Al alloys oxidized at 1073 K in Ni/NiO packs

Oxidation time (hours)	Depth (μm)	
	Experimental	Predicted
8	2.60±1.50	4.23
20	5.00±1.80	7.03
48	11.56±1.90	11.99
120	18.59±1.40	18.95
500	38.68±3.17	38.69

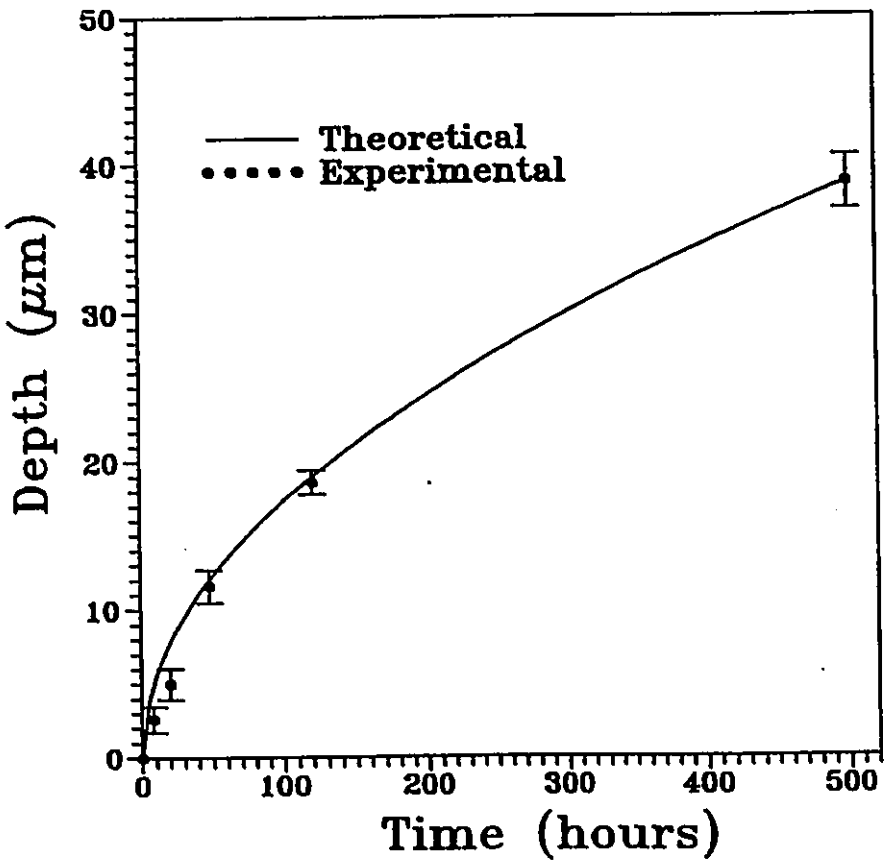

Fig. 7.6 Kinetics of internal oxidation of Ni-1at% Si-4at% Al alloys at 1073 K in Ni/NiO packs

The stress generated results in a dislocation density of about 10^{11} cm^{-2} in the internal oxidation zone. A detailed model for the dislocation density picture is proposed in a paper co-written by this author [7.25].

For Ni-1at%Si-4at%Al alloys oxidized in 760 torr of oxygen, internal oxidation of Al and Si occurs in combination with an external NiO scale. As experimentally observed in this study, the external scale of NiO grows according to a parabolic rate law with the rate constant $k_C \approx 3.83 \times 10^{-13}$ cm^2/sec. If local equilibrium is assumed at the NiO/Ni interface, the oxygen solubility in Ni at the interface may be taken as the value corresponding to the dissociation pressure of NiO. Substituting the solubility and diffusivity data into Eq. (4.51) one obtains $\gamma \leq 0.069$, $(k_C/2D_O)^{1/2} = 0.01$, and $\gamma(D_O/D_k)^{1/2} \geq 6.113$. Thus Eq. (4.52) and Eq. (4.16) can be used to determine the value of the dimensionless parameter γ and then to calculate the expected depth of the internal oxidation zone. The calculated depths of internal oxidation are 10-20% lower than the experimentally observed values, as shown in Table 7.4.

Table 7.4 Comparison of predicted and experimentally observed depths of internal oxidation of Ni-1at% Si-4at% Al alloys oxidized at 1073 K in 760 torr of O_2

Oxidation time (hours)	Depth (μm)	
	Experimental	Predicted
50	18.68±0.76	13.82
120	33.41±1.15	28.23
260	49.56±1.24	41.57
500	64.32±0.50	57.95

There are several possibile explanations for the small deviations from ideal kinetics described by Eq. (4.51) and (4.16). The first is that an oxygen activity corresponding to the coexistence of NiO and Ni may not be maintained in the Ni matrix at the Ni/external NiO scale interface. If the external oxidation is exclusively diffusion controlled, the activity of oxygen at the Ni/NiO scale interface will be affected by the interplay of diffusion processes in the Ni matrix and in the NiO scale. Therefore, when applying the value of the oxygen concentration at the interface in Eq. (4.51), it is necessary to take into account not only the thermodynamic factors but the diffusion factors as well. In addition, mechanical factors (*i.e.*, stress generation and relief around the Ni/NiO scale interface) may also affect the value of interfacial oxygen concentration.

The second possibility is that of vacancy injection into the alloy as a result of forming NiO on the surface. During oxidation in 760 torr of oxygen, the p-type external NiO scale develops and thickens mainly by outward diffusion of Ni^{2+} ions to the scale/gas interface. At the same time, vacancies are injected into the metal at the Ni/NiO interface. If these vacancies diffuse inward and condense at the advancing internal oxidation front, the nucleation and growth of internal oxide precipitates would be enhanced by the relief of compressive stresses induced within the internal oxidation zone. These vacancies might influence nucleation either individually or collectively by grouping into small clusters. However, a detailed mechanism remains to be proposed.

Other explanations have been put forward to interpret the small deviations. In the classic models of internal oxidation of binary alloys and also in this study, it is assumed that the internal oxide precipitates within the internal oxidation zone do not assist or hinder the inward diffusion of oxygen.

Such an assumption may be valid at low alloying concentrations, when a relatively low volume or area fraction of oxide precipitates within the internal oxidation zone is expected. At larger oxide volumes or area fractions, the influence of the morphology or population density of internal oxide precipitates on the diffusivity of oxygen should be considered. The precipitates themselves block the transport of oxygen, while the incoherent regions between the precipitates and the metal matrix may provide enhanced diffusion paths for oxygen [7.21]. Depending on the distribution of the precipitates, the overall effective flux of oxygen may be decreased or increased compared with that expected for lattice transport. For the case of binary alloys, a model which is appropriate for describing the effective oxygen diffusivity within the internal oxidation zone has been advanced by Stott and Wood [7.21]. Nevertheless, under the conditions of the present experiments and theoretical considerations, where bulk concentrations of the alloying elements and oxide volume fraction are relatively small, the effect of enhanced oxygen diffusivity may be neglected. This is indicated by the excellent agreement between predicted and experimentally measured depths of internal oxidation of the alloys oxidized in Ni/NiO packs. Another explanation, suggested by Rapp [7.26] for internal oxidation of Cu-Al alloys, is that nonstoichiometric solute-oxygen clusters may be formed during the internal oxidation. The effect is considered to be particularly important when internal oxidation causes precipitation of very small oxide particles, as with dilute alloys. However, small changes in the stoichiometric ratio, y and v in Eq. (4.51), are found to be insufficient to cause the difference between the calculated and experimentally measured depths of internal oxidation of the alloys oxidized in 760 torr of oxygen, as given in Table 7.4.

7.4. Minimum Al Concentrations for External Al_2O_3 Scale Formation on Ni-Cr-Al Alloys

The criterion for the transition from internal to external oxidation on ternary alloys, developed in §4.4.2, was used to predict the minimum Al bulk concentrations required for the exclusive formation of external Al_2O_3 scales on Ni-Cr-Al alloys at 1373 and 1473 K. Values for the interdiffusion coefficients of the ternary alloy system at both temperatures were taken from the measurements by Nesbitt and Heckel [7.27]. Values of interdiffusion coefficients involving oxygen and alloying elements are usually not available experimentally because of the very low solubility of oxygen in metals and alloys and the strong interaction between oxygen and the alloying elements. However, for dilute alloys these interdiffusion coefficients may be estimated based on the knowledge of tracer or self diffusion coefficients of oxygen and solutes in the base metal as well as thermodynamic interaction parameters of the alloy plus oxygen system (*i.e.*, Eq. (2.4), (2.15) and (2.16)). The values of the tracer or self diffusion coefficient of oxygen in Ni at 1373 and 1473 K are taken as 2.1×10^{-8} and 7.6×10^{-8} [7.21], of Cr in Ni as 1.3×10^{-10} and 3.9×10^{-10} [7.28], and of Al in Ni as 1.0×10^{-10} and 5.0×10^{-10} [7.29], respectively. The values of oxygen solubilities in Ni at the two temperatures were taken from the measurements by Smithells and Ranseley [7.30] and by Seybolt [7.19], and were then modified using Eq. (4.12) to include the effect of Al and Si additions into the ternary alloys. The values of the thermodynamic interaction parameters for the Ni-Cr-Al-O system were taken from either experimental measurements in nickel melts [7.18] or from the theoretical assessment of the system (see §7.2.3). Values for the parabolic rate constants k_c

for the growth of external Al_2O_3 scales on Ni-Cr-Al alloys at 1373 and 1473 K were taken directly from the measurement of Giggens and Pettit [7.31].

At 1473 K, the minimum Al bulk concentrations N_{Al}^{*} predicted from Eq. (4.77) were found to depend on Cr bulk concentrations in the range of 0-35 at% as shown in Fig. 7.7. By increasing the Cr concentration from 0 to about 22 at%, the value of N_{Al}^{*} decreased, whereas further increases in the Cr bulk concentration resulted in an increase of N_{Al}^{*}. The data points in Fig. 7.7 correspond to the compositions of alloys experimentally studied by Giggens and Pettit [7.31]. Open squares and sold circles indicate the alloys that have been found to exhibit internal oxidation of Al and the exclusive external Al_2O_3 scale formation, respectively. Results similar to those above were obtained for the oxidation of Ni-Cr-Al alloys at 1373 K. Fig. 7.8 shows the predicted values of N_{Al}^{*} and the data points from the experimental observations by Giggens and Pettit [7.31]. It is clear from Fig. 7.7 and 7.8 that the predicted values of N_{Al}^{*} agree well with the experimental observations at both temperatures.

The only previous attempt to predict values of N_{Al}^{*} for the formation of exclusive external Al_2O_3 scales on Ni-Cr-Al alloys was made by Nesbitt [7.32]. In his analysis the diffusion of oxygen into the alloys was neglected and only the ternary interdiffusion effect on the Al flux from the alloy to the scale/alloy interface was taken into account. By assuming the mole fraction of Al at the scale/alloy interface to be zero, he predicted the value of N_{Al}^{*} by equating the maximum possible flux of Al with the rate of Al consumption due to the oxidation at the scale/alloy interface. His predicted values of N_{Al}^{*} at 1473 K ranged from 3 to 6 at% for Cr bulk concentrations in the range of 0-40 at%. In this study, Nesbitt's method was used to calculate N_{Al}^{*} for Ni-Cr-Al alloys at 1373 K, and the

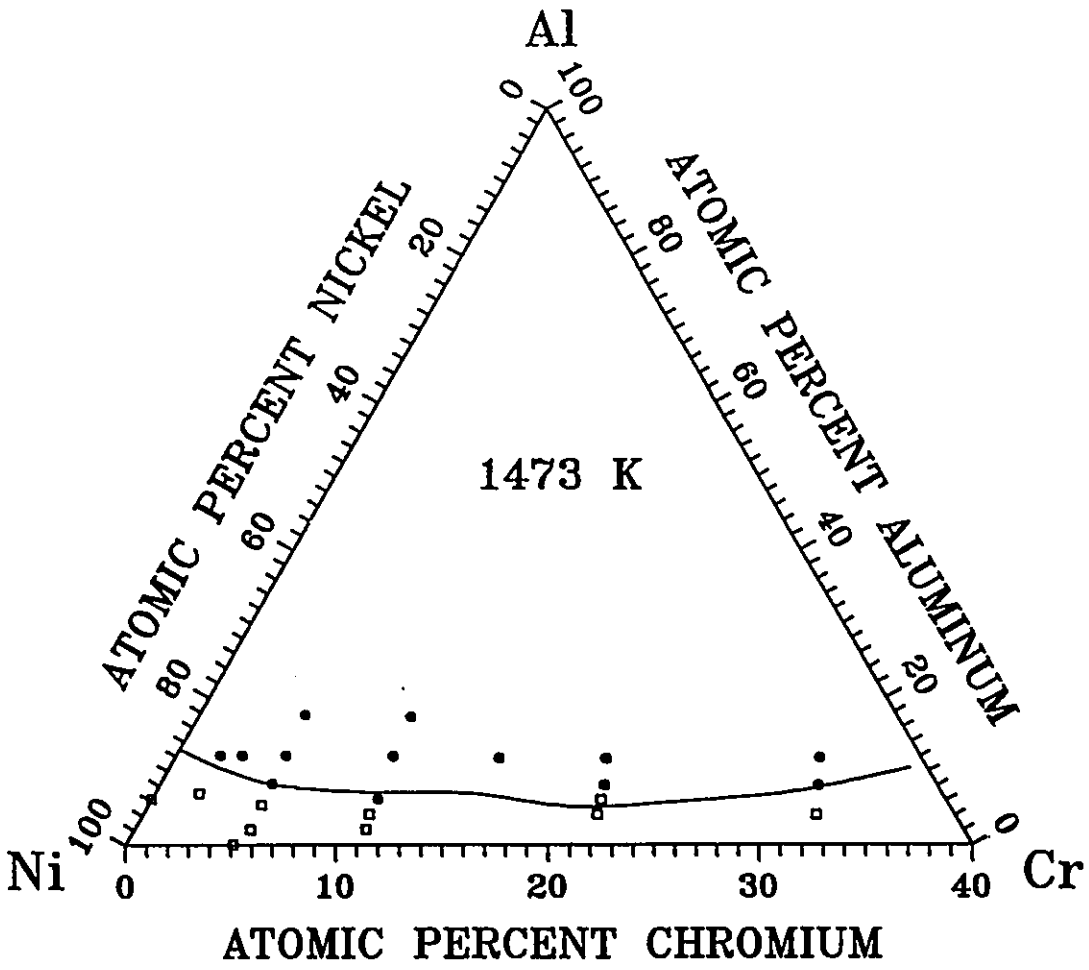

Fig. 7.7 Predicted minimum Al concentrations for Al_2O_3 scale formation on Ni-Cr-Al alloys at 1473 K.

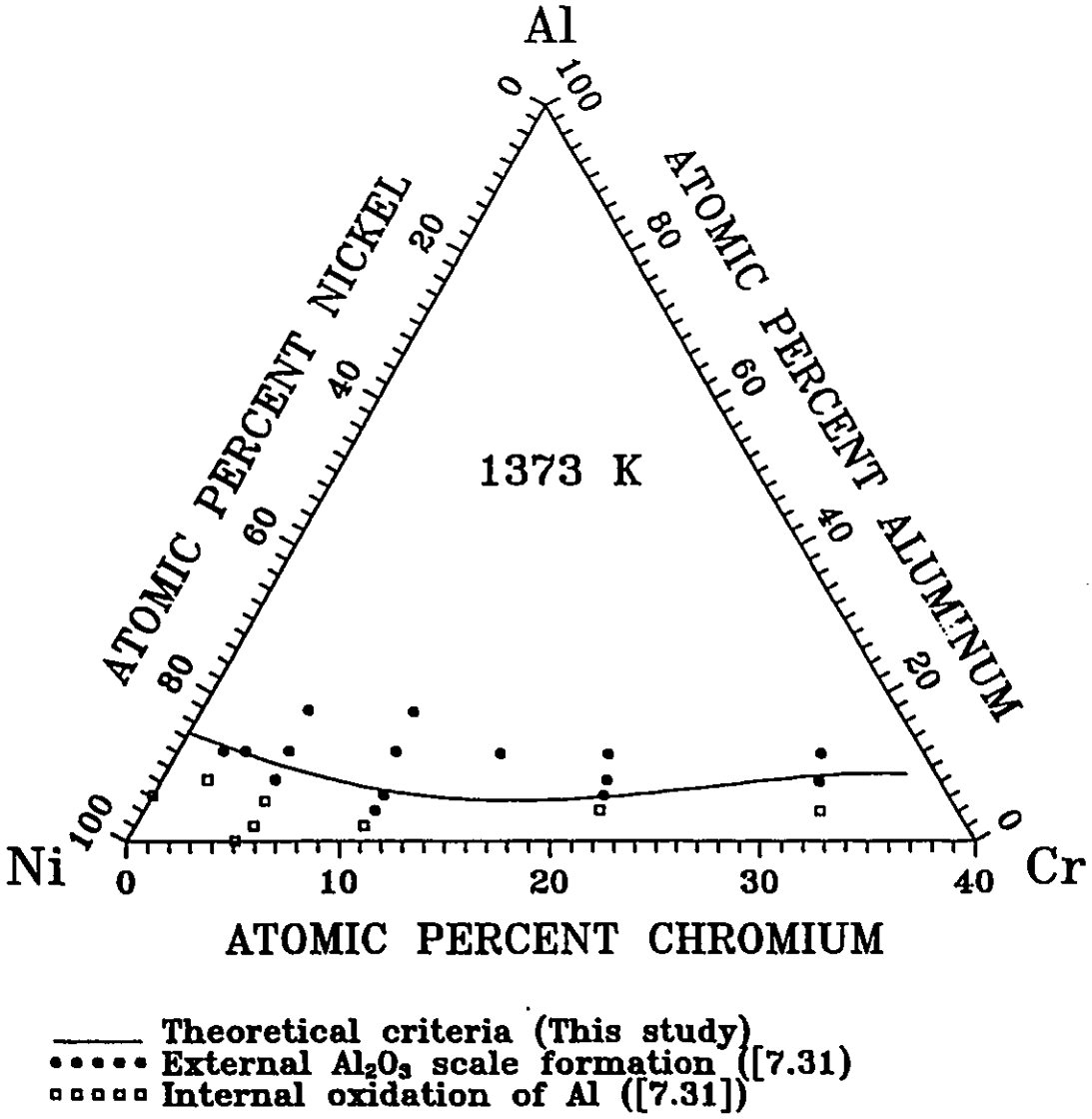

Fig. 7.8 Predicted minimum Al concentrations for Al_2O_3 scale formation on Ni-Cr-Al alloys at 1373 K.

values of N_{Al}^{*} obtained ranged from 2 to 4 at% in the same bulk concentration range of Cr as above. These predicted values of N_{Al}^{*} are similar to those obtained for binary Ni-Al alloys, if the same method is applied. They are much lower than those observed experimentally. The results of Nesbitt's analysis indicate clearly that the beneficial effect of Cr additions on the formation of external scale of Al_2O_3 cannot be accounted for by the ternary interdiffusion effect. Because the ternary diffusion coefficients affecting the diffusion of Al in dilute Ni-Cr-Al alloys (D_{AlAl} and D_{AlCr}, [7.27]) and the parabolic rate constants for external Al_2O_3 scale growth [7.31] are not significantly affected by Cr concentration, the diffusion flux of Al in the alloy to the scale/alloy interface will not be significantly affected by Cr addition either. In fact, one may calculate the flux of Al to the scale/alloy interface using Eq. (4.64) or Eq. (4.82). As shown in Fig. 7.9, the difference between the Al flux to the scale/alloy interface of a Ni-10at% Cr-8at% Al alloy and that of a Ni-8at% Al alloy is very small.

According to Wagner's hypothesis for the gettering effect in the oxidation of ternary alloys [7.33], one may assume that the Cr acts as an oxygen getter, preventing internal oxidation of Al. During the very early stage of oxidation, oxides of Ni, Cr and Al, are all formed. If sufficient Cr is present in the alloy, the initially formed NiO will be reduced by Cr through the reaction

$$3NiO + 2Cr \text{ (in alloy)} = Ni \text{ (in alloy)} + Cr_2O_3 \qquad (7.9)$$

In this manner a continuous layer of Cr_2O_3 could be formed in the alloy, and this would reduce the oxygen activity to such a low level that Al in the alloy could now be selectively oxidized to build up a continuous Al_2O_3 scale. However, it has

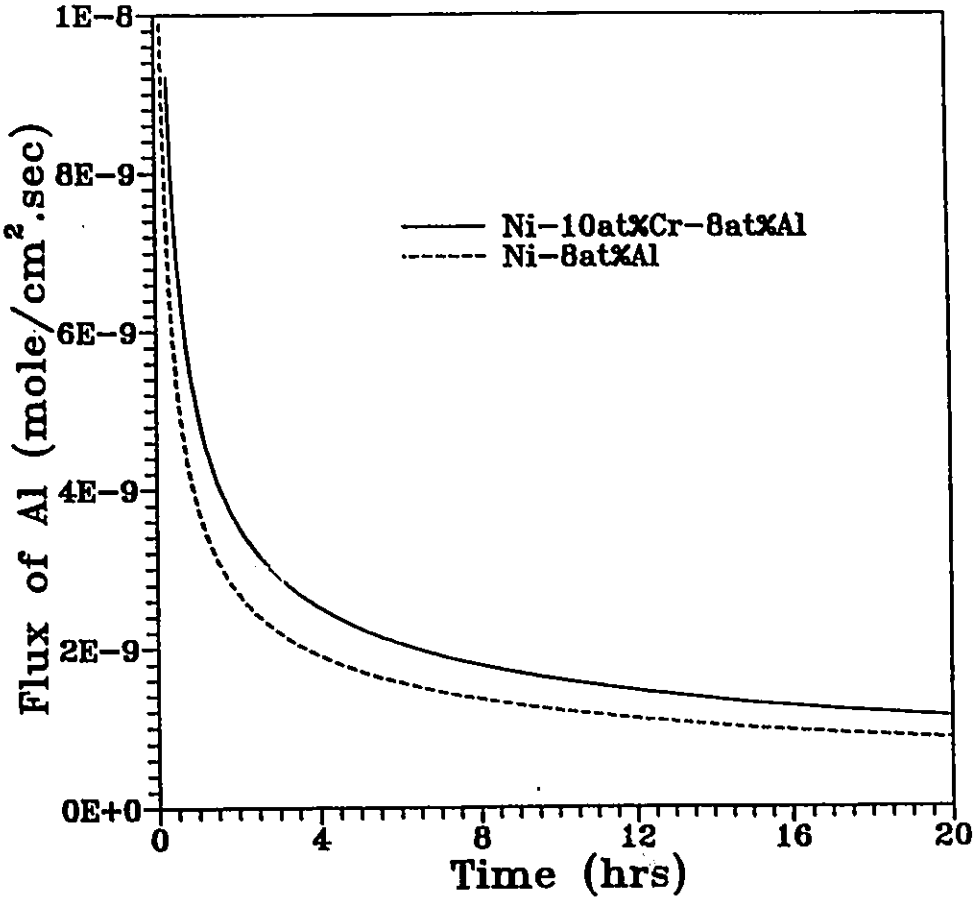

Fig. 7.9 The Al flux to the scale/alloy interface from Ni-8 at% Al alloys with or without Cr additions at 1473 K

been found experimentally [7.31, 7.34-38] that the amount of Cr required to act as a getter in Ni-Cr-Al alloys, would not be sufficient to form a continuous Cr_2O_3 external scale in the absence of Al. For instance, Giggens and Pettit [7.31] found that in order to form an external Al_2O_3 scale on Ni-Cr-Al alloys containing 8 at% Al at 1473 K, the minimum Cr bulk concentration would be 5 at%. On the other hand, it was found that at 1473 K, continuous Cr_2O_3 external scales form only on binary Ni-Cr alloys with more than approximately 20 at% Cr [7.39]. Obviously, it is necessary to reconsider the role of Cr as a secondary getter. Using the oxygen solubility model developed in §4.2, it is possible to quantitatively determine the oxygen solubility behavior in the Ni-Cr-Al alloys as a function of Cr and Al concentrations. When $N_{Al} = 0.08$, the dependence of the oxygen solubility on Cr concentrations at 1473 K was obtained using Eq. (4.12), as shown in Fig. 7.10. Because of thermodynamic interactions, the addition of Cr up to 0.05 mole fraction can reduce the oxygen solubility in the alloys dramatically, whereas the gradient of the decrease with larger Cr concentrations is very small. This suggests that the gettering effect of Cr does not necessarily require a Cr concentration high enough to establish a continuous Cr_2O_3 external scale.

At a fixed Cr concentration, the dependence of the oxygen solubility in Ni-Cr-Al alloys on the Al concentration at 1473 K was calculated using Eq. (4.13), as shown in Fig. 7.11. The gradient of the change has large negative values at small Al concentrations, but it is almost constant (~0.011) at N_{Al} larger than 0.02. It is interesting that, although the addition of Cr into the ternary alloys will reduce the oxygen solubility in the alloys, it does not significantly affect the dependence of the oxygen solubility on N_{Al}.

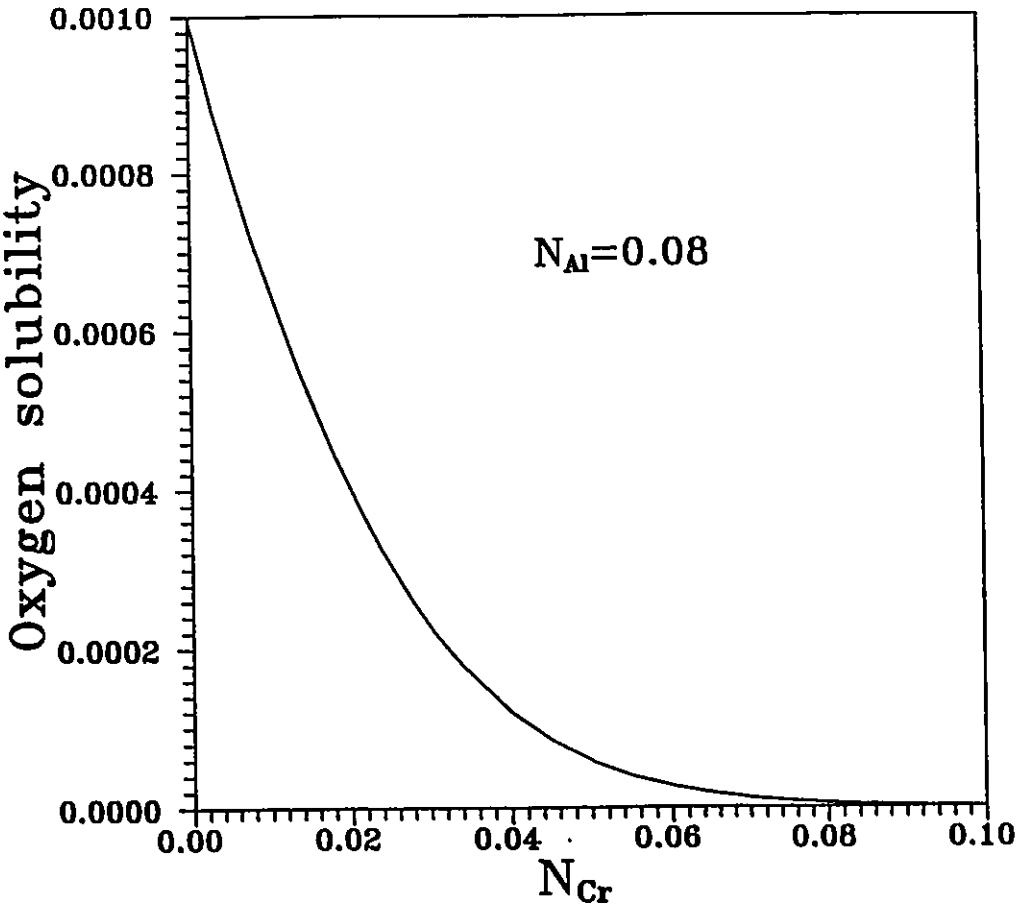

Fig. 7.10 Oxygen solubility in the Ni-Cr-Al alloys as a function of Cr concentration at 1473 K.

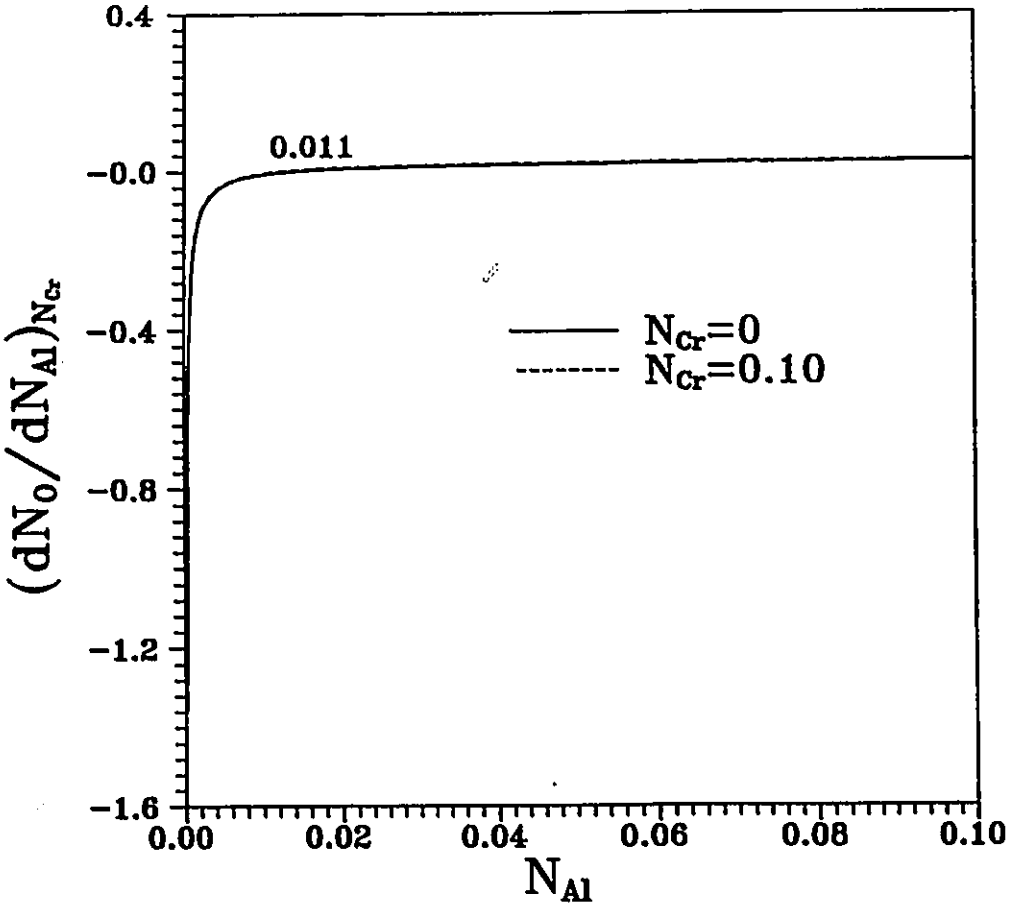

Fig. 7.11 The dependence of oxygen solubility in Ni-Cr-Al alloys on Al concentrations at 1473 K

The ternary extension (§4.4.2) of Wagner's criterion for the presence or absence of internal oxidation is essentially based on the activity gradients of metal and oxygen and their relationships to oxygen supersaturation in the alloys. In the case of binary alloys, Smeltzer and Whittle [7.40] have demonstrated that Wagner's criterion is equivalent to the relationship between the diffusional composition path and the oxygen solubility curve in the alloy-oxygen isotherm. The distributions of oxygen and the solute elements are not independent of each other but are interrelated. Because its concentration is small, the influence of oxygen on the distribution of solute elements may be neglected. However, the distribution of the solute elements should have a very significant effect on the oxygen distribution, especially where there is strong thermodynamic interaction. Accordingly, the diffusion of oxygen in the Ni-Cr-Al alloys will be dependent not only on its own concentration gradient but also on the gradients of Cr and Al. It is also expected that the Cr addition will have an influence on the slope of the virtual diffusion path on the alloy side of the scale/alloy interface, $(dN_O/dN_{Al})_{DP}$. According to Eq. (4.63) and (4.76), we have

$$\left(\frac{d\,N_O}{d\,N_{Al}}\right)_{DP} = \left(\frac{\partial\,N_O}{\partial\,x} \Big/ \frac{d\,N_{Al}}{d\,x}\right)_{x=\xi} = \frac{\sum_{k=1}^{3} \theta_{1k} F_k}{\sum_{k=1}^{3} \theta_{2k} F_k} \qquad (7.10)$$

where 1 and 2 refer to oxygen and Al, respectively. As shown in Fig. 7.12, the slope of the diffusion path decreases significantly with increasing Cr bulk concentrations in the Ni-Cr-Al alloys containing 8 at% Al at 1473 K. Referring to Fig. 7.11 and Fig. 7.12, it can be seen that in order to force the diffusion path to contact the tangent of the oxygen solubility surface, the Cr bulk concentration

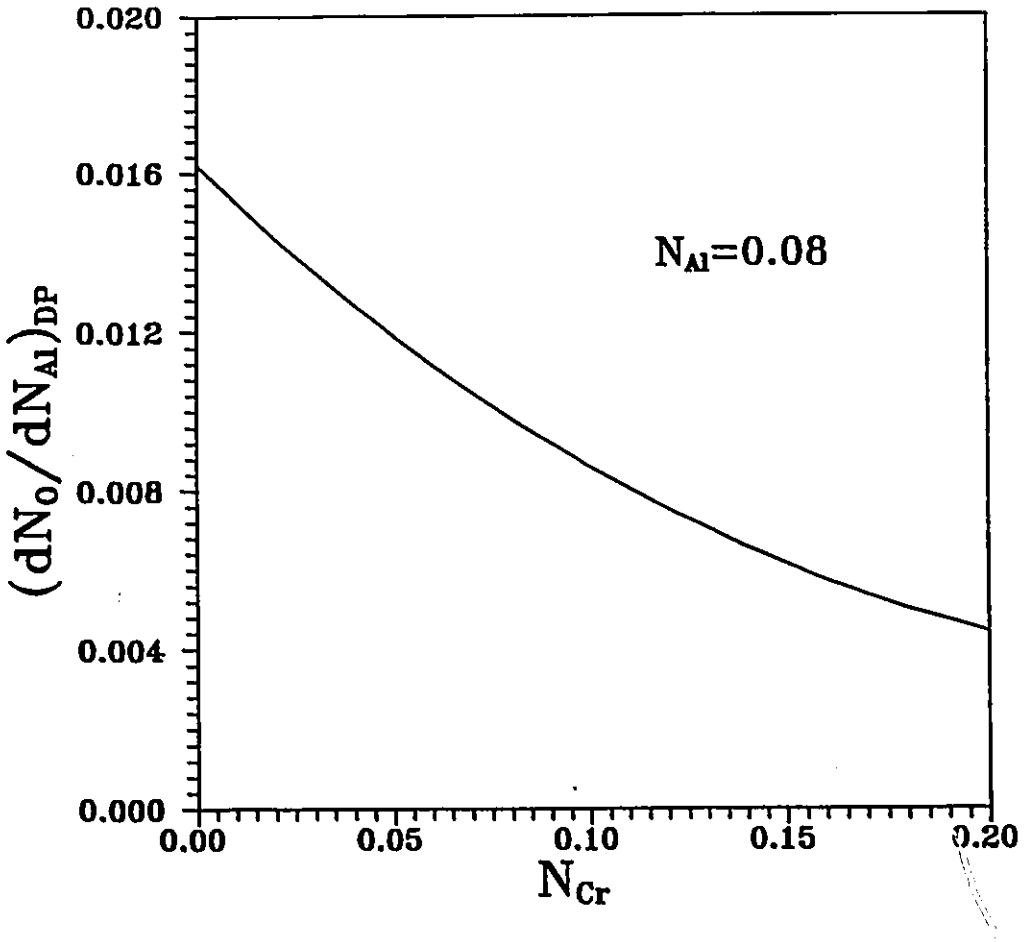

Fig. 7.12 The change of the slope of the diffusion path at the scale/alloy interface as a function of Cr concentration at 1473 K

in the alloys has to be not less than 5 at%. In this manner the slope of the diffusion path will be equal to or smaller than the gradient of the oxygen solubility surface (0.011). Therefore, the diffusion path will not lead to oxygen supersaturation and internal oxide precipitation. This effect of the Cr addition may be seen more clearly from Eq. (4.77). Letting all interaction parameters be zero in Eq. (4.77), one obtains the criterion for exclusive external scale formation as

$$N_2^O \geq f(r,k) - \frac{N_1^i}{\nu} \frac{\sum_{k=1}^{3} \theta_{2k} F_k}{\sum_{k=1}^{3} \theta_{1k} F_k} \tag{7.11}$$

Then Fig. 7.12 implies that the minimum Al bulk concentration required for the fromation of an exclusive Al_2O_3 external scale should decrease with increasing Cr bulk concentrations in the Ni-Cr-Al alloys. The gettering effect of Cr on the minimum Al concentration may not be seen distinctly from Eq. (7.11) because the oxygen interfacial concentration (N_1^i) is also included in F_k terms.

It is thus apparent that the beneficial effect of Cr addition on the oxidation of Ni-Cr-Al alloys can be attributed to that through thermodynamic interactions: (*i*) a sufficient Cr addition reduces the oxygen solubility in the alloys; and (*ii*) a sufficient Cr addition also alters the oxygen distribution in the ternary alloys, detering the oxygen supersaturation necessary for the onset of internal oxidation in the alloys. These two factors make it easier to establish a continuous Al_2O_3 external scale on ternary Ni-Cr-Al alloys.

The need to use thermodynamic interaction parameters from the molten state for the calculations in this study introduces some uncertainty. However, it can be

shown that the absolute values of these interaction parameters would increase by less than a factor of two if the temperature is extrapolated from the state of melt (*i.e.*, 1873 K) to 1473 or 1373 K, and this temperature effect would only cause changes in the predicted values of the minimum Al for the exclusive Al_2O_3 external scale formation of less than 1.5 at%. Some uncertainty may also arise from the use of the Wagner formalism for activity coefficients in Ni-Cr-Al alloys containing concentrations of Al as high as 16 at% and of Cr as high as 30 at%. This use may be justified by the following facts: (*i*) the activity of Cr in Ni-Cr alloys shows only a slight deviation from ideality below 25 at% Cr over the temperature range of 1200-1600 K [7.41]; (*ii*) Al activity corresponds to Henrian solution behavior below 17 at% Al in Ni-Al alloys between 900 and 1400 K [7.42]; and (*iii*) the deviation of Al activity from ideality decreases on passing from the Ni-Al binary system to the ternary Ni-Cr-Al system, and the effect of the addition of Cr on the activity of Al is small in ternary Ni-Cr-Al alloys [7.43].

7.5 Oxidation of Fe-Si-Al Alloys

7.5.1 Oxidation Characteristics of Binary and Ternary Fe-Si-Al Alloys

Table 7.5 records values of the parabolic rate constants determined from the oxidation curves in Fig. 6.1 and Table 6.1, for long exposure intervals in 0.04-0.07 torr and 760 torr of oxygen at 1073 K. It shows that the three ternary Fe-Si-Al alloys were 100~1000 times more oxidation resistant than the binary Fe-6Al alloys. In particular, the Fe-6Si-5Al alloy had a typical oxidation rate

Table 7.5 Measured parabolic rate constant in oxygen at 1073 K

Alloy	Pressure (torr)	k_p ($g^2 \cdot cm^{-4} \cdot sec^{-1}$)	Reference
Pure Fe	760	5.3×10^{-8}	[7.44]
Fe-16Al	200	4.0×10^{-14}	[7.45]
Fe-22Al	100	5.0×10^{-15}	[7.46]
Fe-6Al(24 hrs)	0.04-0.07	$(2.40\pm0.08)\times10^{-12}$	this study
Fe-6Al(200 hrs)	760	$(7.48\pm0.01)\times10^{-11}$	this study
Fe-6Al(500 hrs)	760	$(8.96\pm0.07)\times10^{-11}$	this study
Fe-6Si(24 hrs)	0.04-0.07	$(1.20\pm0.01)\times10^{-14}$	this study
Fe-6Si(200 hrs)	760	$(3.25\pm0.01)\times10^{-12}$	this study
Fe-6Si(500 hrs)	760	$(3.50\pm0.01)\times10^{-12}$	this study
Fe-6Si-1Al(24 hrs)	0.04-0.07	$(1.00\pm0.02)\times10^{-14}$	this study
Fe-6Si-1Al(200 hrs)	760	$(6.28\pm0.01)\times10^{-14}$	this study
Fe-6Si-1Al(500 hrs)	760	$(8.13\pm0.02)\times10^{-14}$	this study
Fe-6Si-3Al(24 hrs)	0.04-0.07	$(1.01\sim3.02\pm0.03)\times10^{-14}$	this study
Fe-6Si-3Al(200 hrs)	760	$(1.21\pm0.17)\times10^{-14}$	this study
Fe-6Si-3Al(500 hrs)	760	$(2.43\pm0.02)\times10^{-14}$	this study
Fe-6Si-5Al(24 hrs)	0.04-0.07	$(7.60\pm0.04)\times10^{-15}$	this study
Fe-6Si-5Al(200 hrs)	760	$(4.14\pm0.02)\times10^{-15}$	this study
Fe-6Si-5Al(500 hrs)	760	$(9.23\pm0.01)\times10^{-15}$	this study

which was comparable to that of an Fe-22Al alloy in 100 torr of oxygen at the same temperature.

As shown in Fig. 6.1, initially the Fe-6Al alloys exhibited a relatively slow oxidation rate, after which the oxidation rate increased significantly. Morphologies of the oxide formed are shown in Fig. 6.2. Sample surfaces were almost covered by a multilayered oxide scale which was composed of Fe_2O_3, Fe_3O_4,

and $FeAl_2O_4/Al_2O_3$. At long reaction times (200 and 500 hours), the multilayered scale contained only layers of Fe_2O_3 and Al_2O_3. There were some regions at the sample surface not fully covered by the multilayered oxide scale, as shown in Fig. 6.2 (a). These regions were Al rich, as indicated by EDAX analyses. At 1073 K, alloys of this composition are classified as Al_2O_3 formers as a transition occurs from internal to external oxidation [7.47]. The scales formed at this Al composition, however, are not fully protective and permit the development of bulky nodular growths of iron oxides. In the initial stages of oxidation, nuclei of Al_2O_3 and FeO form at the alloy surface. However, the Al_2O_3 soon forms a continuous layer, isolating most of the FeO grains from the alloy which becomes depleted in Al. This is consistent with the initial slow oxidation rate shown in Fig. 6.1. Physical flaws or discontinuities in the the Al_2O_3 layer act as rapid diffusion channels which permit the passage of oxygen. This enables a few of the FeO grains to continue growing. As the underlying substrate has been depleted in Al during the initial scale-forming stage, the Fe-enriched alloy then oxidizes locally to form nodules around the FeO grains. During its growth, a typical nodule has an outer shell of Fe_2O_3 with a porous interior containing Fe_3O_4 and $FeAl_2O_4$. Some FeO may still remain at the base of nodules but it readily reacts with Al_2O_3 to form $FeAl_2O_4$. There is a build up of Al-rich phases at the base of the nodules. But because the Al content in the alloy is low, an aluminum oxide healing layer is not able to develop at the base of the nodules. Therefore, the Fe oxide nodules will coalesce to develop a bulky stratified scale composed of Fe_2O_3 and Fe_3O_4 with an inner layer of Al_2O_3. This is reflected by the increase in the oxidation rate shown in Fig. 6.1. After 200 or 500 hours of oxidation, the Fe_3O_4 layer disappears by reaction with oxygen or Al_2O_3. The observed morphologies of scales formed on

the Fe-6Al alloys in this study are consistent with those obtained by Tomaszewicz and Wallwork [7.48].

The oxidation kinetics of the Fe-6Si alloys in 0.04-0.07 torr of oxygen are characterized by an initially rapid oxidation rate, followed by a second, much slower rate, on the order of 1.2×10^{-14} $g^2 \cdot cm^{-4} \cdot sec^{-1}$. EDAX, Auger survey and TEM analyses of the oxide formed indicated a duplex morphology, with an outer Fe_2O_3 layer and an inner SiO_2 layer. The mechanism for the oxide formation appears to be similar to that proposed by Wagner [7.49], and is schematically illustrated in Fig. 7.13. At the initial stage of oxidation, both FeO and SiO_2 are nucleated at the sample surface (Fig. 7.13(a)). As FeO grows much faster then SiO_2, it soon overgrows the SiO_2 and interdiffusion leads to the establishment of Fe_2SiO_4 (Fig. 7.13(b)). As oxidation is continued, Fe_3O_4 and Fe_2O_3 form as external layers and a fine dispersion of Fe_2SiO_4 and SiO_2 is established near the oxide/alloy interface (Fig. 7.13(c)). The Fe_2SiO_4 may then disappear gradually while at the same time the formation of SiO_2 becomes predominant. SiO_2 formation can be attributed to increased mobility of Si^{4+} ions which are preferentially oxidized in the vicinity of the oxide/alloy interface. SiO_2 can also be generated from Fe_2SiO_4 by solid displacement reactions. Thus a continuous layer of SiO_2 is established at the oxide/alloy interface, leading to a reduction in the rate of oxidation by blocking the outward diffusion of Fe^{2+} cations as seen in Fig. 6.1. This results in further reaction of the Fe_3O_4 layer with oxygen or SiO_2. Eventually the oxide scale becomes duplex in nature, with an outer layer of Fe_2O_3 and an inner layer of SiO_2 (Fig. 7.13(d)). FeO is seldom detected in oxidation products since it cannot exist in equilibrium with SiO_2, as is demonstrated in the oxygen pressure-composition equilibrium diagram (Fig. 7.2) obtained in §7.1. Tomaszewicz and Wallwork [7.48]

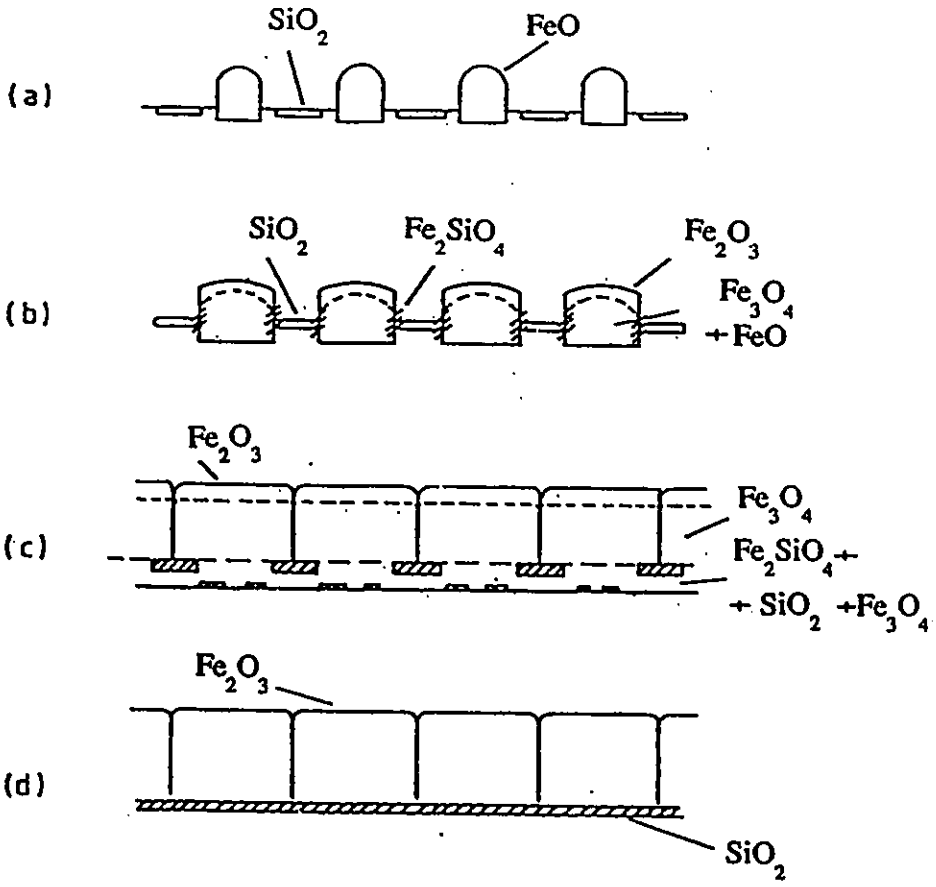

Fig. 7.13 A schematic representation for the progressive oxidation of Fe-6Si and the formation of a duplex Fe_2O_3/SiO_2 scale.

have shown that a similar pattern of a duplex scale of Fe_2O_3/Al_2O_3 is found on Fe-5at%Al alloys.

The increased oxidation rate of the Fe-6Si alloys in 760 torr of oxygen for periods of 200 and 500 hours may be due to the enhanced outward permeation of Fe through the slowly growing SiO_2 inner layer. Significant transport through SiO_2 of a metallic element with an oxide less stable than SiO_2 has been reported previously for the oxidation of Cu-Si [7.50] and Ni-Si [7.51] alloys. In the case of Fe-Si alloys, Adachi and Meier [7.52] have shown that SiO_2 is permeable to Fe and that the permeation is more rapid at higher pressures of oxygen. The transport of Fe through the SiO_2 layer results in the significant contribution of Fe_2O_3 growth to the overall weight change. A second mode contributing to the higher oxidation rate of the Fe-6Si alloys in 760 torr of oxygen is growth of extensive Fe oxide nodules. The nodules tend to be formed at highly stressed areas such as specimen edges and corners, or at regions of crystal misfit such as grain boundaries or triple points. A typical oxide nodule is shown in Fig. 6.3(d), containing SiO_2/Fe_2SiO_4 + Fe_3O_4/Fe_2O_3 phases. The higher oxidation rate can be explained if some of the nodules did not develop a complete SiO_2 healing layer at the base of the nodules. The continued growth of such nodules is associated with an increase in overall weight change.

The ternary Fe-6Si-1Al, Fe-6Si-3Al, and Fe-6Si-5Al alloys exhibited slow parabolic oxidation rates and formed a convoluted oxide scale which is composed of predominantly α-Al_2O_3 covered by α-Fe_2O_3 segments. Such oxidation characteristics are generally expected in binary Fe-Al alloys containing a very high content of Al. The ternary alloy containing only 0.88 at% Al formed a very protective α-Al_2O_3 film, with an oxidation resistance comparable to that of Fe-16Al. It is clearly

shown from this study that in combination with Si, the Al content required to form a protective Al_2O_3 scale is significantly lower than that for binary Fe-Al alloys. The synergistic effect of Al and Si in the oxidation of Fe-Si-Al alloys will now be considered.

7.5.2. Synergistic Effect in Fe-Si-Al Alloy Oxidation

Oxidation properties of ternary Fe-Si-Al alloys containing up to 15 at% Al and 5 at% Si were studied by Boggs [7.53] in 700 torr of wet and dry oxygen and in flowing air for 50 hours over the temperature range of 1073-1366 K. His study contained only limited compositional identification of the oxide formed. The adherent protective oxide was identified by X-ray diffraction as α-Al_2O_3. The Si content in the protective oxide formed on an Fe-2Si-11Al alloy, which had the best oxidation resistance of all the ternary alloys examined, was found to be less than 0.01%. Boggs speculated that the role of Si in the ternary alloys is to act as a getter for oxygen, preventing inward diffusion of oxygen into the alloy when a break occurs in the primary protective Al_2O_3. This prevents the internal precipitation of Al_2O_3 that prevents the healing of the primary protective film. It also suppresses the formation of the iron oxide nodules that tend to destroy binary Fe-Al alloys during oxidation. In this study, TEM and Auger analyses indicated that SiO_2 existed at the surface only at the very early stage of oxidation, while Si was not detected or was under the detectable limit in the oxides formed after longer times of oxidation. SIMS profiles of the oxide formed suggested that the Si amount in the oxide was less than 0.1 at%. Some Si enrichment was found at the oxide/alloy interface after long exposure time, but

there is no evidence showing the formation of SiO_2 there. In the oxidation of Fe-6Si-3Al alloys in 0.04-0.07 torr of oxygen, some voids were found at the oxide surface as shown in Fig. 6.16 (c). At the base of these voids, Si was not detected, although some Al enrichment was observed. The above results suggest that Si can limit the oxidation of Fe by forming SiO_2 during the transient stage of oxidation before the onset of parabolic kinetics governing growth of the protective Al_2O_3 film. In light of the greatly enhanced oxidation resistance, however, it is questionable whether the gettering effect of Si for oxygen can be considered as the sole mechanism leading to oxidation resistance.

Using the oxygen solubility theory developed in §4.2, one can try to quantitatively describe the oxygen solubility behavior in the ternary Fe-Si-Al alloy beneath Al_2O_3 scale as a function of alloy compositions. Oxygen solubility in solid α-Fe is very small with only 0.0024 at% at both 923 and 1153 K [7.54]. To a first approximation, the following thermodynamic interaction coefficients may be taken from a compilation by Sigworth and Elliott [7.55] for Fe melts at 1873 K: $\varepsilon_O^{Al} = -433$, $\varepsilon_O^{Si} = -15.0$, and $\varepsilon_O^{O} = -12.5$; Values of the interaction coefficients ε_{Al}^{Al}, ε_{Si}^{Si}, and ε_{Si}^{Al} at 1073 K were calcuated from Eq. (7.7) and (7.8) as 2.54, 5.01, and 14.32, respectively. When the Al mole fraction in the alloy was fixed as 0.01, the dependence of the oxygen solubility on the Si concentration was obtained using Eq. (4.12), as shown in Fig. 7.14. The result demonstrates that, unlike the gettering effect of Cr in Ni-Cr-Al alloys (Fig. 7.10), Si addition cannot significantly reduce the oxygen solubility in the Fe-Si-Al alloys in equilibrium with the Al_2O_3 scale.

There is a shortage of experimental results on the thermodynamic and diffusional data of Fe-Si-Al alloys. The addition of 1 at% Si to an Fe-1at%Al

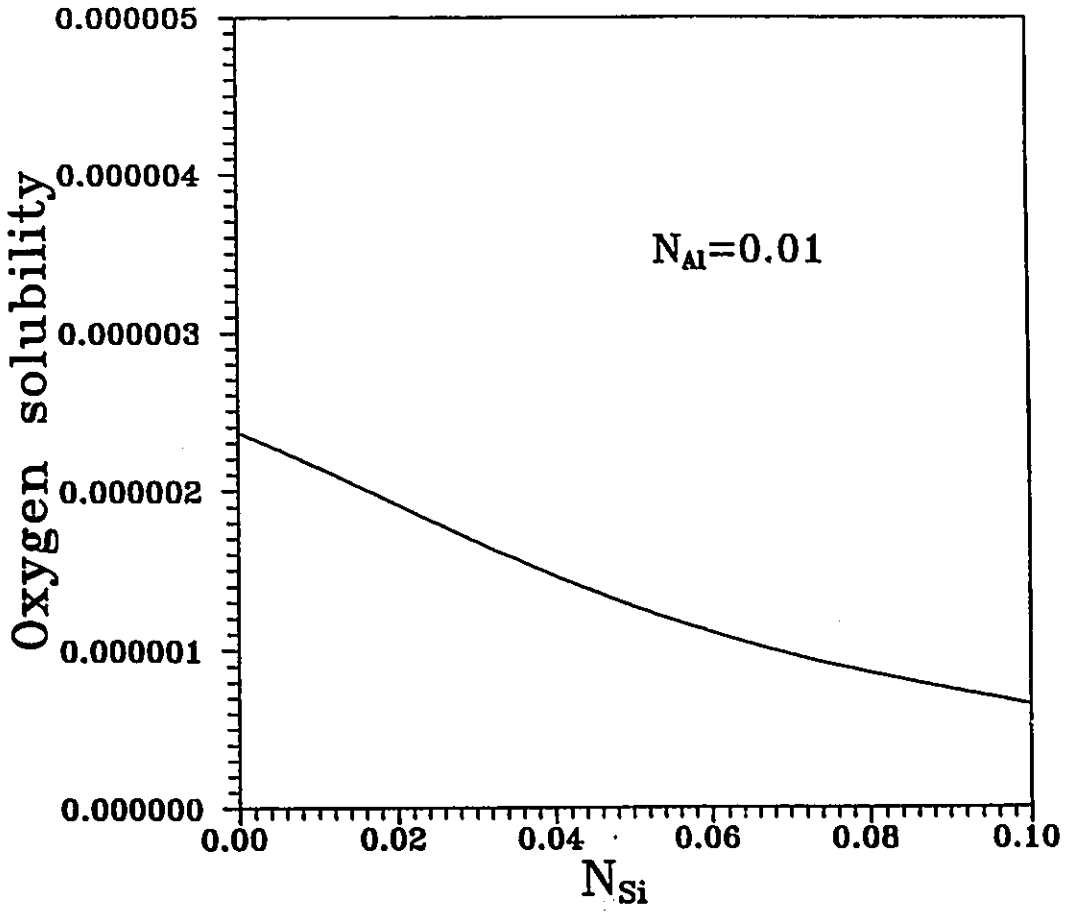

Fig. 7.14 Oxygen solubility in the Fe-Si-Al alloys as a function of Si concentration at 1073 K.

alloy was observed to increase the activity of Al in the alloy up to 6 times at 1823 K [7.8]. At 1273 K, the range of solid solubility of α-Fe in the Fe-Si-Al system can reach up to 20 wt% Si and 35 wt% Al [7.56], as seen in Fig. 3.4. These facts indicate strongly there are large repulsive alloying interactions in the Fe-Si-Al system. Thus the synergistic beneficial effect of Si and Al additions on the oxidation resistance of the Fe-Si-Al alloys may be associated with the large interactions, increasing the Al activity (Fig. 7.4) and outward diffusion flux of Al to the oxide/alloy interface. This decreases the critical Al concentration required to form a protective Al_2O_3.

In the case of oxidation of A-B binary alloys, for a high concentration of B one can assume that only B is oxidized to form an external oxide scale and no internal oxidation occurs. The oxidation rate will thus depend on the diffusion processes, and the maximum flux of B from the alloy to the oxide/alloy interface, J_B^*, would be given at a given time t by [7.57]

$$J_B^* = \frac{1}{V_a} N_B^o \left[\frac{\tilde{D}}{\pi t}\right]^{1/2} \tag{7.12}$$

where $\tilde{D}$ is the chemical diffusivity of B in the alloy, V_a is the molar volume of the alloy, and N_B^o is the bulk mole fraction of B. An attempt to calculate the maximum flux of B in both cases of A-B binary alloys and A-B-C ternary alloys was made for the Fe-Si-Al system at 1073 K according to Eq. (7.12) and (4.85). The data of chemical diffusivities in Fe-Al alloys were taken from the measurement by Nishida *et al.* [7.9]. Values of interdiffusion coefficients of the Fe-Si-Al system were taken from Table 7.2. The calculated results of the maximum flux of Al at

Table 7.6 The Al flux to the oxide/alloy interface from binary or ternary Fe-Si-Al alloys at oxidation times up to 24 hours at 1073 K

Alloy	Ternary Al flux J_{Al}, mole·cm^{-2}·sec^{-1}	Binary Al flux J^{*}_{Al}, mole·cm^{-2}·sec^{-1}	J_{Al}/J^{*}_{Al}
Fe-6Si-1Al	8.47×10^{-11}	5.40×10^{-12}	15.7
Fe-6Si-3Al	1.54×10^{-10}	2.03×10^{-11}	7.58
Fe-6Si-5Al	2.98×10^{-10}	3.82×10^{-11}	7.80
Fe-11Al		8.90×10^{-11}	
Fe-20Al		3.00×10^{-10}	

oxidation time up to 24 hours are listed in Table 7.6. These numbers show that, for the Fe-6Si-1Al ternary alloy, the flux of Al to the oxide/alloy interface is as large as 16 times that of the Fe-1Al alloy. The flux of Al in the Fe-6Si-5Al alloy is as large as 8 times that of the Fe-5Al alloy, and is comparable to the flux of an Fe-Al binary alloy containing 20 at% Al. Certainly, the greatly enhanced Al flux from the alloy to the oxide/alloy interface would facilitate the establishment of a protective Al_2O_3 scale on the ternary alloys.

Attempts were made to apply the criterion from the analysis in §4.4.2 to predict the minimum Al concentration required to form a protective Al_2O_3 scale on ternary Fe-Si-Al alloys containing 6 at% Si. For Fe-(1~5)at%Al-6at%Si alloys at 1073 K, average values of interdiffusion diffusion coefficients can be obtained from Table 7.3 as $D_{AlAl} = 3.35 \times 10^{-11}$, $D_{AlSi} = 2.96 \times 10^{-12}$, $D_{SiSi} = 9.95 \times$

10^{-12}, and D_{SiAl} = -9.47 × 10^{-13} cm^2/sec. Values of the interdiffusion coefficients involving oxygen and the two alloying elements may be estimated based on the knowledge of self diffusion of oxygen in Fe, the solubility of oxygen in the ternary alloy beneath Al_2O_3 scale, and the thermodynamic interaction parameters (*i.e.*, Eq.(2.4), (2.15), and (2.16)). The value of the self diffusion of oxygen in Fe was taken from Takada and coworkers [7.58] as 1.23 × 10^{-7} cm^2/sec. The average value of the oxygen solubility in the ternary alloys beneath the Al_2O_3 scale was calculated to be 0.0011 at% at 1073 K by applying Eq. (4.12) (The thermodynamic interaction parameters were given previously). From these data, the following interdiffusion coefficients at 1073 K were obtained: D_{OO} = 1.20 × 10^{-7}, D_{OAl} = -5.90 × 10^{-9}, D_{OSi} = -2.0 × 10^{-10}, D_{AlO} = -3.34 × 10^{-10}, and D_{SiO} = -5.90 × 10^{-11} cm^2/sec. The average value of the parabolic oxidation rate constant of the ternary alloys at 1073 K in 0.04-0.07 torr of oxygen can be taken as 1 × 10^{-14} $g^2 \cdot cm^{-4} \cdot sec^{-1}$, from previous calculations in this study. Using Eq. (4.77), the minimum Al concentration, above which no internal oxidation occurs and an external Al_2O_3 scale forms on the Fe-Si-Al alloys containing 6 at% Si, is calculated to be 0.67 at%.

The ternary Fe-Si-Al alloys formed a convoluted oxide scale which is composed of predominantly α-Al_2O_3 scale partially covered by α-Fe_2O_3 segments. The mechanism for the development of the oxide scale is described schematically in Fig. 7.15. The initial stages of oxidation are characterized by the formation of nuclei of FeO, SiO_2 and Al_2O_3 (Fig. 7.15(a)). Because of strong alloying interactions in the ternary Fe-Si-Al system, the concentration of Al is sufficient for Al_2O_3 grains to cover the alloy surface completely and FeO and SiO_2 only remain at randomly located sites. Grains of FeO and SiO_2 eventually become

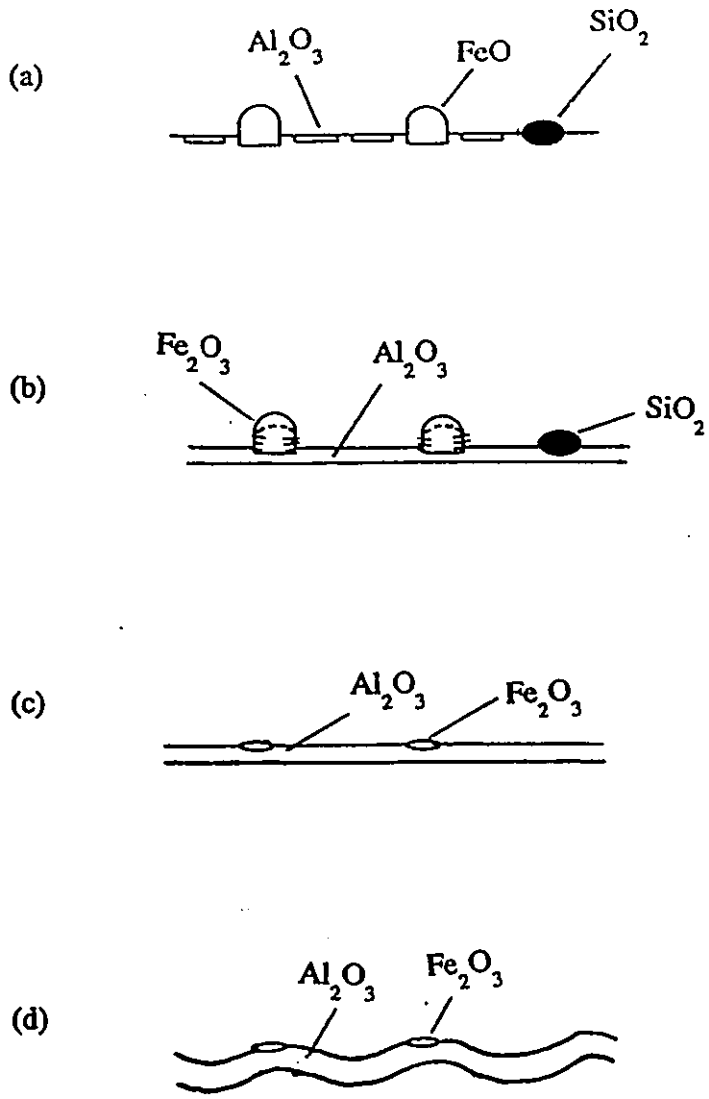

Fig. 7.15 Schematic model illustrating the development of the Al_2O_3 scale formed on the ternary Fe-Si-Al alloys

isolated by a continuous growing layer of Al_2O_3. The outer surface of FeO further reacts with oxygen to form higher oxides such as Fe_2O_3, while SiO_2 is present as β-cristobalite (Fig. 7.15(b)). With continued oxidation, the Al_2O_3 film thickens. Very small amounts of Fe and Si cations may transport from the alloy through leakages in the Al_2O_3 film to the outer oxide surface and react with oxygen there. This is indicated by SIMS depth profile analyses of the oxide formed on Fe-6Si-1Al and Fe-6Si-5Al alloys as shown in Fig. 6.15 and 6.29. But the leakages are soon blocked by a healing layer of Al_2O_3. The amount of Fe and Si transported are not sufficient at the Al_2O_3 surface to allow the formation of a continuous layer of iron and silicon oxides. Eventually, most isolated Fe_2O_3 and SiO_2 may dissolve into the continuous Al_2O_3 oxide (Fig. 7.15(c)). At this stage, Si cannot be detected from Auger survey analysis of the oxide surface or from TEM selected area diffraction analysis, since its concentration in the oxide is so small. As the oxidation continues, the Al_2O_3 growth is accompanied by a build-up of compressive stress within the oxide. This results in the development of a convoluted morphology of the Al_2O_3 scale (Fig. 7.15(d)).

It is generally believed that the mode of stress generation responsible for the development of a convoluted morphology is oxide growth within the oxide layer (lateral growth). Lateral growth appears to occur as a consequence of the formation of new oxide at oxide grain boundaries following the reaction between oxygen ions diffusing inwards and Al ions diffusing outward [7.59]. It is thought to be unlikely that diffusing Al and oxygen species are able to pass each other while moving along the same path. Therefore it has been proposed that Al ions move outward along short circuit paths within the Al_2O_3 grains, whereas oxygen ions move predominantly along the Al_2O_3 grain boundaries [7.60]. In this study, SIMS

depth profiles of the oxides formed indicate that there is outward Al diffusion to some extent, but inward oxygen diffusion is the major transport process. The SIMS depth profiles appear to indicate that the oxygen transport occurs through the lattice, as shown in Fig. 6.15 and 6.29. In the present work, the α-Al_2O_3 grain size is only ~ 100-200 nm after 24 hours oxidation, as indicated by SEM, and so atoms in the grain boundaries could exchange with those in the lattice, making it difficult to distinguish between lattice and grain boundary diffusion. Oxide formation at grain boundaries would give rise to compressive stress in the oxide and a residual tensile stress in the alloy interfacial region. If a pre-existing flaw occurs at the oxide/alloy interface, bulking of the oxide occurs when the compressive stress in the oxide exceeds a critical value. The magnitude of this critical value depends on the ability of the oxide to relieve stress and on the energy required to produce a new surface [7.61]. As a result of oxide bulking, oxide ridges form, usually along alloy grain boundaries and polish markings, as observed by Golightly, Wood and Stott [7.62] as well as in the present study. The initiation and development of oxide ridges over alloy grain boundaries are due to special grain boundary effects, e.g., the more rapid formation of α-Al_2O_3 due to enhanced Al diffusion along alloy grain boundaries, the discontinuity in the specimen surface at alloy grain boundaries, and the crystal misfit at alloy grain boundaries. The oxide ridges grow with oxidation time, thus coarsening the convoluted morphology (Fig. 7.15(d) or 7.16(a)). The coarsening of the convoluted morphology results from a progressive increase in the length of oxide comprising individual ridges. The oxide convolution development produced extensive detachment of the oxide from the alloy, creating cavities beneath the oxide ridges (Fig. 7.16(b)). The detached oxide is believed to continue to thicken and grow

laterally, due to the ready supply of Al, most likely transferred in the vapour phase across the cavity. The continuous later growth of the detached oxide will certainly produce higher compressive stresses in the oxide ridges. On the other hand, compressive stress in the oxide of sufficient magnitude can lead to interface sliding, resulting in plastic deformation of the alloy substrate in the region of the oxide/alloy interface [7.61]. This may be the case particularly for already highly stressed areas such as specimen edges and corners, or at alloy grain boundaries or triple points. As a result of the substrate plastic deformation and the continuous later growth, some detached oxide ridges may crack off (Fig. 7.16(c)). Crack opening or complete scale removal immediately exposes the relatively Al-depleted alloy to the oxidizing environment. Even though the ternary Fe-Si-Al alloy may contain a sufficient concentration of Al to form a healing Al_2O_3 film and thus prevent further oxidation, this fresh healing oxide may not form immediately on exposure of the alloy to oxygen. Often the establishment of the healing oxide is preceded by a "non-steady state" period when all components of the alloy are oxidizing, as indicated by Whittle [7.63]. Therefore, the specimen is likely to undergo the transient oxidation stages outlined earlier. Al_2O_3 could still be formed at the surface of the alloy, but it will not take the form of a coherent layer, which allows the simultaneous oxidation of Fe and Si. Fe-rich oxide nodules may also be formed (Fig. 7.16(d)). Under these conditions, the overall oxidation rate will be much increased and breakway oxidation behavior occurs. Furthermore, oxygen dissolution and diffusion may now occur as the effective oxygen pressure behind the Fe-rich oxide is considerably higher than behind the protective Al_2O_3 oxide. Given time for the build up of sufficient Al atoms at the oxide/alloy interface, either as a result

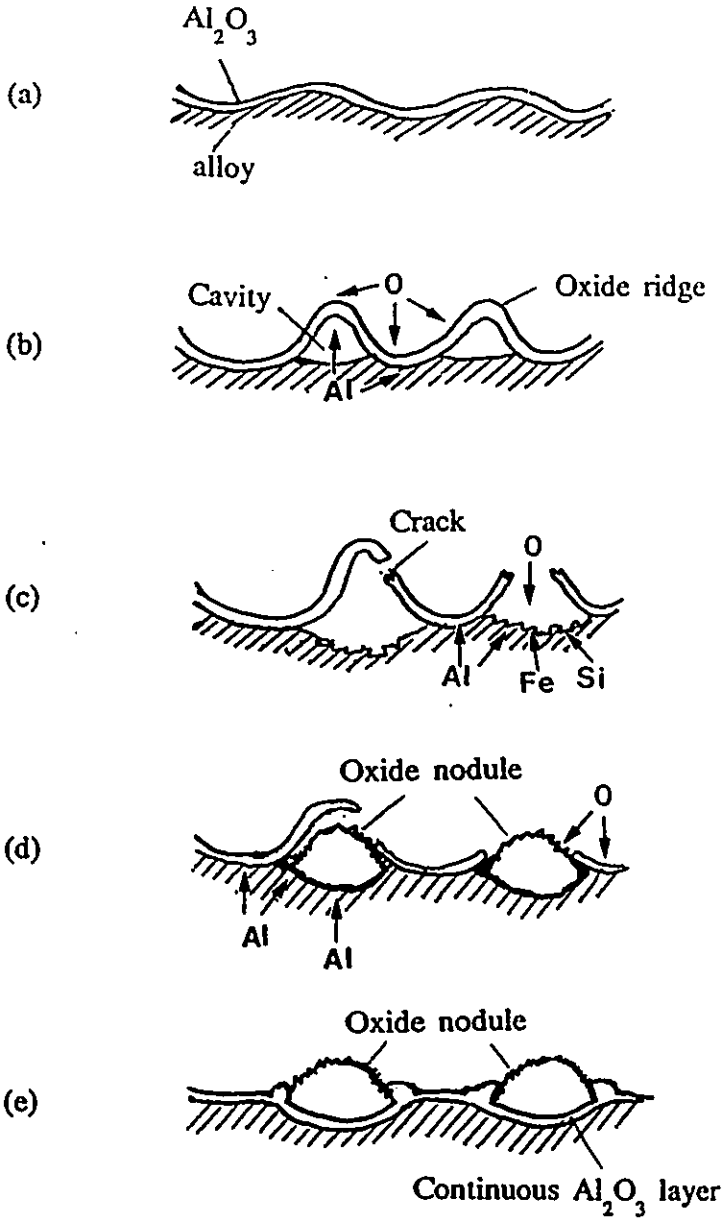

Fig. 7.16 Schematic model illustrating the oxidation behavior of the Fe-6Si-3Al alloys

of the formation of Fe-rich oxide or of diffusion from the bulk of the alloy, oxygen can diffuse into the alloy and react with Al to form a coherent healing layer of Al_2O_3 (Fig. 7.16 (e)), and the alloy again becomes oxidation resistant. Calculating the time at which healing occurs is difficult, principally because of the large number of parameters involved, and the difficulty of assigning values to them in any situation [7.63].

The above model schematically illustrated in Fig. 7.16 may explain the oxidation behavior of the Fe-6Si-3Al alloys in this study. Oxides formed on alloys of this composition exhibited more severe convoluted morphology than those formed on Fe-6Si-1Al and Fe-6Si5Al alloys. Breakway oxidation kinetics occurred after 6 hours oxidation in 0.04-0.07 torr of oxygen. A number of oxide nodules and voids were found mostly at specimen edges. The nodules occurred predominantly at the crest of oxide convolutions. EDAX analysis revealed that the base of the voids associated with the spalling of oxide nodules was Al rich, indicating that the formation of a healing Al_2O_3 layer might occur after long time exposure. Eventually, the alloys oxidized in 760 torr of oxygen for 200 and 500 hours exhibited very good oxidation resistance.

CHAPTER 8

Conclusions and Recommendations for Future Work

8.1 Conclusions

1. Attempts were made to give expressions for the kinetics of internal oxidation of dilute ternary alloys when oxidation conditions favor simultaneous internal oxidation of the two solutes in the alloys. Good agreement between theoretically predicted and experimentally observed values of the depths of internal oxidation zones in Hi-1at%Si-4at%Al alloys at 1073 K, in either Hi/NO packs or in 760 torr of oxygen, demonstrates the applicability of these expressions in describing the kinetics of internal oxidation of ternary alloys.

2. Multi-component diffusion theory was used to establish a criterion for the onset of internal oxidation beneath the external oxide scale, when oxidizing conditions favor formation of the oxide of the least noble metal in a dilute ternary alloy. This criterion was applied to the oxidation of ternary Fe-Si-Al and Hi-Dr-Al alloys. Theoretical predications of minimum Al concentrations required to form a protective Al_2O_3 scale on these two alloys are consistent with the experimental observations.

3. The oxidation behavior of binary and ternary Fe-Si-Al alloys containing 0-6 at% Si and 0-6 at% Al was extensively investigated at 1073 K in either 0.04-0.07 or 760 torr of oxygen. In combination with Si, the Al concentration required to form a protective Al_2O_3 scale on the ternary alloys was found to be significantly lower than that for binary Fe-Al alloys. Theoretical and experimental results are consistent with the hypothesis that there is a synergistic beneficial effect of Si and Al in combination on the oxidation properties of the ternary Fe-Si-Al alloys. Si limits the oxidation of Fe during the transient stage of oxidation and increases the activity and outward diffusion flux of Al to the oxide/alloy interface through ternary interactions during the subsequent stage of parabolic oxidation kinetics.

4. A model was proposed to quantitatively describe the oxygen solubility behavior in an A-B-C alloy beneath a stoichiometric oxide scale of BO_v as a function of alloy compositions. Attempts were made to give a unified treatment of exclusive external scale formation and the transition from internal to external oxidation for binary alloys.

8.2. Recommendations for Future Work

For the kinetics of internal oxidation of ternary alloys, models remain to be developed to describe the influence of distribution and morphology of internal oxide precipitates on the effective diffusion flux of oxygen in the internal

oxidation zone. Future work should also place emphasis on the derivation of expressions to describe detailed modes and magnitudes of the formation of internal oxide-denuded base metals on the alloy surface during internal oxidation, as well as its influence on the kinetics of internal oxidation of both binary and ternary alloys.

More fundamental knowledge is required to fully understand the oxygen solubility and diffusion behavior in binary and ternary alloys as a function of alloy compositions. Values of the thermodynamic interaction parameters between oxygen and alloying elements, together with values of the diffusion coefficients involving oxygen and alloying elements, are often not available at temperatures of solid state. Such basic data are also important in the prediction of minimum solute concentrations required to form a protective oxide scale on ternary alloys.

The marked influence of Si additions on the oxidation properties of Fe-Al alloys warrants further investigation. Experimental measurements of diffusion or thermodynamic data for the Fe-Si-Al-O system should be carried out. Transport mechanisms in growing oxides of both SiO_2 and Al_2O_3 formed on Fe alloys remain to be established.

REFERENCES

Chapter 1

[1.1] G.A. Pickup, *Metals and Materials.*, 4(1970)166

[1.2] J.A. Von Fraunhofer and G.A. Pickup, *Anti-Corros. Meth. Mater.*, 17(1970)10

[1.3] W.E. Boggs, *Oxid. Met.*, 10(1976)277

[1.4] G.S. Giggins and F.S. Pettit, *J. Electrochem. Soc.*, 118(1971)1782

[1.5] G.R. Wallwork and A.Z. Hed, *Oxid. Met.*, 3(1971)171

[1.6] I.A. Kvernes and P. Kofstad, *Metall. Trans.*, 3(1972)1511

[1.7] P. Kofstad, *High Temp. Corros.*, Elsevier Appl. Sci. Pub., New York, 1988

[1.8] C. Wagner, *Z. Electrochem.*, 63(1959)772

[1.9] F. Maak, *Z. Metallkd.*, 52(1961)545

[1.10] D.P. Whittle, Y. Shida, G.C. Wood, F.H. Stott, and B.D. Bastow, *Corros. Sci.*, 23(1983)9

[1.11] R.A. Rapp, *Corrosion*, 21(1965)382

Chapter 2

[2.1] P. Kofstad, *High Tempersture Corrosion*, Elsevier Applied Science, 1988

[2.2] N. Birks and G.H. Meier, *Introduction to High Temperature Oxidation of Metals*, Edward Arnold, Lodon, 1983

[2.3] O. Kubaschewski and B.E. Hopkins, *Oxidation of Metals and Alloys*, Butterworths, London, 1962

[2.4] R.A. Rapp, Editor, *High Temperature Corrosion*, NACE-6, 1983

[2.5] *Oxidation of Metals and Alloys*, ASM, Metals Park, Ohio, 1971

[2.6] G.C. Wood and F.H. Stott, *Mat. Sci. and Tech.*, 3(1987)519

[2.7] E.L. Cussler, *Multicomponent Diffusion*, American Elsevier Publishing, New York, 1976

[2.8] J.S. Kirkaldy and D.J. Young, *Diffusion in the Condensed State*, The Institute of Metals, London, 1987

[2.9] F. Kohler, *Monatsh. Chemie.*, **91**(1960)738

[2.10] C. Colinet, *D.E.D., Fac. des Sci.*, University Grenoble, France, 1967

[2.11] Y.M. Muggianu, M. Gambino, and J.P. Bros, *J. Chim. Phys.*, 72(1975)83

[2.12] G.W. Toop, *Trans. AIME*, **233**(1965)850

[2.13] M. Hillert, *Calphad*, 4(1980)1

[2.14] K.C. Chou, *Calphad*, **11**(1987)293

[2.15] I. Ansara, *Metallurgical Symposium*, O. Kubaschewski, ed., Her Majesty's Stationery Office, London, 1972, p403

[2.16] C.H.P. Lupis, *Chemical Thermodynamics of Materials*, North-Holland, New York, 1983

[2.17] C. Wagner, *Acta Met.*, **21**(1973)1297

[2.18] T. Chiang and Y.A. Chang, *Met. Trans.* **7B**(1976)453

[2.19] W.W. Liang, *Z. Metallkunde*, **73**(1982)369

[2.20] L. Onsager, *Ann. N. Y. Acad. Sci.*, **46**(1945/6)241

[2.21] H.L. Toop, *A. I. Ch. E. Journal*, **10**(1964)460

[2.22] F.N. Rhines, *Trans. AIME*, **137**(1940)246

[2.23] C. Wagner, *Z. Elecktrochem.*, **63**(1959)772

[2.24] F.N. Rhines, W.A. Johnson and W.A. Anderson, *Trans. AIME*, **147**(1942)205

[2.25] F. Maak, *Z. Metallkunde*, **52**(1961)538

[2.26] F. Gesmundo and F. Viani, *Oxid. Met.*, **25**(1986)269

[2.27] J.S. Kirkaldy, *Can. Met. Q.*, **8**(1969)35

[2.28] G.R. Laflamme and J.E. Morral, *Acta Met.*, 26(1978)1791

[2.29] E.K. Ohriner and J.E. Morral, *Scripta Met.*, 13(1979)7

[2.30] R.A. Rapp, *Corrosion*, 21(1965)382

[2.31] C. Wagner, *Corros. Sci.*, 8(1968)889

[2.32] W.W. Smeltzer and D.P. Whittle, *J. Electrochem. Soc.*, 125(1978)117

[2.33] C. Wagner, *Z. Phys. Chem.*, B21(1933)25

[2.34] W.W. Smeltzer, R.R. Haering, and J.S. Kirkaldy, *Acta Met.*, 9(1961)880

[2.35] C. Wagner, *Corros. Sci.*, 9(1969)91

[2.36] C. Wagner, *Corros. Sci.*, 5(1965)751

[2.37] J.E. Morral, M.S. Thompson, and O.F. Devereux, in *Oxidation of Metals and Association Mass Transport*, M.A. Dayanada, *et al.*, eds., The Metallurgical Society, 1987, p315

[2.38] J.E. Morral, *Scrip. Met.*, 18(1984)1257

[2.39] M.S. Thompson and J.E. Morral, *Acta Met.*, 34(1986)2201

[2.40] J.E. Morral, M.S. Thompson, and O.F. Deverux, *Scrip. Met.*, 20(1986)1355

[2.41] R.A. Perkins, K.T. Chiang, and G.H. Meier, *Scrip. Met.*, 22(1988)419

Chapter 3

[3.1] G.R. Wallwork and A.Z. Hed, *Oxid. Met.*, 3(1971)171

[3.2] D. Hardwick and G.R. Wallwork, *Reviews on High Temperature Materials*, 4(1978)47

[3.3] P. Tomaszewicz and G.R. Wallwork, *ibid*, 4(1978)75

[3.4] J.L. Corkum, *M.Eng. Thesis*, McMaster University, 1988

[3.5] G.S. Giggins and F.S. Pettit, *J. Electrochem. Soc.*, 118(1971)1782

[3.6] F.H. Stott, G.C. Wood and M.G. Hobby, *Oxid. Met.*, 3(1971)103

[3.7] V.G. Rivlin and G.V. Raynor, *International Metals Reviews*, 3(1981)133

[3.8] A. Steiner and K.L. Komarek, *Trans. AIME*, 230(1964)786

[3.9] J. Eldridge and K.L. Komerek, *TMS AIME*, 230(1964)226

[3.10] G.G. Liibowitz, *Met. Trans.*, 2(1971)89

[3.11] O. Kubaschewski and W.A. Dench, *Acta Met.*, 3(1955)339

[3.12] S.V. Radcliffe, B.L. Averbach and M. Cohen, *Acta Met.*, 9(1961)169

[3.13] L. Kaufman and H. Nesor, *Calphad*, 2(1978)325

[3.14] L.M. Atlas and W.K. Sumida, *J. Amer. Ceram. Soc.*, 41(1958)158

[3.15] F.A. Elrefaie and W.W. Smeltzer, *Met. Trans.*, 14B(1983)85

[3.16] J. Chipman, J.C. Fulton, N. Gokien, and G.R. Caskey, *Acta Met.*, 2(1954)439

[3.17] A. Schneideer and W. Meyer-Yungnick, Angew. Chem., 67(1955)307

[3.18] P.J. Bowles, H.F. Ramstad, and F.D. Richardson, *J. Iron Steel Inst.*, 202(1964)2

[3.19] V.H. Schench, E. Schmidtmann and H.M. Aachen, *Arch. Eisen.*, 30(1960)121

[3.20] R.A. Vecher, Y.I. Gerasimovand and V.A. Geiderikh, *Russian J. Phy.Chem.*, 39(1965)650

[3.21] L. Kaufman, *Calphad*, 1(1977)7

[3.22] B.J. Lee, S.K. Lee and D.N. Lee, *Calphad*, 11(1987)253

[3.23] D. Ludecke, *Z. Metallkunde*, 77(1986)5

[3.24] T. Miyazaki, T. Kozakai and T. Tsuzuki, *J. Mater. Sci.*, 2191986)2557

[3.25] M. Mitani, H. Nagai and T. Ohtani, *J. Jpn. Inst. Met.*, 34(1970)165

[3.26] G.I. Batalin, V.S. Sudavtosova, R.N. Shevchuck, V.I. Ulyanov and G.B. Bondarenko, *Atom. Svarka.*, 1(1980)70

[3.27] R.K. Iyengar, W.O. Philbrook, *Met. Trans.*, 4(1973)2181

[3.28] F. Kanz, *Arch. Eisenhuttenn*, 8(1934)67

[3.29] R. Schenck, *Z. Ano. Allg. Chem.*, 206(1932)129

[3.30] A. Benedicks, *Non-Metallic Inclusions in Iron and Steel*, TMS, 1930, p92

[3.31] W.W. Smeltzer, L.A. Morris, R.C. Logani, *Can. Metall. Quart.*, 9(1970)513

[3.32] R. Sifferlen, *Cr. Acad. Sci. Fr.*, 247(1952)1608

[3.33] L.S. Darken, J. Amer. Chem. Soc., 70(1948)2046

[3.34] E.J. Hrostowki, *Phys. Chem. Solids*, 9(1959)214

[3.35] O.H. Lindsley, *Amer. J. Sci.*, 266(1968)342

[3.36] L. Brewer and F.T. Greene, *J. Phys. Chem. Solids*, 2(1957)286

[3.37] A. Muan, *J. Metals*, 7(1955)1

[3.38] R.E. Johnson and A. Muan, *J. Amer. Ceram. Soc.*, 51(1968)431

[3.39] A.U. Seybolt and E.I. Alessandrini, *Trans. AIME*, 212(1958)507

[3.40] R. Scott, *Trans. Ceram. Soc.*, 25(1926)339

[3.41] E. Swinden, *J. Iron Steel Inst.*, 2(1941)203

[3.42] N.L. Bowen and J.F. Schairer, *Amer. J. Sci.*, 24(1932)177

[3.43] A. Muan, *Trans. AIME*, 203(1955)965

[3.44] H.J. Engell, *Arich. Eisenhuttenw*, 28(1957)109

[3.45] L.S. Darken, *J. Amer. Chem. Soc.*, 68(1946)798

[3.46] J. White, *J. Iron Steel Inst.*, 148(1953)579

[3.47] D.R. Wones and M.C. Gilbert, *Amer. J. Sci.*, 267A(1969)480

[3.48] A. Muan, *J. Amer. Ceram. Soc.*, 40(1957)121

[3.49] A. Muan, *ibid*, 40(1957)420

[3.50] V.S. Raghunathan and B.D. Sharma, *Philos. Mag.*, 43A(1981)427

[3.51] K. Sato, *Trans. Jpn. Inst. Met.*, 4(1963)121

[3.52] K. Hirano and A. Hishinuma, *J. Jpn. Inst. Met.*, 32(1968)516

[3.53] K. Nishida, T. Yamamoto and T. Nagota, *Trans Jpn. Inst. Met.*, 12(1970)319

[3.54] H.C. Akuezue and D.P. Whittle, *Met. Sci.*, 17(1983)27

[3.55] H.A.A. Ahmed, *Ph.D. Thesis*, McMaster University, 1984

[3.56] R.J. Borg and D.Y.F. Lai, *J. Appl. Phys.* 41(1970)5193

[3.57] W. Batz, H.W. Mead and C.E. Birchenall, *J. Metals*, 4(1952)1070

[3.58] H.V.M. Mirani and P. Maaskant, *Phys. State Sol.* 14A(1972)521

[3.59] H. Mitani, M. Omishi and T. Shikano, *J. Jpn. Inst. Met.*, 30(1966)56

[3.60] S.V. Kositsyn, V.S. Ltvinov, V.G. Sorokin and M.A. Gervasyer, *Phys. Met. Metall.*, 49(1980)138

[3.61] J. Takada, S. Yamamoto, S. Kikuchi and M. Adchi, *Oxid. Met.*, 25(1986)93

[3.62] J. Takada, S. Yamamoto, S. Kikuchi and M. Adchi, *J. Mater. Sci.*, 21(1986)2133

[3.63] A. Goursat and W.W. Smeltzer, *Rev. High Temp. Mat.*, 1(1971)353

[3.64] L. Himel, R.F. Mehl and C.E. Birchenal, *Trans. AIME*, 197(1953)827

[3.65] R. Haul and G. Dumbgen, *Z. Electrochem.*, 66(1962)636

[3.66] E.W. Sucov, *J. Amer. Ceram. Soc.*, 46(1965)190

[3.67] E.L. Williams, *ibid*, 48(1965)190

[3.68] H. Yinnon, *Ph.D. Thesis*, Case Western Reserve University, 1979

[3.69] F.J. Norton, *Nature*, 191(1961)701

[3.70] J.D. Cawley, J.W. Halloran and A.R. Cooper, *Oxid. Met.*, 28(1987)1

[3.71] A. Aktinson and J.W. Gardner, *Corros. Sci.*, 21(1981)49

[3.72] F.A. Kroger, in *High Temp. Corros.*, R.A. Rapp, ed., NACE-6, 1983, p89

[3.73] R. Prescott and M.J. Graham, *Oxid. Met.*, 38(1992)233

[3.74] A. Aktinson, *Corro. Sci.*, 22(1982)347

[3.75] V.I. Izvekov and K.M. Gorbunova, *Phys. Met. Metall.*, 7(1959)71

[3.76] W.E. Boggs, *J. Electrochem. Soc.*, 118(1971)906

[3.77] G.J. Bateman and R. Rolls, *Br. Corros. J.*, 5(1970)122

[3.78] N.G. Schmahl, H. Baumann and H. Schenck, *Archiv. Eisenhuttw.*, 30(1959)345

[3.79] P. Tomaazewicz and G.R. Wallwork, *Oxid. Met.*, 19(1983)165

[3.80] G.R. Wallwork and M.B. McGirr, in *Stress Effects and Oxidation of Metals*, J.V. Cathcart, ed., AIME, New York, 1975, p263

[3.81] G.C. Wood and F.H. Stoot, in *High Tem. Corros.*, NACE-6, 1983

[3.82] R.E. Grace and A.V. Seybolt, *J. Electrochem. Soc.*, **105**(1958)582

[3.83] T. Nakayama and K. Kaneko, *Corrosion*, **26**(1966)168

[3.84] F. Saegusa and L. Lee, *ibid*, 22(1962)168

[3.85] R. Prescott, D.F. Mitchell, G.I. Sproule, R.J. Hussey and M.J. Graham, in *High Temp. Corros. Advan. Mater. Protect. Coatings.*, North Holland, 1992

[3.86] P. Tomas, *Ph.D. Thesis*, University of New South Wales, 1982

[3.87] R. Prescott and M. J. Graham, *Oxid. Met.*, **38**(1992)73

[3.88] V.V. Ipatyev and G. Morlova, *J. Appl. Chem. (U.S.S.R.)*, **29**(1956)981

[3.89] J.W. Evans and S.K. Chatterji, *J. Electrochem. Soc.*, **106**(1959)860

[3.90] R. Logani and W.W. Smeltzer, *Oxid. Met.*, **1**(1969)3

[3.91] *ibed*, 3(1971)15

[3.92] *ibed*, 3(1971)279

[3.93] I. Svedung and N.G. Vannerberg, *Corros. Sci.*, **14**(1974)391

[3.94] T. Ban, K. Bohenkamp and H.J. Engell, *ibid*, **19**(1979)283

[3.95] A.U. Seybolt and E.I. Alessandrini, *Trans. AIME*, **215**(1959)756

[3.96] T. Adachi and G.H. Meier, *Oxid. Met.*, **27**(1987)347

[3.97] A. Atkinson, *Corros. Sci.*, **22**(1982)87

[3.98] E.A. Brandes, *Fulmer Res. Inst. Special Rep.*, **2**, 1956

[3.99] C.W. Tuck, *Corros. Sci.*, **5**(1965)631

[3.100] G.A. Pickup, *Met. Mater.*, **4**(1970)166

[3.101] J.A. Von Fraunhofer and G.A. Pickup, in *Proc. 4th Inter. Cong. Met. Corros.*, NACE, 1972

[3.102] J.A. Von Fraunhofer and G.A. Pickup, *Anti-Corros. Meth. Mater.*, **17**(1970)10

[3.103] W.E. Boggs, *Oxid. Met.*, **10**(1976)277

[3.104] S. Guruswamy, J.P. Hirth and G.W. Powell, *Oxid. Met.*, **19**(1983)77

[3.105] M. Hunens and K.H. Schmidt, *J. Magn. Magn. Mater.*, **19**(1980)72

[3.106] K. Hartig and G. Pospiech, *ibid*, **19**(1980)79

[3.107] M. Hansen, K. Anderko, *Constitution of Binary Alloys*, McGraw-Hill, New York, 1958

[3.108] A. Steiner, K.L. Komarek, *Trans. AIME*, **230**(1964)786

[3.109] R.E. Hanneman, A.U. Seybolt, *ibid*, **245**(1969)434

[3.110] P. Nash, *Bulletin of Alloy Phase Diagrams*, **7**(1986)466

[3.111] H. Davies and W.W. Smeltzer, *J. Electrochem. Soc.*, **121**(1974)543

[3.112] F.N. Mazandarany and R.D. Pehlke, *Met. Trans.*, **4**(1973)2067

[3.113] W. Johnson and E. Miller, *Trans. Metall.Soc. AIME*, **249**(1968)1685

[3.114] L. Kaufman and H. Nesor, *Z. Metallkunde*, **64**(1973)249

[3.115] V.F. Malkin and V.V. Pokidyshev, *Izv. Akad. Nauk. SSSR.*, **6**(1965)1747

[3.116] N.C. Oforka and B.B. Argent, *J. Less-Common Met.*, **114**(1985)97

[3.117] F.A. Elrefaie, *Ph.D. Thesis*, McMaster University, 1979

[3.118] C.J. Smithells and C.E. Ransley, *Proc. Roy. Soc.*, **A155**(1936)195

[3.119] A. Green and N. Swindells, *Mater. Sci. Tech.*, **1**(1985)101

[3.120] M.S. Seltzer and B.A. Wilocx, *Metall. Trans.*, **3**(1972)2357

[3.121] T. Tamamoto, T. Takashima and K. Nishida, *Trans. Jpn. Inst. Met.*, **21**(1980)601

[3.122] J.A. Nesbitt and R.W. Heckel, *Metall. Trans.*, **18A**(1987)2075

[3.123] R. Barlow and P.J. Grundy, *J. Mat. Sci.*, **4**(1969)797

[3.124] R.A. Kerr, *M.S. Thesis*, The Ohio State University, 1972

[3.125] J.A. Nesbitt, *J. Electrochem. Soc.*, **136**(1989)1511

[3.126] F.S. Pettit, *Trans. AIME*, **239**(1967)1296

[3.127] F.H. Stott and G.C. Wood, *Corros. Sci.*, 17(1977)647

[3.128] Y. Shida, *Ph.D. Thesis*, University of Manchester, 1979

[3.129] A. Martinez-Villafance, *Ph.D. Thesis*, University of Manchester, 1983

[3.130] D.P. Whittle, Y.Shida, G.C. Wood, F.H. Stott and B.D. Bastow, *Philos. Mag.*, A46(1982)931

[3.131] F.H. Stott, G.C. Wood, D.P. Whittle, B.D. Bastow, Y. Shida and A. Martinez-Villafance, *Solid State Ionics*, 12(1984)365

[3.132] H. Hindam and D.P. Whittle, *J. Mater. Sci.*, 18(1983)1389

[3.133] W.W. Smeltzer, H. Hindam and F.A. Elrefaie, in *High Temp. Corros.*, R.A. Rapp, ed., NACE, 1983

[3.134] G.R. Wallwork and A.Z. Hed, *Oxid. Met.*, 3(1971)171

[3.135] I.A. Kvernes and P. Kofstad, *Metall. Trans.*, 3(1972)1511

[3.136] F.A. Golightly, G.C. Wood and F.H. Stott, *Oxid. Met.*, 14(1980)217

[3.137] G.N. Irving, J. Stringer and D.P. Whittle, *ibid*, 9(1975)427

[3.138] P. Kofstad, *High Tempersture Corrosion*, Elsevier Applied Science, 1988

[3.139] D. P. Whittle, in *High Temp. Corros.*, R.A. Rapp, ed., NACE, 1983

[3.140] R.W. Guard and E.A. Smith, *J. Inst. Met.*, 88(1959/60)369

[3.141] R.A. Swalin, A. Martin and R. Olson, *J. Met*alts, 9(1957)936

[3.142] I.S. Gildengorn and I. L. Rogelberg, *Fiz. Met. Metalloved.*, 17(1964)527

[3.143] S. Okamoto and S. Okada, *Nippon Kinzoku Gakkai-Shi*, 21(1957)544

[3.144] D.L. Douglass, P. Nanni, C. De Asmundis and C. Bottino, *Oxid. Met.*, 28(1987)309

[3.145] G.H. Meier, in *High Temp Corros. 2*, R. Streiff, *et al.*, eds, Elsevier, Sci. Pub., London, 1989

Chapter 4

[4.1] L.S. Darken, *Trans. AIME*, 221(1961)654

[4.2] P.N. Smith, *Ph.D. Thesis*, McMaster University, 1970

[4.3] C. Wagner, *Z. Electrochem.*, **63**(1959)772

[4.4] R.A. Rapp, *Corrosion*, **21**(1965)382

[4.5] H.L. Toop, *A. I. Ch. E. Journal*, **10**(1964)460

[4.6] F.N. Rhines, W.A. Johnson and W.A. Anderson, *Trans. AIME*, **147**(1942)205

[4.7] F. Maak, *Z. Metallkunde*, **52**(1961)538

[4.8] F. Gesmundo and F. Viani, *Oxid. Met.*, **25**(1986)269

[4.9] H.M. Hindam, *Ph.D. Thesis*, McMaster University, 1979

[4.10] R.A. Rapp, *Acta Met.*, **9**(1961)730

[4.11] A. Atkinson, *Corros. Sci.*, **22**(1982)87

[4.12] D.L. Douglass, P. Nanni, C.D. Asmundis and C. Bottino, *Oxid. Met.*, **28**(1987)309

[4.13] J.A. Nesbitt, *J. Electrochem. Soc.*, **136**(1989)1511

[4.14] W.W. Smeltzer and D.P. Whittle, *J. Electrochem. Soc.*, **125**(1978)117

[4.15] F.S. Pettit, *Trans. AIME*, **239**(1967)1296

[4.16] H. Hindam and D.P. Whittle, *J. Mater. Sci.*, **18**(1983)1389

[4.17] C. Wagner, *Corros. Sci.*, **8**(1968)889

[4.18] *ibed*, **5**(1965)751

[4.19] J.E. Morral, M.S. Thompson, and O.F. Deverux, *Scrip. Met.*, **20**(1986)1355

Chapter 5

[5.1] S. Hofman, in *Practical Surface Analysis*, D. Briggs and M.P. Seah, eds., Wiley and Sons Pub., 1983, p141

Chapter 6

[6.1] H.C. Yi, S.W. Guan, W.W. Smeltzer and A. Petric, *Acta Metall.*, submitted

[6.2] R. Prescott, D.F. Mitchell, G.I. Sproule, R.J. Hussey and M.J. Graham, in *High Temperature Corrosion of Advanced Materials and Protective Coatings*, Y. Saito eds., Elsevier Sci. Pub., 1992, p83

Chapter 7

[7.1] B.J. Lee, S.K. Lee and D.N. Lee, *Calphad*, 11(1987)253

[7.2] C.H.P. Lupis, *Chemical Thermodynamics of Materials*, North-Holland, New York, 1983

[7.3] R.A. Vecher, Y.I. Gerasimovand and V.A. Geiderikh, *Russian J. Phy.Chem.*, 39(1965)650

[7.4] L.S. Darken, *J. Amer. Chem. Soc.*, 70(1948)2046

[7.5] J.F. Elloitt and M. Gleiser, *Thermochemistry for Steel Making*, North-Holland, London, 1960

[7.6] R.W. Taylor and J. Schmalzried, *J. Phys. Chem.*, 68(1964)2444

[7.7] E.J. Hrostowki, *Phys. Chem. Solids*, 9(1959)214

[7.8] G.I. Batalin, V.S. Sudavtosova, R.N. Shevchuck, V.I. Ulyanov and G.B. Bondarenko, *Atom. Svarka.*, 1(1980)70

[7.9] K. Nishida, T. Yamamoto and T. Nagota, *Trans Jpn. Inst. Met.*, 12(1970)319

[7.10] R.J. Borg and D.Y.F. Lai, *J. Appl. Phys.* 41(1970)5193

[7.11] R.A. Swalin, A. Martin and R. Olson, *J. Met.*, 9(1957)936

[7.12] W. Gust, M.B. Hintz, A. Lodding, H. Odelius and B. Predel, *Phys. Stat. Sol.*, 64(1981)187

[7.13] L. Kaufman, *Calphad*, 3(1979)45

[7.14] L. Kaufman and H. Nesor, *Calphad*, 2(1978)325

[7.15] D. Ludecke, Z. *Metallkunde*, 77(1986)279

[7.16] T. Chiang and Y.A. Chang, *Met. Trans.* 7B(1976)453

[7.17] W.W. Liang, Z. *Metallkunde*, 73(1982)369

[7.18] D. Janke and W.A. Fischer, *Arch. Eisenhuttenwes*, 46(1975)297

[7.19] M. Hansen, *Constitution of Binary Alloys*, McGraw-Hill, 1958, p1025

[7.20] J. Park and C.J. Altstetter, *Met. Trans.*, 18A(1987)43

[7.21] F.H. Stott, G.C. Wood, *Mater. Sci. Tech.*, 4(1988)1072

[7.22] S. Guruswamy, S.M. Park, J.P. Hirth and R.A. Rapp, *Oxid. Met.*, 26(1986)77

[7.23] J.R. Machert, R.D. Ringle and C.W. Fairhurt, *J. Dent. Res.*, 62(1983)1229

[7.24] R.P. Rubly and D.L. Douglass, in *High Temperature Corrosion of Advanced Materials and Protective Coatings*, Y. Saito eds., Elsevier Sci. Pub., 1992, p133

[7.25] H.C. Yi, S.W. Guan, W.W. Smeltzer and A. Petric, *Acta Metall.*, submitted

[7.26] R.A. Rapp, *Corros.*, 21(1965)382

[7.27] J.A. Nesbitt and R.W. Heckel, *Metall. Trans.*, 18A(1987)43

[7.28] M.S. Seltzer and B.A. Wilcox, *Metall. Tran.*, 3(1972)2357

[7.29] T. Yamamoto, T. Takashima and K. Nishida, *Trans. Japan. Inst. Met.*, 21(1980)601

[7.30] C.J. Smithells and C.E. Ransley, *Proc. Roy. Soc.*, A155(1936)195

[7.31] G.S. Giggins and F.S. Pettit, *J. Electrochem. Soc.*, 118(1971)1782

[7.32] J.A. Nesbitt, *J. Electrochem. Soc.*, 99(1952)369

[7.33] C. Wagner, *J. Electrochem. Soc.*, 103(1956)571

[7.34] Golightly, G.C. Wood and F.H. Stott, *Oxid. Met.*, 14(1980)217

[7.35] G.N. Irving, J. Stringer and D.P. Whittle, *ibid*, 9(1975)427

[7.36] I.A. Kvernes and P. Kofstad, *Metall. Trans.*, 3(1972)1511

[7.37] G.R. Wallwork and A.Z. Hed, *Oxid. Met.*, 3(1971)171

[7.38] D.P. Whittle, in *High Temperature Corrosion*, R.A. Rapp, ed., NACE6, 1983, p171

[7.39] P. Kofstad, *High Temp. Corros.*, Elsevier Sci. Pub., New York, 1988, p368

[7.40] W.W. Smeltzer and D.P. Whittle, *J. Electrochem. Soc.*, 125(1978)117

[7.41] F.N. Mazandarany and R.D. Pehlke, *Met. Trans.*, 4(1973)2067

[7.42] F.A. Elrefaie, *Ph.D. Thesis*, McMaster University, 1979

[7.43] N.C. Oforka and B.B. Argent, *J. Less-Common Met.*, 114(1985)97

[7.44] L. Himmel, R.F. Mehl and J.S. Anderson, *Trans. AIME*, 197(1953)827

[7.45] P. Tomas, *Ph.D. Thesis*, The University of New South Wales, 1982

[7.46] W.C. Hagel, *Corros.* 21(1965)316

[7.47] R. Prescott and M.J. Graham, *Oxid. met.*, 38(1992)73

[7.48] P. Tomaszewicz and G.R. Wallwork, *Oxid. Met.*, 19(1983)165

[7.49] C. Wagner, *J. Electrocehm. Soc.*, 103(1956)627

[7.50] J. Kapteijn, S.A. Couperus and J.L. Meijering, *Acta. Met.*, 17(1969)1311

[7.51] A. Ashary, G.H. Meier and F.S. Pettit, *Report on AFOSR, No. 80-0089*, 1986

[7.52] T. Adachi and G.H. Meier, *Oxid. Met.*, 27(1987)347

[7.53] W.E. Boggs, *Oxid. Met.*, 10(1976)277

[7.54] R. Sifferlen, *Compt. Rend.*, 247(1958)1608

[7.55] G.K. Sigworth and J.F. Elloitt, *Met. Sci.*, 8(1974)298

[7.56] V.G. Rivlin and G.V. Raynor, *International Metals Reviews*, 3(1981)133

[7.57] J. Crank, *The Mathematics of Diffusion*, Oxford Univ. Press., 1970, p30

[7.58] J. Takada, S. Yamamoto, S. Kikuchi and M. Adachi, *Oxid. Met.*, 25(1986)93

[7.59] A. Rahmel, G.C. Wood, P. Kofstad and D.L. Douglass, *Oxid. Met.*, 23(1985)2251

[7.60] G.C. Wood and F.H. Stott, in *High Temperature Corrosion*, R.A. Rapp, ed., NACE6, 1983, p227

[7.61] A.G. Evans, G.B. Crumley and R.E. Demaray, *Oxid. Met.*, 20(1983)193

[7.62] F.A. Golightly, G.C. Wood and F.H. Stott, *Oxid. Met.*, 14(1980)217

[7.63] D.P. Whittle, *Oxid. Met.*, 4(1972)171